Ahsan Habib Khandoker
Chandan Karmakar
Michael Brennan
Andreas Voss
Marimuthu Palaniswami

Poincaré Plot Methods for Heart Rate Variability Analysis

Springer

Poincaré Plot Methods for Heart Rate Variability Analysis

Ahsan Habib Khandoker • Chandan Karmakar
Michael Brennan • Andreas Voss
Marimuthu Palaniswami

Poincaré Plot Methods for Heart Rate Variability Analysis

Springer

Ahsan Habib Khandoker
Department of Biomedical Engineering
Khalifa University, Abu Dhabi, UAE

Department of Electrical and Electronic Engineering
The University of Melbourne, VIC, Australia

Michael Brennan
Electrical and Electronic Engineering
The University of Melbourne
Melbourne, VIC, Australia

Marimuthu Palaniswami
Electrical and Electronic Engineering
The University of Melbourne
Melbourne, VIC, Australia

Chandan Karmakar
Electrical and Electronic Engineering
The University of Melbourne
Melbourne, VIC, Australia

Andreas Voss
Department of Medical Engineering and Biotechnology
University of Applied Sciences Jena
Jena, Germany

ISBN 978-1-4614-7374-9 ISBN 978-1-4614-7375-6 (eBook)
DOI 10.1007/978-1-4614-7375-6
Springer New York Heidelberg Dordrecht London

Library of Congress Control Number: 2013939585

Dedicated to students and researchers of biomedical engineering.

Preface

Heart rate variability is the study of autonomic nervous activity through the information provided by fluctuations in heart rate. Autonomic activity is responsible for regulating heart rate. By studying the beat-to-beat variability in the intervals between heartbeats, it is possible to form a representation of autonomic nervous activity. Alterations in this activity can thus be quantitatively measured with a non-invasive technique. Accordingly, heart rate variability has become a very active field of research and the most popular biological signal by which the autonomic nervous system is studied. Heart rate variability can measure the individual levels of parasympathetic and sympathetic modulation of heart rate, and from this information one can make predictions on the state of the autonomic nervous system. Moreover, a deeper exploration of the physiological basis of the autonomic nervous system can be investigated.

The study of the autonomic nervous system from the information contained in heart rate relies upon mathematical models and techniques and the power of digital computers to achieve reliable and accurate results. In the past only simplistic mathematical techniques have been brought to bear due to the limited ability of clinical investigators in this regard. Recently, mathematicians, physicists and engineers have worked alongside cardiologists and physiologists to develop sophisticated models and mathematical techniques for the analysis of heart rate data. The development of more accurate models of heart rate variability and robust analysis techniques that are immune to the large levels of noise and artefact found in all biological signals is an active field of research currently. Advances in this area have direct benefits to clinical and physiological studies that employ heart rate variability to study disease and physiology.

Many of the mathematical techniques are only approximations and have defects that are not obvious except when analysed carefully with a mathematical formulation. Mathematical analysis allows one to investigate the limitations of analysis techniques. Further, the full potential of the analysis techniques is often only revealed by a full mathematical treatment. The theoretical study of models of the autonomic system has similar characteristics, with the limitations and full descriptive power of a model being largely unknown until studied mathematically.

The study of models also allows the development of optimal analysis techniques. Many of the mathematical algorithms and models applied in HRV analysis remain uninvestigated. The problem is, how do we quantitatively characterize (linear and/or nonlinear) the heart rate time series to capture useful summary descriptions that are independent of existing HRV measures? Recent research on HRV has proven that Poincaré plot analysis (PPA) is a powerful tool to mark short-term and long-term HRV. Researchers have investigated a number of techniques: converting the two-dimensional plot into various one-dimensional views; the fitting of an ellipse to the plot shape; and measuring the correlation coefficient of the plot. In fact, they are all measuring linear aspects of the intervals which existing HRV indices already specify. The fact that these methods appear insensitive to the nonlinear characteristics of the intervals is an important finding because the Poincaré plot is primarily a nonlinear technique. This result motivates the search for better methods for Poincaré plot quantification. This provides the motivation for this book.

Chapter 1 gives an overview of the physiological concepts and necessary background in the field of heart rate variability, including the history, physiology, analysis techniques and the clinical significance of the field. This includes models of heart rate variability and the mathematical signals employed to characterize heart rate variability. Details of the time-domain and frequency-domain analysis of these signals are also covered.

Chapter 2 provides a mathematical analysis of a common heart rate variability technique known as the Poincaré plot. The Poincaré plot is an emerging analysis technique that takes a sequence of intervals between heartbeats and plots each interval against the following interval. The geometry of this plot has been shown to distinguish between healthy and unhealthy subjects in clinical settings by employing trained specialists to visually classify the plots. The Poincaré plot is a valuable HRV analysis technique due to its ability to display nonlinear aspects of the interval sequence. In particular we investigate the question of whether existing measures of Poincaré plot geometry reflect nonlinear features of heart rate variability. We show that methods of Poincaré quantification that summarize the geometrical distribution of the points with "moment-like" calculations, i.e. means and standard deviations, etc., are unlikely to be independent of existing linear measures of heart rate variability.

Chapter 3 of the book investigates Poincaré plot interpretation using a new oscillator model of heart rate variability. This chapter develops a physiologically plausible mathematical model of autonomic nervous control of heart rate based on a series of well-studied oscillations in heart rate. By employing the results described, the time series of intervals between heartbeats are able to be analytically determined. The properties of the Poincaré plot can then be derived. By analysing the Poincaré plot in terms of an underlying model of HRV, the theoretical basis of Poincaré plot morphology can be precisely related back to the model and therefore back to the physiological causes. This provides a deeper understanding of the Poincaré plot than has previously been possible. To validate the model, simulations of various autonomic conditions are compared to HRV data obtained from subjects under the prescribed conditions. For a variety of autonomic balances, the model generates

Poincaré plots that undergo morphological alterations strongly resembling those of actual heartbeat intervals.

Poincaré plot is valuable due to its ability to display nonlinear aspects of the data sequence. However, the problem lies in capturing temporal information of the plot quantitatively. The standard descriptors used in quantifying the Poincaré plot (*SD1*, *SD2*) measure the gross variability of the time series data. Determination of advanced methods for capturing temporal properties poses a significant challenge. Chapter 4 proposes a novel descriptor "Complex Correlation Measure (*CCM*)" to quantify the temporal aspect of the Poincaré plot. In contrast to *SD1* and *SD2*, the *CCM* incorporates point-to-point variation of the signal.

The asymmetry in heart rate variability is a visibly obvious phenomenon in the Poincaré plot of normal sinus rhythm. It shows the unevenness in the distribution of points above and below the line of identity, which indicates instantaneous changes in the beat-to-beat heart rate. The major limitation of the existing asymmetry definition is that it considers only the instantaneous changes in the beat-to-beat heart rate rather than the pattern (increase/decrease). Chapter 5 describes a novel definition of asymmetry considering the geometry of a 2D Poincaré plot. Based on the proposed definition, traditional asymmetry indices—Guzik's index (*GI*), Porta's index (*PI*) and Ehlers' index (*EI*)—have been redefined.

Chapter 6 of the book considers the segmented aspects of Poincaré plot remaining, on the one hand, the nonlinear properties of the system and, on the other hand, providing high resolution information about the time course and time correlations within a heart rate time series. These new approaches were successfully introduced in risk stratification.

This book should be of considerable help to researchers, professionals in medical device industries, academics and graduate students from a wide range of disciplines. The text provides a comprehensive account of recent research in this emerging field and we anticipate that the concepts presented here will generate further research in this field.

Melbourne, VIC, Australia — Ahsan Habib Khandoker
Melbourne, VIC, Australia — Chandan Karmakar
Melbourne, VIC, Australia — Michael Brennan
Jena, Germany — Andreas Voss
Melbourne, VIC, Australia — Marimuthu Palaniswami

Acknowledgements

The authors would like to gratefully acknowledge the contribution of Michael Brennan in Chaps. 2 and 3. The authors would also like to thank Claudia Fischer and Rico Schroeder of University of Applied Sciences Jena for their contributions in Chap. 6. The authors wish to gratefully acknowledge the financial support provided by the Australian Research Council and the Deutsche Forschungsgemeinschaft (DFG: Vo 505/8-1 and Vo 505/8-2) for the research presented in Chaps. 3–6, respectively.

Contents

Chapter 1
Introduction

Abstract The study of heart rate variability (HRV) focuses on the analysis of beat-to-beat fluctuations in heart rate and the diagnostic ability that these fluctuations provide. The series of time intervals between heartbeats, referred to as RR intervals, are measured over a period of anywhere from 10 min to 24 h and form the most commonly studied HRV time series (Rompelman et al., Med. Biol. Eng. Comput. **15**(3):233–239, 1977). The great majority of variability witnessed in heart rate records is due to the autonomic nervous system modulating heart rate (Jalife and Michaels, *Vagal Control of the Heart: Experimental Basis and Clinical Implications*, ed. by Levy and Schwartz, Futura, New York, 1994, pp. 173–205). Accordingly, attention has focused on HRV as a method of quantifying cardiac autonomic function. Vagal tone is the dominant influence under resting conditions and the majority of heart rate fluctuations are a result of vagal modulation (Chess et al., Am. J. Physiol. **228**:775–780, 1975). This provides clinicians with a reliable, non-invasive technique to monitor parasympathetic nervous activity. This, and other information that can be derived from HRV records, is of great importance to clinicians in the diagnosis, treatment and study of many illnesses related to the cardiovascular and autonomic systems.

1.1 Heart Rate Variability Techniques in Cardiology

The study of heart rate variability (HRV) focuses on the analysis of beat-to-beat fluctuations in heart rate and the diagnostic ability that these fluctuations provide. The series of time intervals between heartbeats, referred to as RR intervals, are measured over a period of anywhere from 10 min to 24 h and form the most commonly studied HRV time series [1]. The great majority of variability witnessed in heart rate records is due to the autonomic nervous system modulating heart rate [2]. Accordingly, attention has focused on HRV as a method of quantifying cardiac autonomic function. Vagal tone is the dominant influence under resting conditions and the majority of heart rate fluctuations are a result of vagal

A.H. Khandoker et al., *Poincaré Plot Methods for Heart Rate Variability Analysis*,
DOI 10.1007/978-1-4614-7375-6_1,

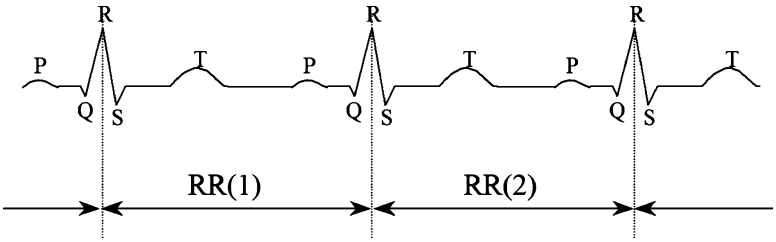

Fig. 1.1 The RR intervals are constructed from the intervals between successive R waves

modulation [3]. This provides clinicians with a reliable, non-invasive technique to monitor parasympathetic nervous activity. This, and other information that can be derived from HRV records, is of great importance to clinicians in the diagnosis, treatment and study of many illnesses related to the cardiovascular and autonomic systems.

1.1.1 The RR Intervals

In HRV, an ECG recording is taken and processed to locate the times of the heartbeats. This is done by locating the R waves in the ECG recordings, as they are the largest deflection and the wave that is able to be most precisely located. The times between successive R waves, the so-called RR intervals, is the time series that is a result of this process. Figure 1.1 details the construction of the RR intervals from the ECG. Short-term recordings or long-term recording of ECG can be made. Short-term recordings are usually at least 5 min long, but not substantially longer so as to guarantee stationarity. Long-term recordings are usually made for 24 h using a portable Holter recording device. Subjects who are healthy generally exhibit a large degree of variability in the RR interval records. This is due to the active operation of various control loops governing HRV. Subjects who are diseased tend to have reduced HRV. This may be a consequence of sections (or all) of the systems regulating heart rate being damaged. It might also be due to an alteration in autonomic nervous behaviour secondary to the effects of a disease not directly affecting the cardiovascular system. Figure 1.2 shows two example of RR interval records. The first (Fig. 1.2a) is of a healthy individual and a substantial degree of variability is present, including high- and low-frequency variability. The second (Fig. 1.2b) record is of heart failure subject who has suffered considerable damage to the parasympathetic nervous system. The level of variability in this record is much less than the healthy subject. The lack of variability is primarily of the high-frequency variety as would be expected for degraded parasympathetic function (parasympathetic control is the only quick-acting modulator of heart rate).

HRV analysis' primary purpose is to assess the function of the nervous system. It is specifically not interested in determining whether the heart, as an individual

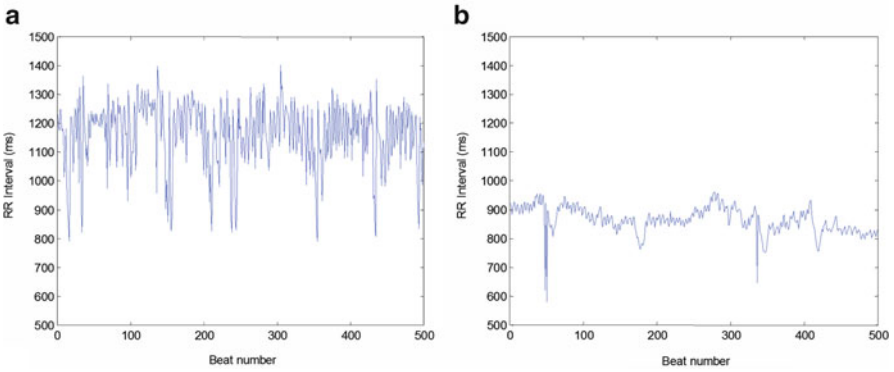

Fig. 1.2 RR interval series is of a healthy subject (**a**) and is of a subject with heart failure (**b**)

unit, produces normal sinus beats. Analysing the ECG directly best assesses problems with beat formation. HRV analysis assumes that each individual heartbeat is a normal heartbeat with a normal ECG signature. In other words, RR interval records should only contain heartbeats that were generated under sinus origin. This is known as being in "sinus rhythm". The autonomic nervous system directly controls the sinus nodes rate of firing. When an ectopic pacemaker controls the heart, the RR interval series don't contain any information on the function of the nervous system. In summary, HRV assesses the hearts rhythm, not how the heart actually forms a beat.

1.2 History of Heart Rate Variability

Since ancient times, it has been known that there exists considerable variability in heart rate even when the body is at rest. The fact that respiration was involved in generating the heart rate fluctuations was well known, even in very early times, because it causes easily noticeable short-term heart rate fluctuations. In 1733, Steven Hales was able to report that beat-to-beat HRV was synchronous with respiration [4]. Even though this cause and effect relationship was established, it took until much later for this fact to be put to a clinical use. That time came with the advent of the digital computer, which allowed long-term heart rate records to be collected and analysed. In 1965 Hon and Lee reported that heart rate patterns during foetal distress altered significantly earlier than did mean heart rate [5]. Bedside tests derived from short-term RR intervals were developed by Ewing to detect diabetic neuropathy [6]. Both these works were based on the known effects of respiration on heart rate. The next major development came as it was being realized that the rhythms in heart rate were more complicated than just respiration. The early 1970s saw a concentration of work describing the physiological rhythms embedded in the heart rate signal, including vasomotor activity, thermal regulation

and respiration [7–10]. In 1977 Wolf et al. showed that those with reduced HRV were at higher risk of postinfarction mortality [11]. In other words, patients who have survived a heart attack, but with little to no HRV, were in a high-risk category for low survival probability. Akselrod et al. used power spectral analysis to quantitatively evaluate cardiovascular control in 1981 [12]. The significance of this result was that heart rate records could be decomposed into separate signals that represented the operation of the different divisions of the autonomic nervous system. The emergence of spectral analysis allowed the autonomic basis of HRV to be explored [13, 14]. In the late 1980s the importance of HRV analysis became appreciated when it was shown to be a strong independent predictor of mortality after acute myocardial infarction [15–17]. As heart attack is a major problem in today's society, this result was received with much enthusiasm, as HRV is a cheap, non-invasive technique that could lead to significantly better health care and recovery management. Lately, with the development of nonlinear mathematics and chaos theory, it has come to light that HRV signals appear to have much in common with chaotic time series. Much has been made of this, and the various statistics used to characterize chaotic time series have been applied to HRV classification [18–20]. These results are not yet convincing, but the hope is that nonlinear dynamics may be able to unravel the high-level operation of the cardiovascular system, which is known to be a nonlinear system.

HRV is becoming a valuable tool for the clinician. Many studies have been done on the use of HRV as an indicator of disease, and an index of risk for sudden death. A brief outline of some of the major findings is as follows:

Myocardial Infarction: Myocardial infarction or "heart attack" is the death of tissue comprising the walls of the heart chambers (the myocardium). This usually occurs from lack of oxygen (ischaemia) due to low levels of blood flow to the heart. Myocardial ischemia caused by coronary occlusion has been shown to be accompanied by excited sympathetic activity [21]. Autonomic activity has been shown to be closely related to susceptibility to ventricular fibrillation [22]. In general, increased sympathetic activity was found to predispose to malignant ventricular arrhythmias, and increased parasympathetic activity provided a protective and antifibrillatory effect [23]. These findings have provided the impetus to study the use of HRV as a non-invasive tool to evaluate alterations of autonomic control in patients following myocardial infarction [24–34].

Risk Stratification Postinfarction: Risk stratification is designed for early identification of the patient at high risk for complications. The aim is to implement appropriate prophylactic therapy to prevent re-infarction or sudden death. Of deaths following infarction, 75% are due to an arrhythmic mechanism and the remainder are due to myocardial pump failure [35]. HRV is a very useful prognostic index, probably because it reflects reduced vagal and increased sympathetic activity [16, 36]. A recent major study has shown that reduced 24 h SDRR is a powerful independent predictor of cardiac events following arrhythmic myocardial infarction [37].

Hypertension: Hypertension is the medical term for high blood pressure. Several functional alterations of the cardiovascular system are frequently found in hypertensive patients. These alterations may increase their risk beyond that induced by elevated blood pressure alone. Left ventricular hypertrophy (LVH), which is a swelling of the left ventricle, secondary to hypertension, is one such example. Reduced high-frequency HRV has been shown to correlate with LVH and a worse prognosis after arrhythmic myocardial infarction [38].

Diabetes: Diabetes can cause severe autonomic dysfunction that can be responsible for several disabling symptoms, including sudden cardiac death (SCD) [39]. Although traditional measures of autonomic function are able to document the presence of neuropathy, in general they are only abnormal when there is severe symptomatology. Thus, by the time changes in function are evident, the natural course of autonomic neuropathy is well established. HRV analysis is able to detect the change in autonomic balance before neuropathy is established [40].

Sudden Cardiac Death: Ventricular tachyarrhythmias represent a leading cause of SCD in the community [34, 41]. The study by Farrell et al. [42] reported that decreased HRV was more predictive of subsequent arrhythmic events than the presence of late potentials (Holter-derived arrhythmias treadmill exercise test results or left ventricular ejection fraction). In multivariate analysis of combinations of risk factors, the combination of late potentials recorded by the signal averaged ECG and reduced HRV was more predictive than any other combination.

Coronary Artery Disease: Studies using short-term measures of HRV demonstrated an inverse relationship between cholesterol and vagal activity [43]. This raises the possibility that a high cholesterol level may directly or indirectly influence cardiac autonomic tone.

Heart Failure: Conflicting evidence as to the correlation between the degree of myocardial damage sustained following a myocardial infarction and HRV in humans [44, 45]. In patients with heart failure, one study showed a significant linear correlation between HRV and ejection fraction [46] while others have not [45].

Smoking and Alcohol: Smokers have increased sympathetic and reduced vagal activity as measured by HRV analysis [47]. HRV is reduced following ingestion of alcohol suggesting sympathetic activation and/or parasympathetic withdrawal [48]. Malapas et al. [49] have demonstrated vagal neuropathy in men with chronic alcohol dependence using 24 h HRV analysis.

1.3 Physiological Basis of HRV Analysis

Several physiological rhythms modulate heart rate via the autonomic nervous system. Instantaneous heart rate represents the total summation of all the effects on the autonomic nervous system. In the normal healthy subject there are several reflexes that operate in a simultaneous manner. These reflexes contain rhythms that

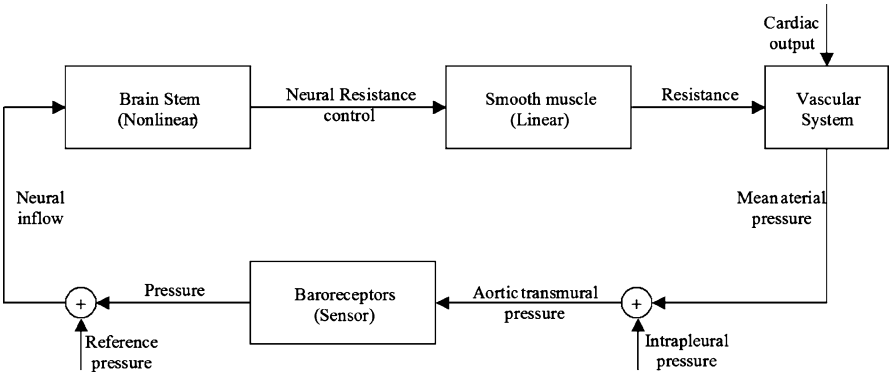

Fig. 1.3 The process which generates vasomotor oscillations

are transmitted to the cardioregulatory systems in the brain and are effected in heart rate. The correspondence between these rhythms and branches of autonomic nervous system allows HRV analysis to provide information on the function of the different sections of the autonomic nervous system.

Respiration: Respiratory sinus arrhythmia (RSA) refers to the clinical variation in heart rate associated with breathing. Breathing causes disturbances in blood pressure, which are sensed by the baroreceptors. The baroreflex arc processes the changes in blood pressure and causes a corresponding fluctuation in heart rate [8]. Because respiration is roughly periodic with a relatively short period (about 3 s), the fluctuations are mediated solely by the parasympathetic nervous system. As a result, parasympathetic control is able to operate on a rapid time scale, whereas the sympathetic systems cannot. Some researchers believe that the magnitude of sinus arrhythmia provides an index of the level of cardiac vagal activity [50, 51]. RSA also relies on the baroreceptor reflex to operate and therefore assess the functioning of the baroreceptor reflexes. Whether RSA indicates the entire level of parasympathetic activity or only the modulatory portion thereof is a matter that is under some debate [52].

Vasomotor Oscillations: Vasomotor oscillations are a low-frequency spontaneous oscillation in blood pressure with a period of roughly 10 s. Constricting of the cross-sectional area of the arteries via smooth muscle activation regulates blood flow to different regions of the body. This process is controlled in a nonlinear manner by the brain stem and the baroreceptors. Due to delays in the processing system and the properties of smooth muscle activation, a spontaneous oscillation of roughly 10 Hz appears in blood pressure. This oscillation is detected by the baroreceptors and is superimposed onto the heart rate by the baroreceptor reflex arc [8]. Figure 1.3 shows the process diagrammatically. Vasomotor oscillations are mediated by the sympathetic nervous system [12, 53, 54]. There is debate

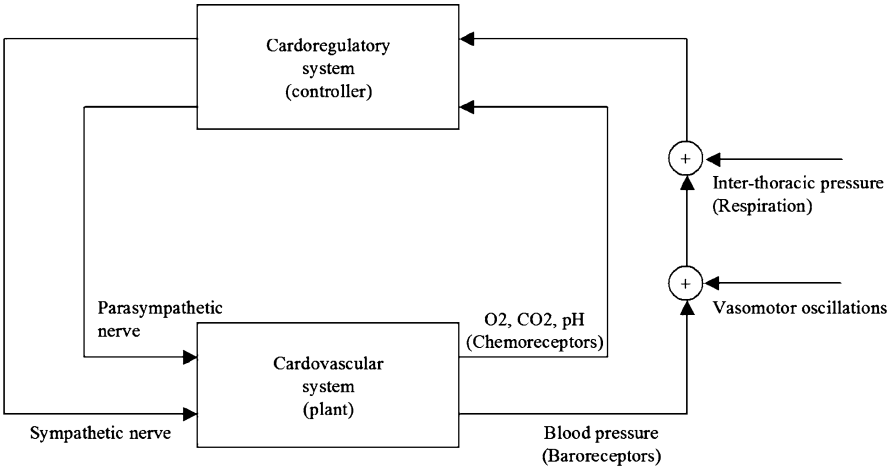

Fig. 1.4 The cardiovascular control system as a feedback control system

about whether they are also mediated by the parasympathetic system [52,55] and at this stage the results are inconclusive. This is a gap in the knowledge of how the sympathetic nervous system affects heart rate and requires further research.

Sympathetic-Vagal Interactions: There is usually a balance between both divisions of the autonomic nervous system with heart rate reflecting the net effect of the two opposing arms of the system. At rest the vagal system is dominant; however with increasing levels of activity the activity of the vagus decreases and the sympathetic increases. However, although heart rate reflects the combined activity of both arms of the autonomic nervous system, it cannot be used to gauge the individual effect of the vagal or sympathetic system. It has been shown that the activity of the vagus nerve is accentuated when heart rate has been accelerated by sympathetic stimulation [56].

Heart Rate Control: Short-term heart rate control can be considered as a control system where the physiological system is broken down into the following components:

- Cardiovascular system: the plant
- Cardioregulatory system: the controller
- Autonomic nervous system: control inputs/outputs
- Vasomotor and respiration: disturbances

Figure 1.4 shows these components as a feedback control system. The disturbances in blood pressure are transmitted via the autonomic nervous system to the controller, which causes sympathetic and parasympathetic activity to fluctuate in rhythm. The fluctuations in blood pressure are therefore seen in heart rate also.

1.4 Analysis Methods

The HRV indices can be divided into three major categories: time domain, frequency domain and nonlinear. The time-domain indices were developed quite early in the field and are still very popular. The frequency-domain indices were developed later and allow the variability to be divided into separate rhythms based on frequency. The nonlinear methods are based on the premise that HRV is a chaotic time series. They are the latest development and a very active field at present. To emphasize that edited RR intervals are being analysed, often the RR intervals are quoted as NN intervals. The NN intervals are the normal-to-normal intervals that result from editing ectopic beats and noise from the RR intervals. Either short-term or long-term recordings are analysed.

1.4.1 Time Domain

The time-domain indices of HRV measure the statistical properties of RR intervals, or the delta RR intervals. The delta RR intervals are the series of differences between successive RR intervals. The most common class of time-domain indices are based on statistical measurements of the intervals. Various "geometric" methods also exist, in which various measurements are made of the geometry of patterns made by the intervals. First we describe the most popular statistical techniques.

1.4.1.1 Statistical Techniques

The statistical techniques are based on various moments of the RR intervals and the delta RR intervals:

SDRR The standard deviation of the RR intervals. This is a measure of total variability of the RR intervals. Low values indicate practically no HRV and this property alone has made it possibly the most used index in the literature [57–68]. SDRR increases as the length of time the measurement is taken over increases. It is able to be used for both long-term and short-term recordings, although it is not advised for use on short-term recordings due to dubious reproducibility [55]. Normal subjects have a value of 141+/−39 ms (mean +/− standard deviation) for long-term recordings [55].

SDARR The standard deviation of the means of short-term (5 min) recordings. This is a measure of variability with period over 5 min. This measure is obviously only appropriate for long-term HRV measurements and is usually performed on 24 h records [69–74]. Normal subjects have a value of 127+/−35 ms [55].

RMSSD Root mean square of the successive differences of the RR intervals. This is a measure of short-term HRV. It is also given the name SDSD, which stands for standard deviation of successive differences. The measure is best used on long-term recordings, but is often employed for short-term recordings. It is the most common time-domain measure of short-term HRV [29, 69, 75–80]. Normal subjects have an *RMSSD* value of $27+/-12$ ms [55]. As short-term variability is mediated purely by the parasympathetic system, *RMSSD* measures parasympathetic modulation of heart rate.

NN50 The number of interval differences of successive NN intervals that are greater than 50 ms. This is a measure of short-term HRV. This measure correlates highly with *RMSSD*. *NN*50 measures parasympathetic modulation of heart rate. *RMSSD* has better immunity to ectopic beats and has nicer statistical properties, so it is the preferred measure of short-term HRV.

pNN50 The fraction of *NN*50 intervals as a proportion of the total number of NN intervals. This is another measure of short-term HRV. This measure correlates very highly with *RMSSD* . For the same reasons as *NN*50 *RMSSD* is a preferred method of measuring short-term HRV; however this measure is still quite often seen in the literature [40, 81–84].

1.4.1.2 Geometric Techniques

The geometric techniques convert the RR interval data into a geometric pattern. Various qualities of the shape or pattern are measured and form the HRV indices. The geometric techniques generally have better performance on poorly edited data. The most popular techniques are:

HRV Triangular Index: First the sample density histogram is constructed. The most frequent RR interval length is established and denoted by where is the most frequent RR interval length. The triangular index is given by dividing the total number of RR intervals by the most frequent RR interval length. The HRV triangular index has a value of $37+/-15$ in normal subjects. It is a measure of total HRV, but it takes into account long-term fluctuations more than the short-term [17].

Poincaré Plot: The Poincaré plot is a scatter plot of the RR intervals against the next RR interval. The plot resembles a cloud oriented along the line of identity. The shape of the cloud provides a very useful description of HRV [85–93]. The length of the plot corresponds to the level of long-term variability and width of the plot measures short-term variability. Poincaré width is considered a pure measure of parasympathetic activity [94]. Figure 1.5 displays a typical Poincaré plot. Currently, Poincaré plot analysis is a very active field. The main problem with Poincaré plot analysis is the lack of clear quantitative descriptions of the plot.

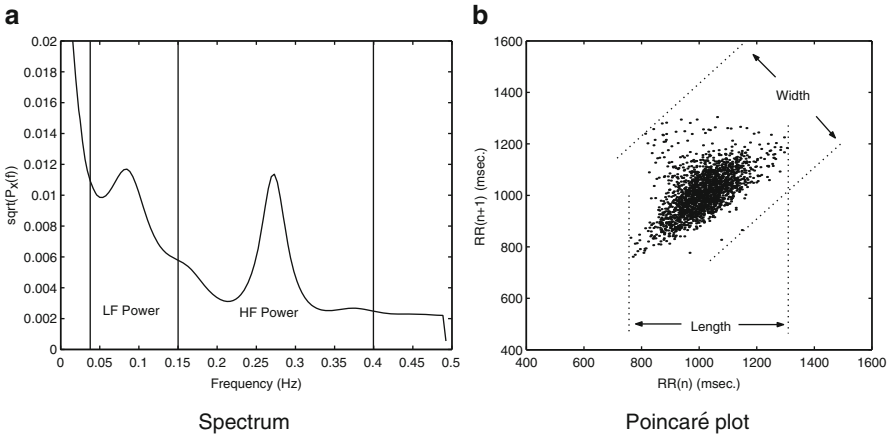

Fig. 1.5 Plot (**a**) is the HRV spectrum. The respiratory component near 0.3 Hz and the vasomotor component near 0.1 Hz are clearly present. Plot (**b**) is the Poincaré plot of the same data. The length and the width are shown graphically on the plot. Figure adapted from Brennan et al. [118]

1.4.2 Frequency Domain

Many methods exist for estimating the spectrum from the RR intervals [1, 95–102]. The methods include both parametric and non-parametric techniques. While parametric methods obtain more accuracy on smaller data sets, the selection of model order can be difficult to automate [55]. Spectral analysis of heart rate consists of first calculating the power spectral density (PSD) of the RR intervals. Secondly, the PSD is broken into separate frequency bands as Fig. 1.5(a) details. Thirdly, the power in each band is calculated by integrating the PSD within the band limits. The bands are placed so as to measure useful information on the autonomic nervous system. The selection of the limits of each band has been standardized and depends on whether short-term or long-term recordings are being processed.

1.4.2.1 Short-Term Recordings

There are three main spectral components in a short-term recording of which only two are of physiological importance [8, 10, 12, 13, 53, 103]. They are:

- HF Power: high-frequency power (0.15–0.4 Hz). HF power is a measure of parasympathetic activity [12, 14, 53, 94]. The band is roughly centred on the average respiration frequency for a normal subject. For a normal subject, a peak in the PSD curve exists in this band at roughly 0.3 Hz caused by respiration .
- LF Power: low-frequency power (0.04–0.15 Hz). LF power is the subject of some controversy. Some consider it to be a measure of both sympathetic and parasympathetic activities [54, 103, 104], while others consider it a pure measure

of sympathetic activity [12, 105]. For a normal subject, a peak exists in the LF band caused by vasomotor oscillations. The band is roughly centred on the frequency of the vasomotor oscillations, at roughly 0.1 Hz.
- VLF Power: very-low-frequency power (0–0.04 Hz). VLF does not correlate with any known physiological rhythms. The VLF band is basically treated as noise and effects due to nonstationarity. No peaks are present in this band.

The total power TOT is given by VLF + HF + LF. The HF and LF components are often used to quantify the autonomic activity of the sympathetic and parasympathetic branches. The balance between the two systems is often quantified by BAL = LF/HF. However, this quantity is interpreted differently by those who consider LF power to reflect sympathetic and parasympathetic activity. In this case LF/HF represents the sympathetic activity. Often researchers normalize the indices by dividing LF and HF by TOT. This gives more consistent results, especially when comparing subjects under different autonomic stresses.

1.4.2.2 Long-Term Recordings

Long-term recordings used for spectral analysis are usually 24 h recordings. An extra band is included for long-term recordings:

- HF: same as for short-term recordings.
- LF: same as for short-term recordings.
- VLF: very-low-frequency band (0.003–0.04 Hz). The VLF band only extends down to 0.003 Hz.
- ULF: ultra-low-frequency band (0–0.003 Hz). The ULF band is included for long-term recordings.

The physiological mechanisms that generate the peaks in the HF and LF bands still produce peaks in long-term recordings. However, as the oscillations of these systems are not stationary over long periods of time, the modulations are averaged over the 24 h and detail is lost. Therefore, the use of LF and HF is not recommended for 24 h records. The LF and HF bands normally only account for 5% of the variability over 24 h. The physiological correlates of the VLF and ULF components are not well understood at present [55].

1.4.3 Nonlinear Dynamics

Considering the variety of factors influencing heart rate, e.g. respiration or mental load, it becomes apparent that heart rate regulation is one of the most complex systems in humans [106]. Many techniques suggested by nonlinear dynamics have been applied to the classification of HRV. The application of these techniques is motivated by the fact that the control systems for HRV have been shown to be

nonlinear [107–110] because of its high complexity and the nonlinear interactions between the physiological subsystems. Several of those indices have been proven to be of diagnostic relevance or have contributed to risk stratification.

The following nonlinear methods/indices have been employed [106]:

- Fractal measures (e.g. power-law correlation, detrended fluctuation analysis, multifractal analysis)
- Entropy measures (e.g. approximate entropy, sample entropy, compression entropy)
- Symbolic dynamics measures and finally
- Poincaré plot

Even if these methods may lead to new insights into HRV changes under various physiological and pathological conditions, the lacking standards of preprocessing the heart rate time series and calculating the different indices and in addition the problem of interpreting the physiological meanings of their indices prevented (yet) a major breakthrough in clinical and ambulatory care.

However, methods from nonlinear dynamics provide additional prognostic information and complement traditional time and frequency-domain analyses of HRV. In this context the Poincaré plot analyses play a more and more important role and—as an advantage—are easier to understand and interpret and are (at least as simple plots) already widespread in Holter ECG analysis.

Chapter 2
Quantitative Poincaré Plot

Abstract Poincaré plot is a geometrical representation of a time series in a Cartesian plane. Points of the plot are duplets of the values of the time series and the distance (in number of values) between values of each duplet is the *lag* of the plot. Statistically, *lag-1* Poincaré plot displays the correlation between consecutive samples in a graphical manner. It has been shown that Poincaré plot reveals patterns of heart rate dynamics resulting from nonlinear processes (Tulppo et al., Am. J. Physiol. **271**:H244–H252, 1996; Brennan et al., IEEE Trans. Biomed. Eng. **48**:1342–1347, 2001). The *lag-1* RR interval Poincaré plot, a two-dimensional plot constructed by plotting consecutive RR intervals, is a representation of RR time series on phase space or Cartesian plane (Liebovitch and Scheurle, Complexity **5**:34–43, 2000). It is extensively used for qualitative visualization of physiological signals. Poincaré plot is commonly applied to assess the dynamics of heart rate variability (Tulppo et al., Am. J. Physiol. **271**:H244–H252, 1996; Acharya et al., Med. Biol. Eng. Comput. **44**(12):1031–1051, 2006; Tulppo et al., Am. J. Physiol. **247**:H810–H816, 1998; Toichi et al., J. Auton. Nerv. Syst. **62**:79–84, 1997; Hayano et al., Nephrol. Dial. Transplant. **14**:1480–1488, 1999). The quantitative analysis of Poincaré plot predominantly means the mathematical characterization of the shape of the plot. In the following sections we will discuss both the qualitative and quantitative techniques of Poincaré plot for analysing HRV signal.

2.1 Introduction

Poincaré plot is a geometrical representation of a time series in a Cartesian plane. Points of the plot are duplets of the values of the time series and the distance (in number of values) between values of each duplet is the *lag* of the plot. Statistically, *lag-1* Poincaré plot displays the correlation between consecutive samples in a graphical manner. It has been shown that Poincaré plot reveals patterns of heart rate dynamics resulting from nonlinear processes [111, 112]. The *lag-1* RR interval Poincaré plot, a two-dimensional plot constructed by plotting consecutive

A.H. Khandoker et al., *Poincaré Plot Methods for Heart Rate Variability Analysis*,
DOI 10.1007/978-1-4614-7375-6_2,

RR intervals, is a representation of RR time series on phase space or Cartesian plane [113]. It is extensively used for qualitative visualization of physiological signals. Poincaré plot is commonly applied to assess the dynamics of heart rate variability [111,114–117]. The quantitative analysis of Poincaré plot predominantly means the mathematical characterization of the shape of the plot. In the following sections we will discuss both the qualitative and quantitative techniques of Poincaré plot for analysing HRV signal.

2.2 Visualization of HRV Using Poincaré Plot

The visual analysis of Poincaré plot is termed as qualitative analysis technique. In HRV analysis, the qualitative technique was first used to visualize the complex HRV pattern which could be produced by alterations and interactions of autonomic and cardiovascular systems accompanying heart failure [91]. The result of qualitative analysis provides additional information to the standard time-domain analysis of HRV signal. It introduced the use of Poincaré plot to characterize the pattern of RR intervals of a healthy heart. Moreover, the visual analysis of RR intervals used to distinguish patients with advanced heart failure from healthy individuals [91].

Comet

This pattern represents the lengthening of RR intervals which indicates increased beat-to-beat variability as well as overall range for healthy subjects (Fig. 2.1) [91].

Torpedo

This indicates that the change between consecutive RR intervals is minimal. However, this minimal deviation does not indicate the fixed heart rate but suggests gradual change in heart rate while maintaining small beat-to-beat variability (Fig. 2.2) [91].

Fan

It has a small increase in RR interval length (i.e. shorter overall range) which is associated with greater dispersion in consecutive RR intervals (Fig. 2.3) [91].

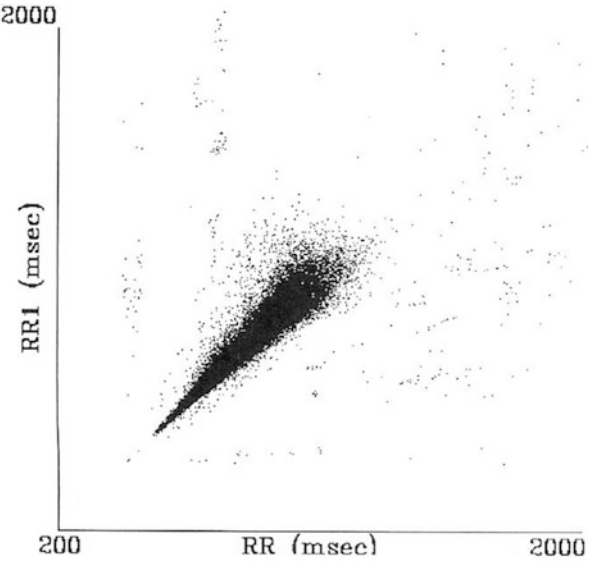

Fig. 2.1 Poincaré plot of RR intervals of healthy patient with comet pattern. Figure adapted from Woo et al. [91]

Complex

This pattern creates stepwise clusters of points with distinct gaps between the clusters. The stepwise change in RR intervals represents lack of graded relationship between successive RR intervals and linked to nonlinear behaviour (Fig. 2.4) [91].

2.3 Quantification of Poincaré Plot of RR Interval

Quantitative analysis of Poincaré plot quantifies the differences among the shape of the plots. It is a mathematical approach to characterize the plot. The RR interval Poincaré plot typically appears as an elongated cloud of points oriented along the line of identity ($RR_n = RR_{n+1}$). Hence, the shape of the plot is measured as the dispersion of points perpendicular to the line of identity, termed as short-term variability, and along the line of identity, termed as long-term variability [89, 111]. Approaches of quantifying Poincaré plot are described in the following sections.

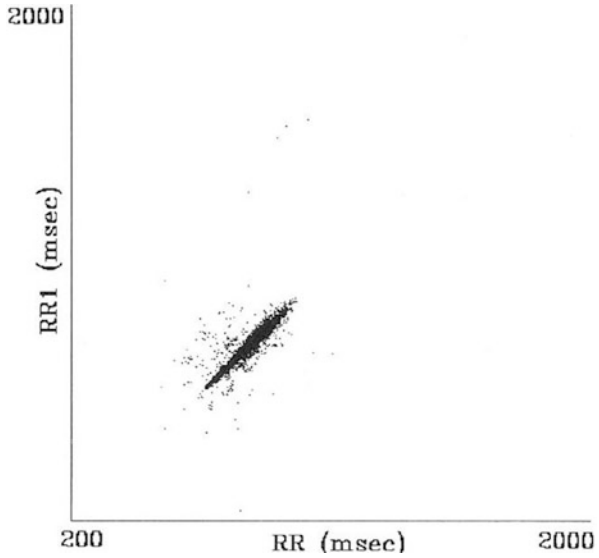

Fig. 2.2 Poincaré plot of RR intervals of heart failure patient with torpedo pattern. Figure adapted from Woo et al. [91]

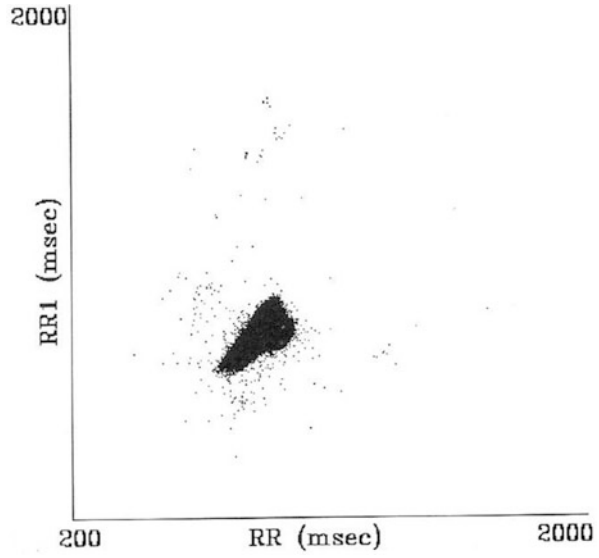

Fig. 2.3 Poincaré plot of RR intervals of heart failure patient with fan pattern. Figure adapted from Woo et al. [91]

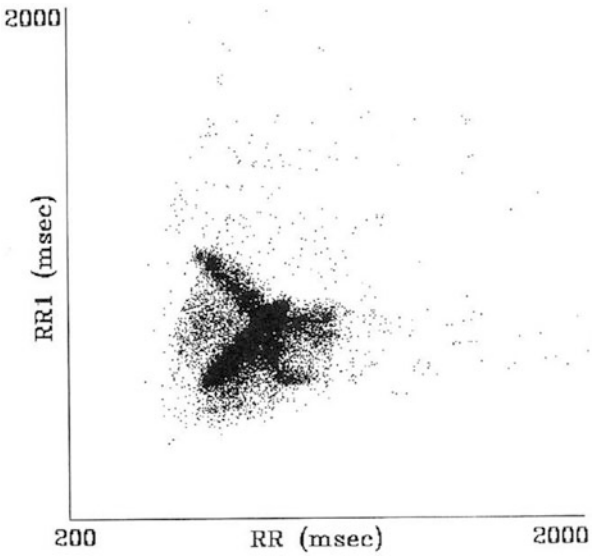

Fig. 2.4 Poincaré plot of RR-intervals of heart failure patient with complex pattern. Figure adapted from Woo et al. [91]

2.3.1 Ellipse-Fitting Technique

Most researchers have adopted the ellipse-fitting technique to characterize the Poincaré plot mathematically as shown in Fig. 2.5. The major axis of the fitted ellipse is aligned with the line of identity, line passes through origin with slope 45°, and the minor axis is perpendicular to the line of identity which has a slope of 135° and passes through centroid of the plot. Hence, the major and minor axis of the fitted ellipse can be expressed as

$$RR_n = RR_{n+1} \tag{2.1}$$

and

$$RR_n + RR_{n+1} = 2\overline{\mathbf{RR}}, \tag{2.2}$$

where **RR** represents the RR interval series used in the Poincaré plot and $\overline{\mathbf{RR}}$ represents the mean value of RR interval series. In the ellipse-fitting technique, the dispersion of the points along minor axis measures the width of the plot, whereas the dispersion of the points along the major axis measures the length of the plot. The distance of ith point of the plot, $P(RR_i, RR_{i+1})$, from major and minor axis, respectively, can be expressed as

$$D_{i(\min)} = \frac{RR_i - RR_{i+1}}{\sqrt{2}} \tag{2.3}$$

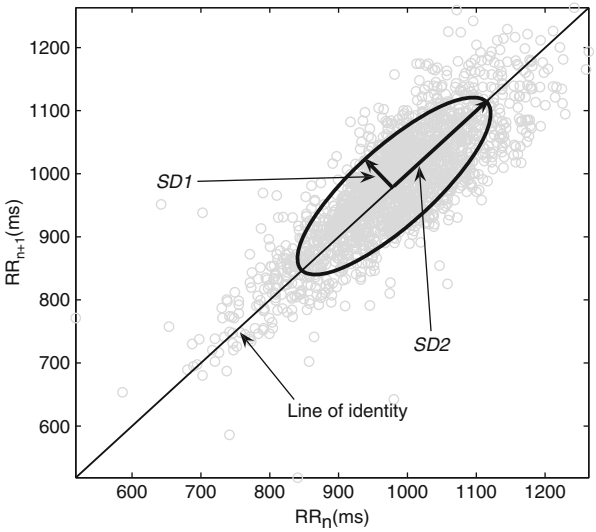

Fig. 2.5 A standard Poincaré plot of RR intervals of a healthy person ($N = 3000$).The *diagonal solid line* represents the line of identity

and

$$D_{i(\text{maj})} = \frac{RR_i + RR_{i+1} - 2\overline{\mathbf{RR}}}{\sqrt{2}}. \tag{2.4}$$

Finally, the short-term and long-term variability of the plot can be expressed as

$$SD1 = \sqrt{\frac{1}{N-1}\sum_{i=1}^{N-1} D_{i(\text{min})}^2} \tag{2.5}$$

and

$$SD2 = \sqrt{\frac{1}{N-1}\sum_{i=1}^{N-1} D_{i(\text{maj})}^2}, \tag{2.6}$$

where N is the number of RR intervals in the plotted HRV signal.

Relation of *SD1* and *SD2* with Linear HRV Indices

The standard deviation of the RR intervals, denoted by SDRR, is often employed as a measure of overall HRV as shown by [112]. It is defined as the square root of the variance of the RR intervals

$$\begin{aligned}
\text{SDRR} &= \sqrt{\frac{1}{N}\sum_{i=1}^{N}(RR_i - \overline{\mathbf{RR}})^2} \\
&= \sqrt{E[(\mathbf{RR} - \overline{\mathbf{RR}})^2]} \\
&= \sqrt{E[\mathbf{RR}^2 - 2\mathbf{RR}\overline{\mathbf{RR}} + \overline{\mathbf{RR}}^2]} \\
&= \sqrt{E[\mathbf{RR}^2] - 2E[\mathbf{RR}]\overline{\mathbf{RR}} + \overline{\mathbf{RR}}^2]} \\
&= \sqrt{\overline{\mathbf{RR}^2} - 2\overline{\mathbf{RR}}^2 + \overline{\mathbf{RR}}^2} \\
&= \sqrt{\overline{\mathbf{RR}^2} - \overline{\mathbf{RR}}^2}, \qquad (2.7)
\end{aligned}$$

where $\overline{\mathbf{RR}} = E[\mathbf{RR}]$.

The standard deviation of the successive differences of the RR intervals, denoted by SDSD, is an important measure of short-term HRV. It is defined as the square root of the variance of the sequence $\Delta\mathbf{RR}$, where each element of $\Delta\mathbf{RR}$, $\Delta RR_i = RR_i - RR_{i+1}$:

$$\text{SDSD} = \sqrt{\frac{1}{N}\sum_{i=1}^{N}(\Delta RR_i - \overline{\Delta\mathbf{RR}})^2},$$

where $\overline{\Delta\mathbf{RR}} = E[\Delta\mathbf{RR}] = E[RR_i] - E[RR_{i+1}] \equiv 0$ for stationary intervals. Considering this wide-sense stationarity the above equation can be expressed as

$$\begin{aligned}
\text{SDSD} &= \sqrt{\frac{1}{N}\sum_{i=1}^{N}\Delta RR_i{}^2} \\
&= \sqrt{E[\Delta\mathbf{RR}^2]} \\
&= \sqrt{\overline{\Delta\mathbf{RR}^2}}. \qquad (2.8)
\end{aligned}$$

Now using Eqs. 2.3 and 2.5 *SD1* can be expressed as

$$\begin{aligned}
SD1 &= \sqrt{\frac{1}{N-1}\sum_{i=1}^{N-1}\frac{(RR_i - RR_{i+1})^2}{2}} \\
&= \sqrt{\frac{1}{2}E[(RR_i - RR_{i+1})^2]} \\
&= \sqrt{\frac{1}{2}E[\Delta\mathbf{RR}^2]}
\end{aligned}$$

$$= \sqrt{\frac{1}{2}\overline{\Delta \mathbf{RR}^2}}$$
$$= \frac{1}{\sqrt{2}}\mathrm{SDSD}. \tag{2.9}$$

Similarly, using Eqs. 2.4 and 2.6, *SD2* can be expressed as

$$\begin{aligned}
SD2 &= \sqrt{\frac{1}{N-1}\sum_{i=1}^{N-1}\frac{(RR_i+RR_{i+1}-2\overline{\mathbf{RR}})^2}{2}} \\
&= \sqrt{\frac{1}{N-1}\sum_{i=1}^{N-1}\frac{RR_i{}^2+RR_{i+1}{}^2+4\overline{\mathbf{RR}}^2+2RR_iRR_{i+1}-4RR_{i+1}\overline{\mathbf{RR}}-4RR_i\overline{\mathbf{RR}}}{2}} \\
&= \sqrt{\frac{1}{N-1}\sum_{i=1}^{N-1}\frac{2RR_i{}^2+2RR_{i+1}{}^2+4\overline{\mathbf{RR}}^2-4RR_{i+1}\overline{\mathbf{RR}}-4RR_i\overline{\mathbf{RR}}-(RR_i-RR_{i+1})^2}{2}} \\
&= \sqrt{\frac{1}{N-1}\sum_{i=1}^{N-1}\frac{2RR_i{}^2+2RR_{i+1}{}^2+4\overline{\mathbf{RR}}^2-4RR_{i+1}\overline{\mathbf{RR}}-4RR_i\overline{\mathbf{RR}}-\Delta\mathbf{RR}^2}{2}} \\
&= \sqrt{\frac{2E[RR_i{}^2]+2E[RR_{i+1}{}^2]+4\overline{\mathbf{RR}}^2-4E[RR_{i+1}]\overline{\mathbf{RR}}-4E[RR_i]\overline{\mathbf{RR}}-E[\Delta\mathbf{RR}^2]}{2}} \\
&= \sqrt{\frac{2\overline{\mathbf{RR}^2}+2\overline{\mathbf{RR}^2}+4\overline{\mathbf{RR}}^2-4\overline{\mathbf{RR}}^2-4\overline{\mathbf{RR}}^2-\overline{\Delta\mathbf{RR}^2}}{2}} \\
&= \sqrt{\frac{4\overline{\mathbf{RR}^2}-4\overline{\mathbf{RR}}^2-\overline{\Delta\mathbf{RR}^2}}{2}} \\
&= \sqrt{2(\overline{\mathbf{RR}^2}-\overline{\mathbf{RR}}^2)-\frac{1}{2}\overline{\Delta\mathbf{RR}^2}} \\
&= \sqrt{2\mathrm{SDRR}^2-\frac{1}{2}\mathrm{SDSD}^2}
\end{aligned} \tag{2.10}$$

using assumptions $E[RR_i]=E[RR_{i+m}]$ and $E[RR_i^2]=E[RR_{i+m}^2]$. This shows that *SD1* and *SD2* of Poincaré plot are directly related to the basic statistical measures, standard deviation of RR interval (SDRR) and standard deviation of the successive difference of RR interval (SDSD) [112].

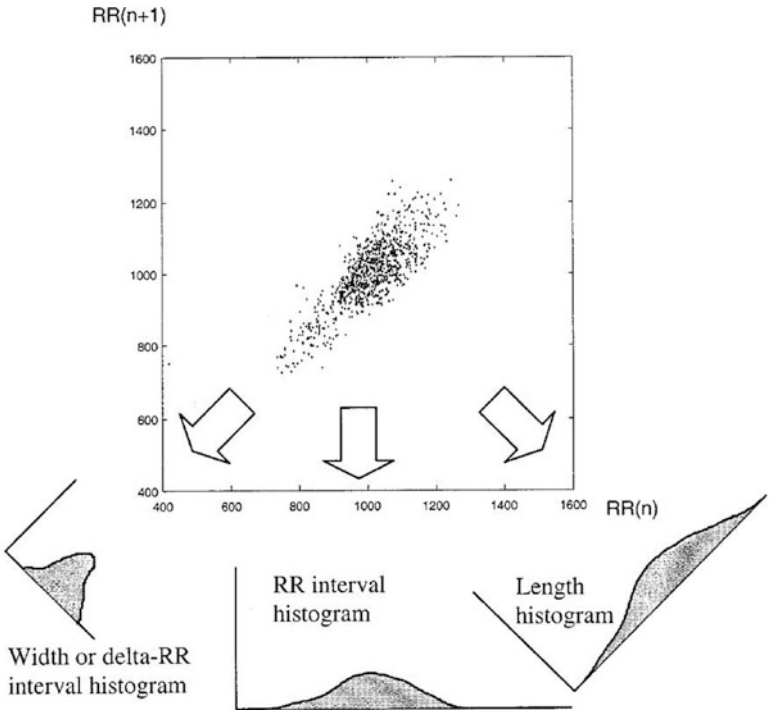

Fig. 2.6 Details the construction of the width (or delta-RR interval) histogram, the RR interval histogram and the length histogram. Each of these histograms is a projection of the points of the Poincaré plot. Figure adapted from Brennan et al. [112]

2.3.2 Histogram Techniques

Intuitively, histogram is a graphical way to summarize the distribution of a univariate data set. It organizes a group of data points into user-specified ranges. Adapting the histogram technique to quantify Poincaré plot requires converting 2D Poincaré plot signal into a univariate signal, which is achieved through various projections of the points. Therefore, in histogram technique the shape of the Poincaré plot is quantified by measuring the statistical properties of the various projections of the plot [87, 89, 94]. Figure 2.6 shows three main projections of the plot.

RR Interval Histogram

The histogram of the Poincaré plot points projected onto the X axis or the Y axis. Since the points in *lag-1* Poincaré plot represent the consecutive RR intervals, projecting them onto one of the axes represents the RR interval series (**RR**). The RR interval histogram is usually quantified by the mean and standard deviation, which

correspond directly to the same measures of **RR** denoted by $\overline{\mathbf{RR}}$ and SDRR. Therefore, this projection of Poincaré plot provides summary information on the overall HRV characteristics.

"Width" or Delta-RR Interval Histogram

This is the histogram of the Poincaré plot points projected on the line of identity. The X value of the point is on the line of identity while the Y value of the point corresponds to the perpendicular distance of the point from the line of identity. It is not exactly equivalent to the delta-RR interval histogram; the abscissa has been scaled by the factor $1/\sqrt{2}$. As expected of the ΔRR intervals, the histogram has a zero mean. Therefore, the standard deviation of the width histogram is equal to *SD1*, which is a scaling of the SDSD measure as shown in Eq. 2.9. This histogram provides summary information on the short-term characteristics.

"Length" Histogram

This histogram is obtained by projecting the Poincaré plot points perpendicular onto the line of identity. The histogram is described mathematically by the distribution of $x2$ and the standard deviation is, therefore, equivalently equal to *SD2*. Consequently, due to its connection with *SD2*, the length histogram portrays the long-term characteristics of HRV.

2.4 Relationship Between Poincaré Shape and Linear HRV Measure

The autocorrelation function is an important measure of HRV simply because its Fourier transform is the power spectrum of intervals. The autocorrelation function of the RR intervals is defined by Brennan et al. [112] as

$$\gamma(m) = E[RR_i RR_{i+m}], \tag{2.11}$$

where m is the time delay. Brennan et al. [112] have also defined *SD1* and *SD2* with respect to autocorrelation function as follows:

$$SD1^2 = \gamma_{RR}(0) - \gamma_{RR}(1) \tag{2.12}$$

$$SD2^2 = \gamma_{RR}(0) + \gamma_{RR}(1) - 2\overline{RR}^2, \tag{2.13}$$

where $\gamma_{RR}(0)$ and $\gamma_{RR}(1)$ are the autocorrelation functions for *lag-0* and *lag-1* RR interval and $\overline{RR}$ is the mean of RR intervals. From Eqs. 2.12 and 2.13, it is obvious that the measures *SD1* and *SD2* are derived from the correlation (at *lag 0* and *1*) and mean of RR interval time series. The above equation sets are derived for unit time delay Poincaré plot. Researchers have shown interest in plots with different time delays to get a better insight in the time-series signal. Usually the time delay is a multiple of the cycle length or the sampling time of the signal [118]. The dependency among the variables is controlled by the choice of time delay, and the most conventional analysis is performed with higher-order linear correlation between points. In the case of plotting the 2D phase space with *lag-m* the equations for *SD1* and *SD2* can be represented as

$$\begin{aligned} SD1^2 &= \gamma_{RR}(0) - \gamma_{RR}(m) \\ \Rightarrow SD1 &= F(\gamma_{RR}(0), \gamma_{RR}(m)) \end{aligned} \tag{2.14}$$

and

$$\begin{aligned} SD2^2 &= \gamma_{RR}(0) + \gamma_{RR}(m) - 2\overline{RR}^2 \\ \Rightarrow SD2 &= F(\gamma_{RR}(0), \gamma_{RR}(m)), \end{aligned} \tag{2.15}$$

where $\gamma_{RR}(m)$ is the autocorrelation function for *lag-m* RR interval. This implies that the standard descriptors for any arbitrary m lag Poincaré plot is a function of autocorrelation of the signal at *lag-0* and *lag-m*.

2.5 Conclusion

Poincaré plot is a popular HRV analysis tool among clinicians due to its ability to visually represent nonlinear dynamics of HRV. We explained and derived the development of Poincaré plot both as a qualitative and quantitative tool for HRV analysis. Existing descriptors of Poincaré plot are discussed and links with statistical HRV measures are shown. These indicate that, despite the ability to represent nonlinear dynamics, existing measures of Poincaré plot are unable to quantify this information effectively. Hence, the vast potential of Poincaré plot in HRV analysis is still unexplored. In the following chapters, we will discuss improvements of existing measures and development of novel measures to better quantification of dynamical information of HRV signal using Poincaré plot.

Chapter 3
Poincaré Plot Interpretation of HRV Using Physiological Model

Abstract In this chapter, we present new results in developing a novel mathematical model that describes the interactions between the sympathetic and the parasympathetic nervous systems and heart rate fluctuations over a short-term period of 5–10 min. While our model is based upon well-accepted physiological principles, the mathematical formulation permits in-depth numerical and analytical investigations yielding valuable insight into clinical RR interval analysis techniques.

3.1 Introduction

In this chapter, we present new results in developing a novel mathematical model that describes the interactions between the sympathetic and the parasympathetic nervous systems and heart rate fluctuations over a short-term period of 5–10 min. While our model is based upon well-accepted physiological principles, the mathematical formulation permits in-depth numerical and analytical investigations yielding valuable insight into clinical RR interval analysis techniques.

Standard analysis techniques commonly estimate the levels of sympathetic and parasympathetic activity from the variability in the RR intervals. Our attention has focused on two specific HRV analysis techniques. The first is the frequency-domain spectral analysis of RR intervals [14, 101, 119–121]. RR interval Poincaré plot analysis is the second technique [59, 87, 89, 91, 94]. The main objective of our model is to provide insight into the significance of Poincaré plot morphology, not to accurately reproduce the complex autonomic activity of any particular individual.

Our model emulates the differing varieties of Poincaré plot patterns seen in subjects over a range of sympathovagal balances. In addition, the model provides a unique link between spectral analysis techniques and the emerging analysis techniques that rely on the shape and/or other morphological properties of the Poincaré plot. Analytical results on the "lengths" and "widths" of the Poincaré plots

A.H. Khandoker et al., *Poincaré Plot Methods for Heart Rate Variability Analysis*,
DOI 10.1007/978-1-4614-7375-6_3,

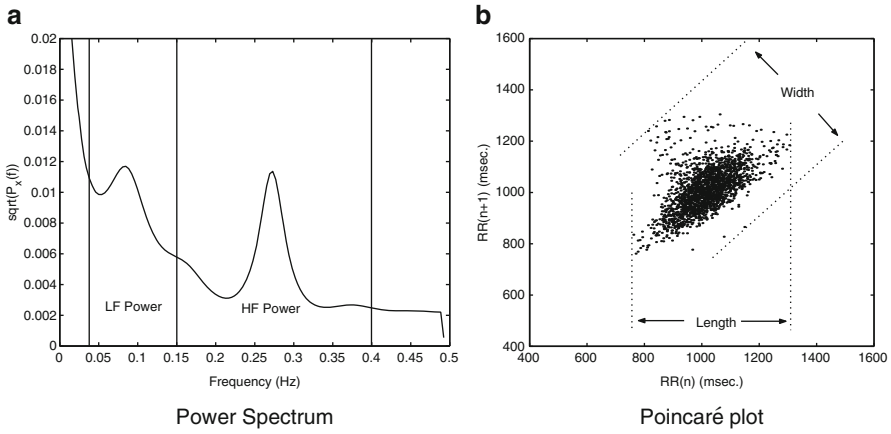

Fig. 3.1 Plot (**a**) is the HRV spectrum. The respiratory component near 0.3 Hz and the vasomotor component near 0.1 Hz are clearly present. Plot (**b**) is the Poincaré plot of the same data. The length and the width are shown graphically on the plot. Figure adapted from Brennan et al. [118]

generated by our model are developed. Simulations are employed to confirm the analytical results on the model. In order to evaluate the validity and scope of the model and analysis we provide results using a set of data from actual subjects.

3.2 Autonomous Nervous System and HRV Analysis

It is well known that perturbations to autonomic activity, such as respiratory sinus arrhythmia and vasomotor oscillations, cause corresponding fluctuations in heart rate [8, 102]. HRV analysis seeks to determine the autonomic activity from heart rate variability. Spectral analysis is the standard technique used to determine the presence of respiratory sinus arrhythmia and vasomotor oscillations [8, 122]. This is accomplished by dividing the spectrum into low-(0.04–0.15 Hz) and high-(0.15–0.4 Hz) frequency bands, known as the LF and HF bands, effectively distinguishing between rapid respiratory modulator activity and slow vasomotor modulation of heart rate (see Fig. 3.1a). HF power is supposedly a pure measure of parasympathetic activity, and LF power is reflective of sympathetic modulation and parasympathetic tone, although it is sometimes considered to reflect sympathetic tone [120]. In this chapter, spectral estimates are given by the autoregressive (AR) parametric technique using the modified covariance method [123] for the smooth spectrum and easy identification of the spectral peaks.

The Poincaré plot is a scatter plot of the current RR interval plotted against the preceding RR interval. Poincaré plot analysis is a quantitative visual technique, whereby the shape of the plot is categorized into functional classes [59, 91]. The plot provides summary information as well as detailed beat-to-beat information on

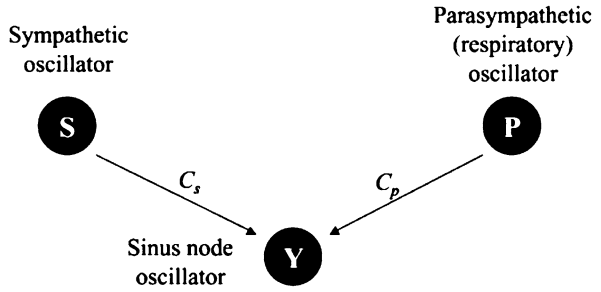

Fig. 3.2 Three coupled oscillators representing the cardiac control system. Figure adapted from Brennan et al. [118]

the behaviour of the heart [94]. Points above the line of identity indicate RR intervals that are longer than the preceding RR interval, and points below the line of identity indicate a shorter RR interval than the previous. Accordingly, the dispersion of points perpendicular to the line of identity (the "width") reflects the level of short-term variability. This dispersion can be quantified by the standard deviation of the distances the points lie from the line of identity. This measure is equivalent to the standard deviation of the successive differences of the RR intervals (SDSD or RMSSD) [89]. The standard deviation of points along the line of identity (the "length") reflects the standard deviation of the RR intervals (SDNN). Figure 3.1b details these quantitative measures of Poincaré plot shape. Poincaré plots appear under different names in the literature: scatter plots, first return maps and Lorenz plots being prominent terms. A distinct advantage of Poincaré plots is their ability to identify beat-to-beat cycles and patterns in data that are difficult to identify with spectral analysis [59, 91].

3.3 Physiological HRV Model

In this section we develop a model using a coupled network of oscillators, each representing a specific characteristic or facet of the baroreflex and autonomic nervous system. The architecture of the network and the coupling are shown in Fig. 3.2. The coupling constants C_s and C_p denote the level at which the corresponding oscillator modulates the sinus node oscillator. For the purpose of clarity, we define the respiratory oscillator as the parasympathetic oscillator.

3.3.1 Sympathetic Oscillator

The sympathetic oscillator (S) is governed by Eq. 3.1:

$$s = \sin(\omega_s t) \tag{3.1}$$

where s represents the level of sympathetic activation. Sympathetic activity occurs on a slow time scale, i.e. it reacts slowly, altering heart rate over a long duration [8, 101, 124]. Accordingly it is assigned a small value, producing slow waves of approximately 10–15 s duration. This oscillator represents the combined low-frequency (LF) power of the HRV spectrum, which includes vasomotor activity. It is generally accepted that low levels of sympathetic activity will result in slow oscillations of sympathetic nerve activity entrained to the vasomotor oscillations.

As the level of sympathetic activity increases, these oscillations are damped and the fluctuations disappear such that under intense sympathetic drive the heart rate becomes metronomic in its regularity. This damped effect can be achieved by taking $\omega_s \to 0$ or by reducing the coupling between the sympathetic oscillator and the sinus oscillator by taking $C_s \to 0$.

3.3.2 Parasympathetic Respiratory Oscillator

Respiratory oscillations affect both the sympathetic and parasympathetic nervous systems. However, because of the slow response time of the sympathetic system, these rapid oscillations, often in the order of 2–3 seconds per cycle, are mediated purely by the parasympathetic system [8, 101, 124]. The effects of respiration are described by the parasympathetic respiratory oscillator (P), which is governed by Eq. 3.2:

$$p = \sin(\omega_p t) \tag{3.2}$$

where p represents the level of parasympathetic respiratory activation. As the parasympathetic system typically reacts faster than the sympathetic system, but altering heart rate over a much shorter duration, this oscillator has a value of ω_p larger than ω_s . Values in the simulation produce oscillations of duration between 2 and 5 s. This oscillator is intended to represent short-term activity impinging on the sinus node via the parasympathetic nervous system.

3.3.3 Sinus Oscillator

The sinus node oscillator is based on the formulation of the well-known integral pulse frequency modulation (IPFM) model. Hyndman and Mohn first suggested the IPFM model as a representation of the cardiac pacemaker and the suitability for modeling the sinus node has been discussed by a number of researchers in the area of point event processes [97, 99, 102]. The IPFM model is a useful description of how cardiac events are modulated by autonomic nervous activity and has had numerous applications in describing the generation of point event processes [99, 102]. The IPFM model generates heartbeats by integrating an input

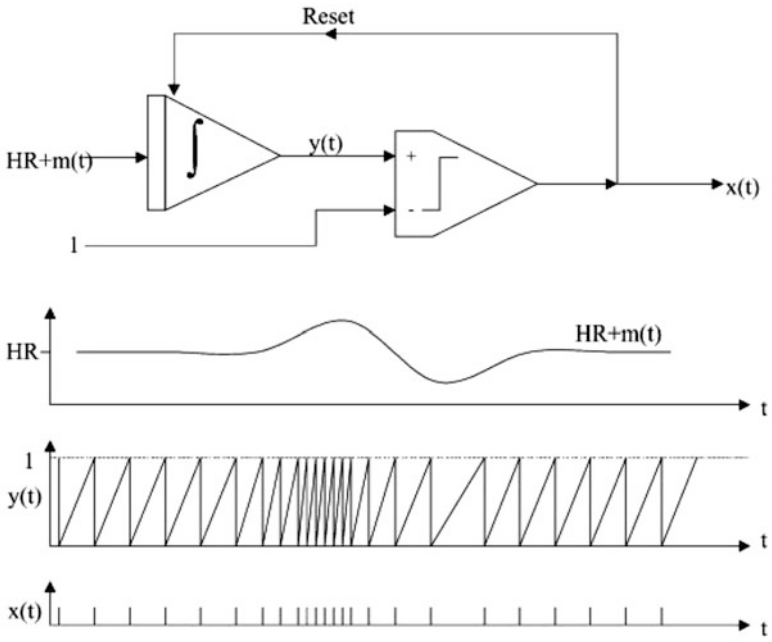

Fig. 3.3 IPFM model. The input signal $HR + m(t)$ is integrated until the integrator output $y(t)$ reaches the threshold of unity. At this point a pulse is produced in the output signal $x(t)$ and the integrator is reset. Figure adapted from Brennan et al. [118]

signal until it reaches a preset threshold of unity. At this point a pulse is produced and the integrator is reset to zero. See Fig. 3.3. The mathematical representation is given in Eq. 3.3:

$$\begin{aligned} 1 &= \int_{t_k}^{t_{k+1}} (HR + m(t))\mathrm{d}t \\ x(t) &= \sum_{k=1}^{N} \delta(t - t_k) \end{aligned} \tag{3.3}$$

The signal $m(t)$ is the input signal representing autonomic activity and t_k is the time of the k^{th} R wave. When the input signal is zero the IPFM model generates heartbeats with an interval equal to $\overline{I} = 1/HR$ where HR is a variable parameter which represents mean heart rate. It is equal to the actual frequency of heartbeats in the absence of any modulatory autonomic nervous activity. The input signal $m(t)$ represents the effects of modulatory autonomic nervous input and is defined by Eq. 3.4. If the input signal is positive then heartbeats are generated at a faster rate while a negative input signal causes heartbeats to be generated at a slower rate. The function $x(t)$ represents the series of pulses representing the heartbeats generated by the model while $y(t)$ designates the integrator's output as a function of time.

We have formulated the modulation of the sinus oscillator by the sympathetic and parasympathetic oscillators as described by Eq. 3.4:

$$m(t) = C_s s(t) + C_p p(t) \tag{3.4}$$

As a result, the sinus oscillator beats at a base rate of HR Hertz, which is increased or decreased in an additive linear fashion by sympathetic and parasympathetic respiratory modulation. For the modulating frequencies to appear unaliased in the beat sequence, the mean beat frequency HR should be higher than the highest modulating frequency component, ω_p :

$$HR \gg \frac{\omega_p}{2\pi} > \frac{\omega_s}{2\pi} \tag{3.5}$$

The coupling constants C_s and C_p reflect the levels of sympathetic and parasympathetic *modulation* of the sinus node, which is not equivalent to the tonic (mean) levels of sympathetic and parasympathetic activity. The tonic autonomic influences are included in the parameter HR which is a combined function of sympathetic and parasympathetic activity, hormonal responses and various parameters of the individual such as blood pressure. Accordingly HR is a function of the intrinsic heart rate HR_0 and the tonic influences of the autonomic system commonly referred to as the sympathovagal balance [125]. While the exact nature of sympathovagal balance is not completely understood, this concept has been formalized by the following model, $HR = HR_0 \times m \times n$, due to Rosenblueth and Simeone [124] and Katona et al. [126] in which $m > 1$ is the net sympathetic influence and $n < 1$ is the net parasympathetic influence. It is still being debated if there exist any reliable connections between the tonic influences m and n and the levels of modulation C_s and C_p; however, it is often observed that heart rate and HRV are inversely related.

Accordingly, we model HR as a free variable which is not determined explicitly by C_s or C_p. In other words, our model characterizes nervous activity as separate *modulatory* and *static* effects. C_s and C_p should be chosen such that $HR + m(t)$ is strictly positive. Choosing $C_s + C_p < HR$ guarantees this.

3.4 Mathematical Analysis of HRV Model Using Poincaré Plot

This section develops a mathematical analysis used to investigate the length and width of the Poincaré plots generated from the HRV model developed in the previous sections. As the model is a simplification of actual HRV mechanisms these results will not apply to real HRV data in an exact sense. However, the results provide clear insight into the manner in which Poincaré plot descriptors vary as sympathetic and parasympathetic modulation levels are varied. Specifically, we characterize the theoretical dependency between low- and high-frequency modulators and the shape of an RR interval Poincaré plot generated by our model.

In accomplishing this analysis we require an explicit solution to the RR interval series. The remainder of this section derives this result. By defining the time of the initial beat to be the origin $t_0 = 0$, the defining equation for the IPFM oscillator (Eq. 3.3) can be expressed non-recursively as

$$\int_0^{t_k} [HR + m(t)]\mathrm{d}t = k \tag{3.6}$$

where $m(t)$ is the modulating signal. In our model $m(t)$ consists of two frequency components. It turns out to be just as easy to work with N frequency components, so we consider $m(t) = \sum_{n=1}^{N} C_n \cos(\omega_n t + \phi_n)$ with $\omega_n \ll 2\pi HR$ for all n, i.e. slow modulation. The defining equation becomes

$$\int_0^{t_k} [1 + \bar{I} \sum_{n=1}^{N} C_n \cos(\omega_n t + \phi_n)]\mathrm{d}t = k\bar{I} \tag{3.7}$$

We have also divided through by HR and expressed $\bar{I} = 1/HR$ to make the equations simpler. After integrating, the general relationship

$$t_k + \bar{I} \sum_{n=1}^{N} \frac{C_n}{\omega_n} (\sin(\omega_n t_k + \phi_n) - \sin(\phi_n)) = k\bar{I} \tag{3.8}$$

is obtained. Performing the substitution $t_k = k\bar{I} + \delta_k$, as per De Boer et al. [99], the following nonlinear relationship for δ_k is obtained:

$$\delta_k = -\bar{I} \sum_{n=1}^{N} \frac{C_n}{\omega_n} (\sin(\omega_n k\bar{I} + \phi_n + \omega_n \delta_k) - \sin(\phi_n)) \tag{3.9}$$

The δ_k terms represent the amount each beat deviates from the regular pulse train $t_k = k\bar{I}$. Equation 3.9 can be linearized about $\delta_k = 0$ provided $\omega_n \delta_k$ is small for all $n\varepsilon[1..N]$. If the event times are close to a regular pulse train ($\delta_k < \bar{I}/2\pi$) and the modulation frequencies are less than the mean beat frequency ($\omega_n < 2\pi HR$) it is obvious that $\omega_n \delta_k \ll 1$. Hence for a large class of practical pulse trains, including RR intervals, a linear analysis is an accurate approximation. Linearizing about $\delta_k = 0$ we obtain

$$\delta_k \approx -\bar{I} \sum_{n=1}^{N} \frac{C_n}{\omega_n} (\sin(\omega_n k\bar{I} + \phi_n) - \sin(\phi_n) + \omega_n \delta_k \cos(\omega_n k\bar{I} + \phi_n)) \tag{3.10}$$

Solving for δ_k gives the final expression for the beat times:

$$t_k = k\bar{I} + \delta_k = k\bar{I} + \frac{\sum_{n=1}^{N} \frac{C_n}{\omega_n} (\sin(\omega_n k\bar{I} + \phi_n) - \sin(\phi_n))}{1 - \bar{I} \sum_{n=1}^{N} C_n \cos(\omega_n k\bar{I} + \phi_n)} \tag{3.11}$$

The RR intervals are $RR_k = t_{k+1} - t_k$. For our model, $N = 2$ and $C_1 = C_s$, $C_2 = C_p$, $\omega_1 = \omega_s$, $\omega_2 = \omega_p$ and $\phi_1 = \phi_2 = 0$. In this case, Eq. 3.11 provides us with an accurate approximation to the RR interval series generated by our HRV model. This result holds so long as the intervals are approximately regular and the modulation is slow. This is generally the case for RR intervals. However, for subjects with very large HRV the assumption that the intervals are approximately regular may be somewhat inaccurate. For the assumption $\delta_k < \bar{I}/2\pi$ to be compromised, an RR interval would have to deviate from the mean RR interval by an amount $\bar{I}$ greater than $\bar{I}/\pi \approx 0.32\pi$.

3.4.1 Length of Poincaré Plot Main Cloud

In this section we develop an approximation to the length of a Poincaré plot, depicted in Fig. 3.1b, as a function of the HRV model's coupling constants C_s and C_p. Researchers, who are dealing with noisy data, often employ the standard deviation of the RR intervals (SDNN) as a measure of Poincaré length [89, 111]. For the purposes of this section, in which sequences lacking random variability are analysed, it's simpler to define the length to be the distance between the extreme right- and left-most points of the Poincaré plot. The agreement between these two measures is a simple scaling by a constant. Thus, length is defined as the difference between the largest and smallest RR intervals: $L = \max_k RR_k - \min_k RR_k$.

Analytically deriving the maximum and minimum of the RR interval series from Eq. 3.11 is n't straightforward; fortunately, these quantities can be approximated. By employing the standard approximation $(1+z)^{-1} = 1 - z$ for $z << 1$, Eq. 3.11 can be approximated as

$$\delta_k \approx \left[-\bar{I} \sum_{n=1}^{N} \frac{C_n}{\omega_n} \left(\sin(\omega_n k \bar{I} + \varphi_n) - \sin(\varphi_n) \right) \right] \left[1 - \bar{I} \sum_{n=1}^{N} C_n \cos(\omega_n k \bar{I} + \varphi_n) \right] \tag{3.12}$$

Expanding the brackets, combining sums and using standard trigonometric identities it is possible to express Eq. 3.12 as a sum of sinusoids

$$\begin{aligned} \delta_k = & -\bar{I} \sum_{n=1}^{N} \frac{C_n}{\omega_n} \left[\sin\left(\omega_n k \bar{I} + \varphi_n + \bar{I} \sum_{m=1}^{N} C_m \sin(\varphi_m) \right) - \sin(\varphi_n) \right] \\ & + \bar{I}^2 \sum_{n=1}^{N} \sum_{m=1}^{N} \frac{C_n C_m}{2\omega_n} \left[\sin((\omega_n - \omega_m) k \bar{I} + \varphi_n - \varphi_m) + \sin((\omega_n + \omega_m) k \bar{I} + \varphi_n + \varphi_m) \right] \end{aligned} \tag{3.13}$$

Hence, the RR interval series, $RR_k = \bar{I} + \delta_k - \delta_{k-1}$, is

$$RR_k = \bar{I} - 2\bar{I}\sum_{n=1}^{N}\frac{C_n}{\omega_n}\sin\left(\frac{\omega_n\bar{I}}{2}\right)\cos\left(\omega_n k\bar{I} + \varphi_n + \bar{I}\sum_{m=1}^{N} C_m\sin(\varphi_m) - \frac{\omega_n\bar{I}}{2}\right)$$
$$+\bar{I}^2\sum_{n=1}^{N}\sum_{m=1}^{N}\frac{C_nC_m}{\omega_n}\left[\begin{array}{l}\sin\left(\frac{(\omega_n-\omega_m)\bar{I}}{2}\right)\cos\left((\omega_n-\omega_m)k\bar{I}+(\varphi_n-\varphi_m)-\frac{(\omega_n-\omega_m)\bar{I}}{2}\right)\\ +\sin\left(\frac{(\omega_n+\omega_m)\bar{I}}{2}\right)\cos\left((\omega_n+\omega_m)k\bar{I}+(\varphi_n+\varphi_m)-\frac{(\omega_n+\omega_m)\bar{I}}{2}\right)\end{array}\right] \tag{3.14}$$

Assuming the maximum values of the time-varying sinusoids (those dependent upon k) of Eq. 3.14 are eventually sampled *simultaneously* at some point in time, an approximation to the upper limit of the length is obtained by replacing the sinusoids with the value 1. This approach gives the maximum length obtainable, a figure that is strictly an upper bound yet also serves as an approximation to the true length L for modulation frequencies significantly less than the mean beat frequency. This is by virtue of having sampled frequently enough to examine arbitrarily close to the upper bound at some point in time. The upper bound on L is then twice the sum of the amplitudes of the frequency components described in Eq. 3.14. As $C_n << 1$, L is largely determined by the first-order terms. Equation 3.15 is the first-order approximation to length. It is noted that this quantity is no longer the strict upper bound on L due to discarding of the higher-order contributions; however, it remains an approximation to the true length:

$$L \approx 4\bar{I}\sum_{n=1}^{N}\frac{C_n}{\omega_n}\left|\sin\left(\frac{\omega_n\bar{I}}{2}\right)\right| \tag{3.15}$$

Therefore, Poincaré plots obtained from our HRV model have a length approximated by

$$L \approx \frac{4}{HR}\left[\frac{C_s}{\omega_s}\left|\sin\left(\frac{\omega_s}{2HR}\right)\right| + \frac{C_p}{\omega_p}\left|\sin\left(\frac{\omega_p}{2HR}\right)\right|\right] \tag{3.16}$$

The actual (true) Poincaré plot length as a function of the HRV model's coupling constants C_s and C_p over the range 0.0–0.15 is shown in Fig. 3.4a (obtained via simulations). Length appears to be dependent upon C_s and C_p in an almost identical manner and to behave linearly, in agreement with this analysis. Figure 3.4c compares true length to the approximation to length given by Eq. 3.16. For $C_s + C_p << 1$ the approximation is in excellent agreement with the true length. As $C_s + C_p$increases, second-order influences begin to become significant due to nonlinear effects becoming prominent, as expected from the analysis. The approximately identical manner that the coupling constants control the length can be explained by noting that $\sin(x) \approx x$ when $x \ll 1$ and for low modulation frequencies $\omega_p \ll 2\pi HR$. Accordingly, Eq. 3.16 behaves as

$$L \approx \frac{2}{HR^2}(C_s + C_p) \tag{3.17}$$

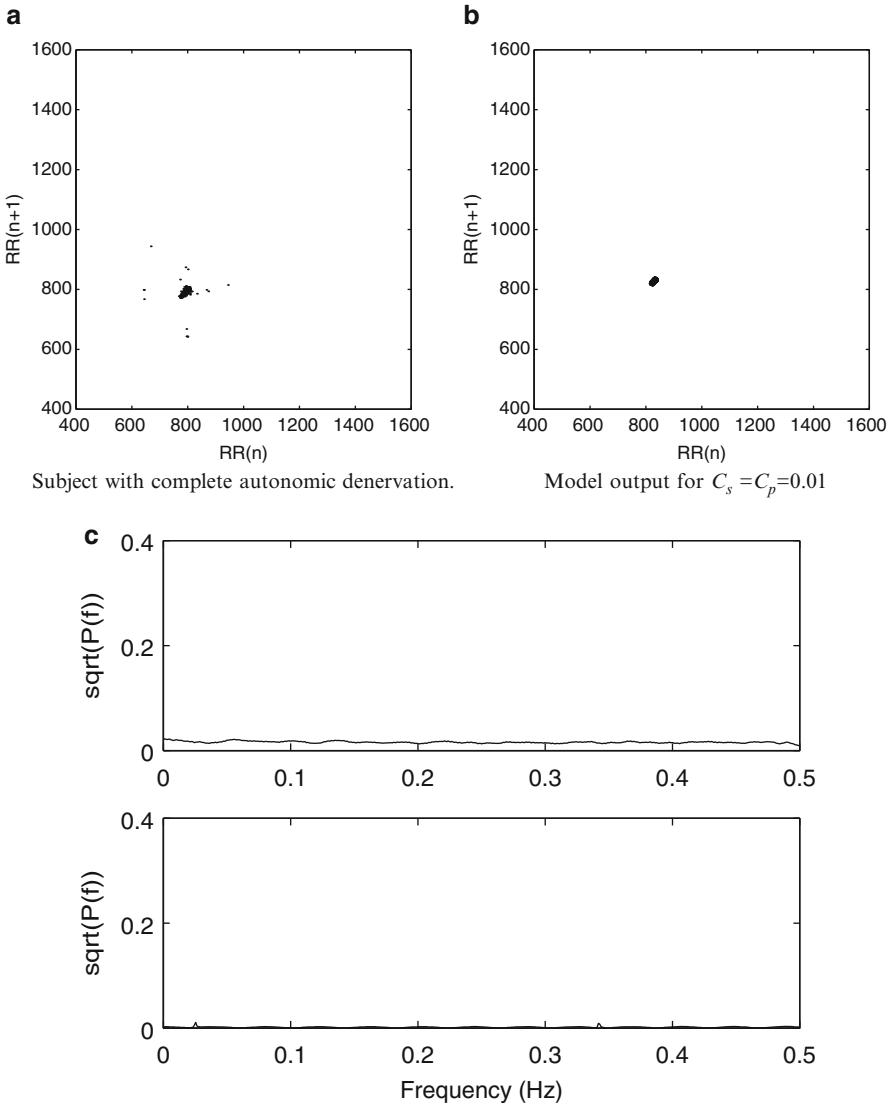

Fig. 3.4 Complete autonomic blockade. (**a**) Poincaré plot of subject with complete autonomic denervation (transplant patient) with mean RR interval of 800 ms. (**b**) Sinus oscillator with low coupling to sympathetic and parasympathetic oscillators. (**c**) Power spectra of plots (**a**) and (**b**). Figure adapted from Brennan et al. [118]

These results state that high- and low-frequency modulations affect L in equivalent manners for slow modulation and in a linear fashion for small coupling intensities. Under these conditions, length reflects neither the high- nor the low-frequency

modulations more significantly than the other. Thus, for practical purposes, length may be considered a measure of total modulation and is akin to the total power of the modulating signal.

3.4.2 Width of the Poincaré Plot Main Cloud

The width of the main cloud of an RR interval Poincaré plot characterizes the dispersion of points about the line of identity. Common measures of the width are the standard deviation and the root mean square of the successive differences of the RR intervals (SDSD or RMSSD) [89, 111]. As for the length of the model-based Poincaré plot, the lack of any random component is exploited and the width is defined to be the distance between the extremities as depicted in Fig. 3.1b. Thus, the width is $W = \max_k |\Delta RR_k| \Big/ \sqrt{2}$ as Fig. 3.5 details. This expression involves the "delta" RR intervals, $\Delta RR_k = RR_k - RR_{k-1}$, which are also known as the successive differences of the RR intervals. They are given by

$$\begin{aligned}\Delta RR_k = &-4\bar{I}\sum_{n=1}^{N}\frac{C_n}{\omega_n}\sin^2\left(\frac{\omega_n\bar{I}}{2}\right)\sin\left(\omega_n k\bar{I}+\varphi_n+\bar{I}\sum_{m=1}^{N}C_m\sin(\varphi_m)-\omega_n\bar{I}\right)\\ &+2\bar{I}^2\sum_{n=1}^{N}\sum_{m=1}^{N}\frac{C_nC_m}{\omega_n}\left[\begin{array}{l}\sin^2\left(\frac{(\omega_n-\omega_m)\bar{I}}{2}\right)\sin\left((\omega_n-\omega_m)k\bar{I}+(\varphi_n-\varphi_m)-(\omega_n-\omega_m)\bar{I}\right)\\ +\sin^2\left(\frac{(\omega_n+\omega_m)\bar{I}}{2}\right)\sin\left((\omega_n+\omega_m)k\bar{I}+(\varphi_n+\varphi_m)-(\omega_n+\omega_m)\bar{I}\right)\end{array}\right]\end{aligned} \tag{3.18}$$

As can be seen from Eq. 3.18, the delta RR intervals posses no D.C. component, which is expected due to the zero average. Similar frequency content is present as for the length, except for being phase shifted and being multiplied by an extra $\sin(\cdot)$ term leading to the squared coefficient. An approximation to W is determined by taking an upper bound for W (by replacing the time-varying sinusoids with unity) and retaining only first-order terms as detailed in the calculations for length:

$$W \approx 4\sqrt{2}\bar{I}\sum_{n=1}^{N}\frac{C_n}{\omega_n}\sin^2\left(\frac{\omega_n\bar{I}}{2}\right) \tag{3.19}$$

For our HRV model, this expression is

$$W \approx \frac{4\sqrt{2}}{HR}\left[\frac{C_s}{\omega_s}\sin^2\left(\frac{\omega_s}{2HR}\right)+\frac{C_p}{\omega_p}\sin^2\left(\frac{\omega_p}{2HR}\right)\right] \tag{3.20}$$

Figure 3.4b details how true width varies as the coupling parameters are varied over the range 0.0–0.15. A comparison of Eq. 3.20 to the true width is given in Fig. 3.4d. It is seen that the approximation to W is accurate when $C_s + C_p << 1$ but deviates widely as $C_s + C_p$ becomes large, due mainly to second-order influences becoming prominent. It can be seen from Fig. 3.4b that the level of high-frequency

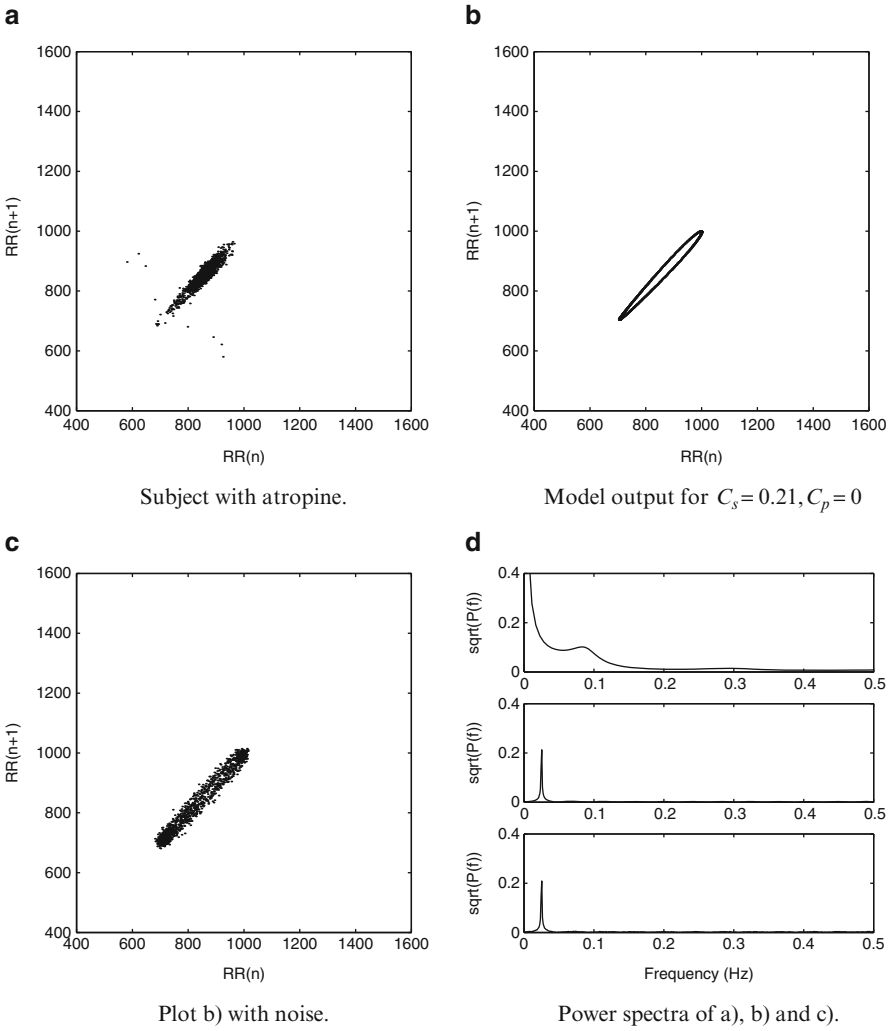

Fig. 3.5 Plot (**a**) is a Poincaré plot of a subject that has been given atropine to block parasympathetic activity. Plot (**b**) shows model generated RR intervals when the sympathetic oscillator is coupled. In plot (**c**) additive Gaussian noise with a standard deviation of 10 ms. is included. Plot (**d**) is the power spectra of plots (**a**) (*upper*), (**b**) (*middle*) and (**c**). Figure adapted from Brennan et al. [118]

modulation C_p is the dominant parameter controlling width. This property is clearly seen from the analysis, especially for small modulation frequencies ($\omega_s < 2\pi HR$) as Eq. 3.20 behaves approximately as

$$W \approx \frac{1}{\sqrt{2}HR^3}\left[C_s\omega_s + C_p\omega_p\right] \tag{3.21}$$

Roughly speaking, the width of a Poincaré plot is a function of the *weighted* sum of the low- and high-frequency amplitudes, where each amplitude is weighted by the respective angular frequency. Accordingly, higher-frequency components contribute to the width in larger amounts, and lower-frequency components contribute at minor yet still significant levels. As will be explained later, Poincaré plot width should correlate highly with high-frequency power (HF) and correlate at small levels with low-frequency power (LF).

3.4.3 Poincaré Plot Morphological Properties for the HRV Model

As the previous sections have shown, the correspondence between the HRV model's parameters and the Poincaré plot's shape can be accurately approximated by a linear transformation for small coupling intensities:

$$\begin{bmatrix} L \\ W \end{bmatrix} = \begin{bmatrix} \frac{4}{HR\omega_s}\sin\left(\frac{\omega_s}{2HR}\right) & \frac{4}{HR\omega_p}\sin\left(\frac{\omega_p}{2HR}\right) \\ \frac{4\sqrt{2}}{HR\omega_s}\sin^2\left(\frac{\omega_s}{2HR}\right) & \frac{4\sqrt{2}}{HR\omega_p}\sin^2\left(\frac{\omega_p}{2HR}\right) \end{bmatrix} \begin{bmatrix} C_s \\ C_p \end{bmatrix} \tag{3.22}$$

The significance of this result is that the morphology of a Poincaré plot encodes the amplitudes of the modulation signal, allowing recovery of the amplitudes for signals composed of two known frequency components:

$$\begin{bmatrix} C_s \\ C_p \end{bmatrix} = \frac{1}{\gamma} \begin{bmatrix} \frac{\sin\left(\omega_p/2HR\right)\omega_s HR}{4\sin(\omega_s/2HR)} & \frac{-\sqrt{2}\omega_s HR}{8\sin(\omega_s/2HR)} \\ \frac{-\sin(\omega_s/2HR)\omega_p HR}{4\sin\left(\omega_p/2HR\right)} & \frac{\sqrt{2}\omega_p HR}{8\sin\left(\omega_p/2HR\right)} \end{bmatrix} \begin{bmatrix} L \\ W \end{bmatrix} \tag{3.23}$$

$$\gamma = \sin\left(\omega_p/2HR\right) - \sin\left(\omega_s/2HR\right)$$

For our model, it is theoretically possible to estimate similar characteristics to HRV spectral analysis, such as LF power, HF power and HF/LF ratios, from the shape of the Poincaré plot by assigning appropriate values to the constants ω_s and ω_p. This is in addition to investigating the detailed beat-to-beat characteristics of HRV data. It should be noted that this property only applies exactly for modulation signals composed of only two frequency components. Perhaps three-dimensional Poincaré plots can resolve three frequency components, and so on. How well the correspondence generalizes to actual HRV data is dependent on how well the HRV spectrum is approximated by two dominant peaks.

3.5 Simulation Results in Clinical Examples

In this section, we demonstrate that our model displays the features of real RR intervals under various induced autonomic balances. We consider the following conditions: complete autonomic blockade, parasympathetic blockade and normal sympathetic-parasympathetic balance. Poincaré plots of the model's output are compared to plots of actual RR intervals obtained from patients under the prescribed autonomic perturbations. The model's simulated autonomic balance is adjusted by varying the coupling constants, which alters the levels at which the oscillators influence the sinus oscillator. For all simulations, except where otherwise mentioned, the following constants were used:

$$HR = 1.18\,\text{Hz}, \omega_\text{S} = 2\pi \times 0.025\,\text{Rad/s}, \text{ and } \omega_\text{P} = 2\pi \times 0.344\,\text{Rad/s} \tag{3.24}$$

HR corresponds to an RR interval of 850 ms. The period of the sympathetic oscillator is set to approximately 40 s and the parasympathetic oscillator is set to a period of approximately 3 s.

3.5.1 Complete Autonomic Blockade

First, we consider the model's output in the absence of coupling, a state that is easily simulated with $C_s$and C_p taking on very small values. Consider Fig. 3.6b for which the coupling constants were $C_s = C_p = 0.01$. The Poincaré plot appears as a single dense point termed a "tight cluster". Due to the low coupling, there is very little variation in $m(t)$ and subsequently the sinus oscillator beats at a constant frequency of HR Hertz. Accordingly the RR intervals varied little from the constant value $1/HR$ seconds. The behaviour of a de-nerved heart, such as found in the case of a transplant patient as in Fig. 3.6a, is mimicked. Figure 3.6c shows the power spectra of plots (a) and (b). It is seen that neither the transplant patient nor the model has any significant spectral power in either the LF or HF bands.

3.5.2 Unopposed Sympathetic Activity–Parasympathetic Blockade

This scenario is simulated by a high degree of coupling between the sympathetic oscillator and the sinus oscillator while a low-coupling level is used for the parasympathetic respiratory oscillator. Accordingly, the coupling constants take the values $C_s = 0.21$ and $C_p = 0$. The model's output, viewed as a Poincaré plot in

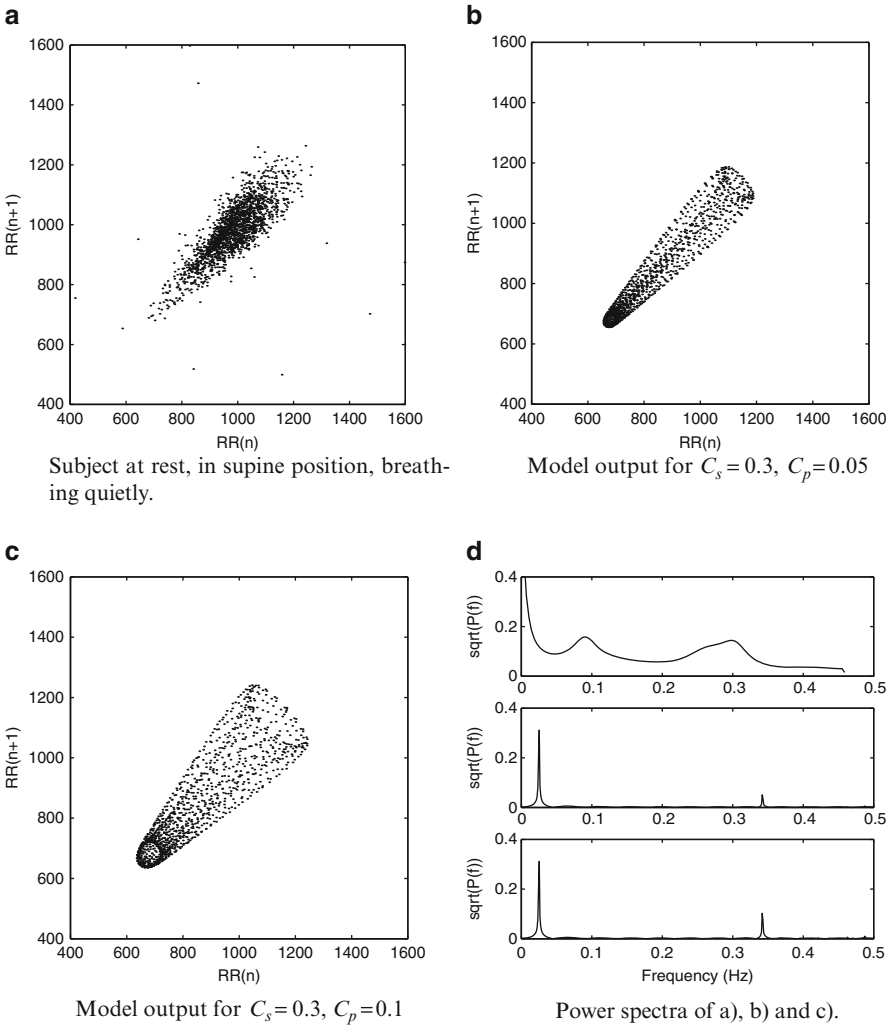

Fig. 3.6 Balanced sympathetic and parasympathetic activity. Plot (**a**) shows RR intervals obtained from a subject who is lying supine at rest. Plot (**b**) shows the model's simulated output for the coupling constants Cs = 0.3 and Cp = 0.05. Plot (**c**) shows the effect of increasing Cp to 0.1. Plot (**d**) shows the power spectra of plots (**a**), (**b**) and (**c**). Figure adapted from Brennan et al. [118]

Fig. 3.7b, is a slender closed loop oriented along the line $y = x$ and is suggestive of a "cigar" due to its shape. No variability is present other than the motion around the loop, a direct result of excluding the parasympathetic respiratory oscillator.

The plot in Fig. 3.7a is of a healthy subject who has been infused with atropine. The variability witnessed in this plot is therefore largely a product of sympathetic activity. The total lack of any short-term variability in our model's output prevents

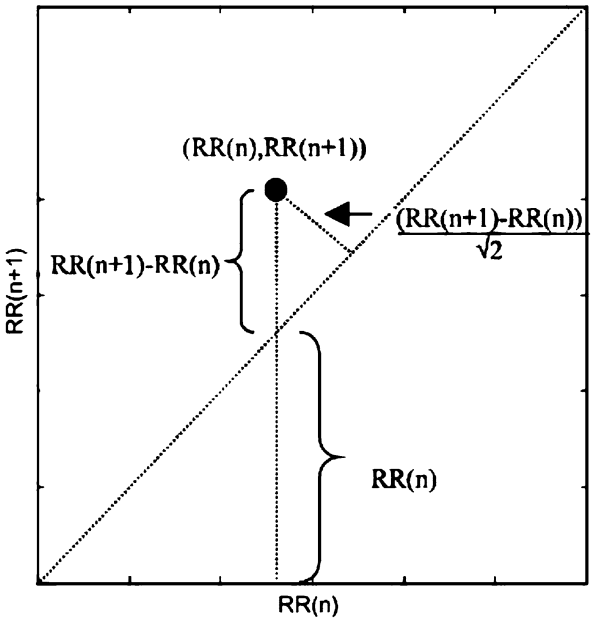

Fig. 3.7 Poincaré width, W, is measured as the largest difference between consecutive intervals, multiplied by the square root of 2. Figure adapted from Brennan et al. [118]

a clear comparison to this subject except at the most qualitative level. Figure 3.7c shows the effect of artificially adding a small amount of short-term variability to the model's output by adding zero mean Gaussian noise with a standard deviation of 10 ms. to the simulated intervals. A Poincaré plot very similar to actual observed cigar-shaped plots is observed. Real-life physiological systems usually do contain some level of spontaneous random variability that is best modelled as noise, particularly at this level. The model's output resembles RR intervals recorded from patients with degraded parasympathetic nervous control, such as patients with heart failure [89]. The length of the cigar is directly proportional to the amplitude of the sympathetic modulation of the sinus oscillator.

The power spectrum of the atropine-infused subject in Fig. 3.7a is shown in the upper panel of Fig. 3.7d. The spectrum is seen to consist of a substantial level of LF power and very little HF power. The middle panel of Fig. 3.7d shows the power spectra of the model-generated RR intervals. The single peak in the LF band is the effect of the sympathetic oscillator with a coupling intensity of 0.21. Finally, the lower panel of Fig. 3.7d shows the power spectrum of the model-generated RR intervals with added noise. The noise adds a constant level across all frequencies to the power spectrum, and therefore its presence does not overly alter the shape of the spectrum.

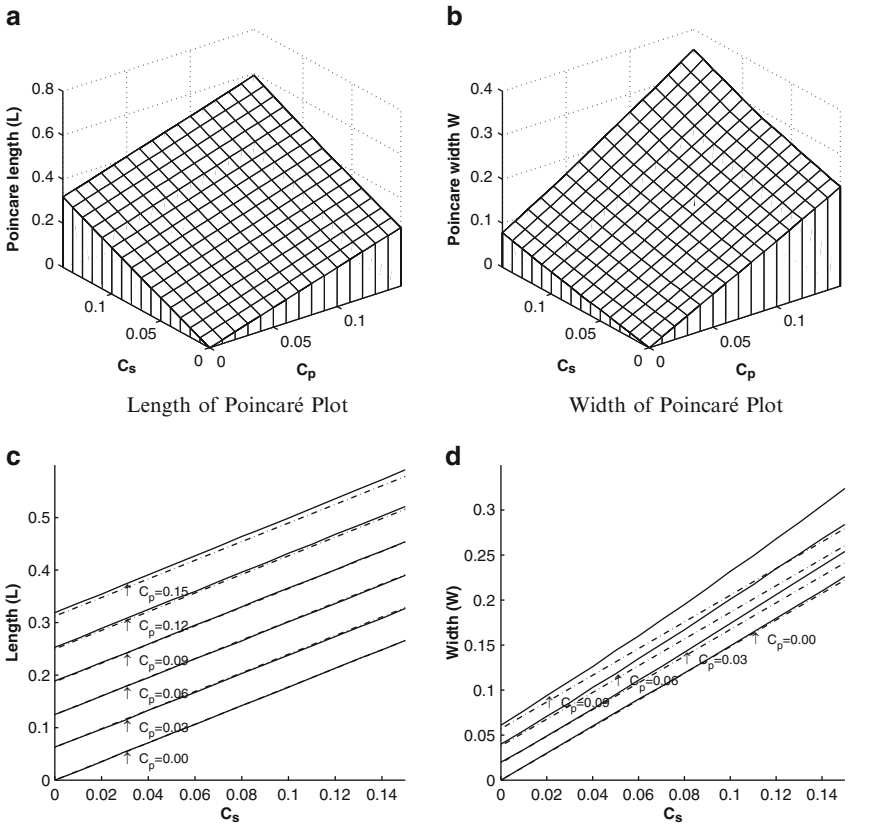

Fig. 3.8 Plots of width and length of Poincaré plot main clouds as the two coupling parameters are varied over the range 0.0 to 0.15. Subplots (**a**) and (**b**) present the length and width obtained from simulated RR intervals. Subplots (**c**) and (**d**) show how the analytic approximations to length and width compare. Figure adapted from Brennan et al. [118]

3.5.3 Sympathetic-Parasympathetic Balance

In this scenario, levels of parasympathetic respiratory activity are introduced. This is simulated by way of a small coupling intensity for the parasympathetic respiratory oscillator in addition to a high level of sympathetic coupling. Figure 3.8b shows the model's RR interval output for the coupling constants $C_s = 0.3$ and $C_p = 0.05$. A large degree of variability emerges in the model's output, in which the parasympathetic oscillator is responsible for the flanging effect or widening of the cigar shape into a "comet". Comparing Fig. 3.8a and b shows how closely the simulated RR intervals resemble a Poincaré plot of a subject at rest breathing quietly in the supine position. Increasing the parasympathetic respiratory oscillator's

coupling intensity increases the width of the comet and consequently the level of short-term variability in the RR intervals. Figure 3.8c demonstrates this effect with C_p taking on the value of 0.1. The width of the comet is also dependent on the frequency of the parasympathetic oscillator in an intuitive manner: larger values of ω_p yield wider comets because short-term variability is increased.

The power spectrum of the supine subject of Fig. 3.8a is presented in the upper panel of Fig. 3.8d. A substantial level of both LF and HF power is displayed. The middle panel of Fig. 3.8d shows the power spectrum of the model-generated RR intervals. The two peaks produced by the sympathetic and the parasympathetic oscillators with coupling intensities 0.3 and 0.05 are clearly shown. The lower panel of Fig. 3.8d displays the power spectrum of Fig. 3.8c, which has an increased value of 0.1 for the parasympathetic oscillator's coupling.

A significant difference exists between the Poincaré plots of the model-generated RR intervals and the RR intervals obtained clinically: the density of the points in the simulated cases is skewed towards the lower left corner of the plot while actual RR intervals are more centrally distributed. The core of this discrepancy lies in the highly periodic nature of the oscillators. Fluctuations produced by the actual autonomic nervous system are not pure sinusoidal signals. Instead they resemble a random walk which obtains low- and high RR interval lengths occasionally while usually fluctuating about a mean value without deviating widely. It is important to observe that the lengths and widths of Fig. 3.8a and b are roughly the same. Our model shows it is this feature that corresponds to the balance of low- and high-frequency power being similar, not the dispersion of the points within the Poincaré plot.

At this point it is interesting to consider how well the results of the previous section apply to actual data obtained from subjects under various autonomic conditions. The results are not expected to apply completely as they stem from a model of a discrete spectrum. However, the general principles identified by the analysis should be evident. That is, the length of the Poincaré plot should be approximately equivalently dependent upon low-frequency modulation and high-frequency modulation. In addition, the width is expected to be dependent upon high-frequency modulation more strongly than on low-frequency modulation. To these predictions, we apply the equations developed in the previous section to RR intervals obtained from subjects under various autonomic conditions.

3.5.4 Data Set Acquisition

We employ the data set of a previous study [94] as it contains subjects over a wide range of autonomic conditions. The data set consists of ten healthy subjects (five female, five male) aged between 20 and 40 years (mean 30.2, sd 7.2). Each subject underwent four autonomic perturbations: baseline study with subjects in

the supine position in a quite environment; seventy-degree head-up tilt which increases sympathetic activity and decreases parasympathetic activity; atropine infusion which markedly decreases parasympathetic nervous system activity and transdermal scopolamine which increases parasympathetic nervous activity. In all, 40 records were collected, each containing 1,024 RR intervals.

3.5.5 Data Set Analysis

For each data set, the length and width of the Poincaré plot and the LF and HF power were calculated. The length was calculated by $L = 2SDRR$, and the width by $W = \sqrt{2}SDSD$ as can be derived from simple geometry. The LF and HF parameters were calculated by using the AR technique with the modified covariance technique [123]. The bands were LF = 0.04–0.15 Hz and HF = 0.15–0.4 Hz. First, we derive the length and width of the Poincaré plot from the LF and HF power by using Eq. 3.22 and compare the derived length and width with the actual length and width by plotting them against each other as scatter plot. The closer the values are to being identical, the closer the scatter plot resembles the line of identity. Equation 3.22 requires the values of the constants ω_s, ω_p and HR. The value of HR is calculated as the inverse of the average RR interval. The choice of suitable values for ω_s and ω_p is akin to the choice of the LF and HF frequency bands. The mid-frequencies of the bands would seem the most appropriate choice, i.e., $\omega_s = 2\pi(0.1)$ and $\omega_p = 2\pi(0.28)$ radians/s.

Figure 3.9a displays the derived length on the vertical axis and the actual length on the horizontal axis. The points do reflect the line of identity; however, there exists a fair amount of variability which indicates that Eq. 3.22 does not hold entirely. The goodness of fit to the line of identity can be quantified by the correlation coefficient. Figure 3.9a has a correlation coefficient of 0.94 indicating that Eq. 3.22 holds reasonably well. In other words, Eq. 3.22 is explaining the main trend of the actual length very well. Equation 3.22 has a tendency to underestimate the actual length. This can be partially explained by noting that the length is a measure of all the modulation; the LF and HF measures, however, only consider the power from 0.04 Hz upwards. The derived width vs. the actual width is plotted on Fig. 3.9b. A very good fit with a correlation coefficient of 0.97 occurs. This indicates that Eq. 3.22 is very good at predicting the width of a Poincaré plot. The superior performance of the width over the length can be explained by noting that the hypothesized reason for the underestimation of length is that the very-low-frequency power has been ignored. Ignoring the very-low-frequency power will not adversely affect the width as it is dominated by high-frequency power (HF).

The same analysis is now repeated for the reverse situation. Starting with the length and width of a Poincaré plot, we derive the LF and HF power using Eq. 3.23 and assign $LF = C_S$ and $HF = C_P$. The derived values of LF and HF are then compared to the actual LF and HF values calculated by standard spectral analysis.

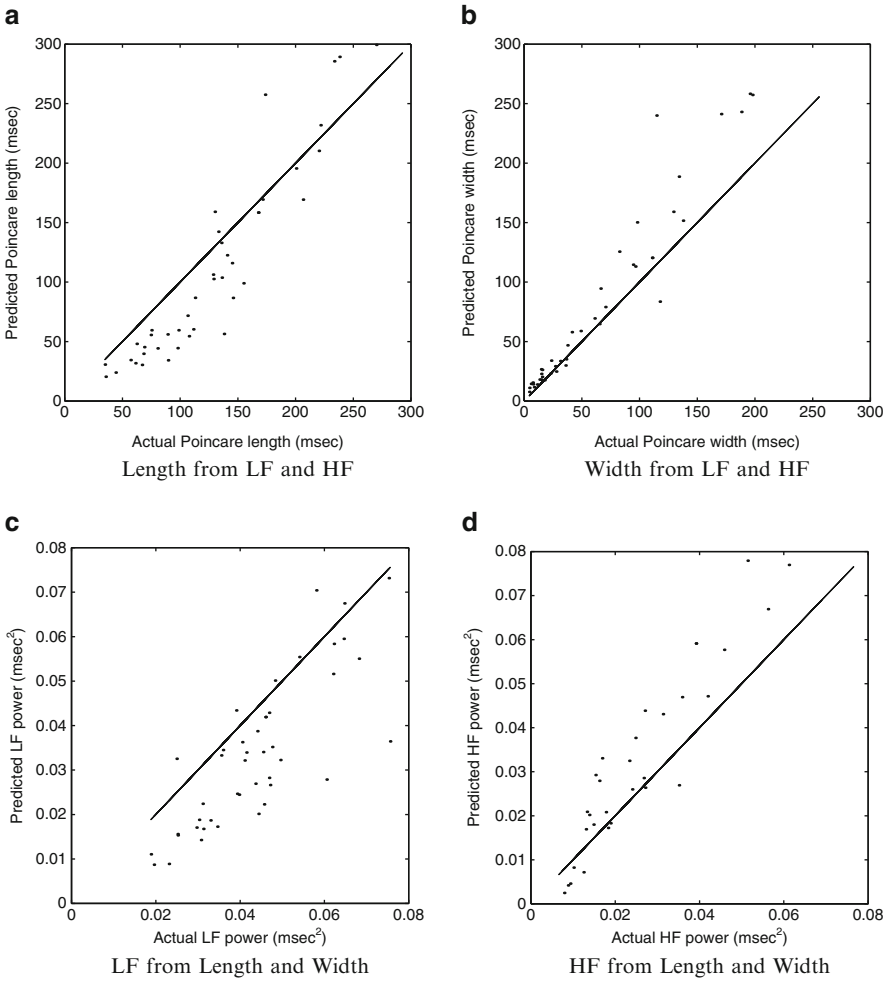

Fig. 3.9 Comparisons of derived parameters versus actual values. Correlation coefficients are: plot (**a**) 0.94, plot (**b**) 0.97, plot (**c**) 0.81 and plot (**d**) 0.94. Figure adapted from Brennan et al. [118]

Figure 3.9c displays the actual LF power vs. the derived LF power. The correlation coefficient of the plot is 0.81, which indicates a reasonable linear fit. However, it is clear that the main trend of the relationship between LF power and length and width is clearly captured by Eq. 3.23. Figure 3.9d compares derived HF power with actual HF power. A correlation coefficient of 0.93 indicates that Eq. 3.23 explains the dependency of HF on the length and width very well.

These results clearly show that the principles identified from Eq. 3.22 and Eq. 3.23 are present for actual HRV data. It must be remembered that the equations are not expected to hold perfectly as they were derived for the HRV model under

the assumption of two modulation frequencies. The fact that a discrete spectrum consisting of only two components can explain so much about the relationships between LF, HF, length and width of a Poincaré plot is remarkable.

3.5.6 Poincaré Plot Morphology for Real Data

In this section we discuss the significance of the length and width descriptors of Poincaré plots. The results of the previous sections imply that the width is a measure of short-term variability and the length is a measure of total variability. This result has consequences for the correlations between frequency-domain indices and Poincaré plot indices. Attempting to correlate LF power with Poincaré length (or equivalent SDNN measures) will explain only part of the variations in Poincaré length. Substantial portions of the variations are due to the codependency with HF power and will appear as uncorrelated noise. In data sets where significant variations in both LF and HF power are present, our model predicts that Poincaré length will correlate reasonably well with both LF and HF powers; however, it will correlate highly with neither due to the variations introduced by the other. For Poincaré width, the dependencies upon HF power are stronger than those of LF power. A strong correlation is expected when comparing HF power to Poincaré width, as the variations due to LF power will be small. LF power should correlate with Poincaré width, albeit at low levels, because LF power does influence the width, but the variations present due to HF power are large and reduce the correlation coefficient markedly.

Many of these results have already been shown experimentally. Specifically, our findings corroborate the findings of Otzenberger et al. [127], who found that SDNN (Poincaré length) correlated with both LF and HF power, and RMSSD (Poincaré width) correlated with HF power and to a lesser extent, LF power. Tullppo et al. [111], who investigated HRV and exercise, also present experimental results which agree with our findings: SDNN correlated almost equally with HF (Pearson's correlation coefficient: $r = 0.75$) and LF ($r = 0.72$) power, and RMSSD correlated highly with HF power ($r = 0.97$) and to a lesser yet significant extent with LF power ($r = 0.65$).

3.6 Conclusion

Poincaré plots are generated from the model and compared to Poincaré plots generated from subjects under various autonomic conditions. Now one can clearly understand how various autonomic regimes appear on the Poincaré plot through the use of the model. Traditionally, researchers have identified length and width of Poincaré plots with low- and high-frequency powers, respectively, of the HRV

signal. However, with the use of our model, we establish that the length and width are not separately related, but are a weighted combination of low- and high-frequency power. This investigation provides a theoretical link between frequency-domain spectral analysis techniques and time-domain Poincaré plot analysis.

To determine the degree to which our results generalize to actual HRV data we applied the model-based formulae to a set of clinical data. The results indicate that the formulae do identify clear trends in the relationships between the spectral components and Poincaré length and width. This gives definitive evidence that, for HRV data, the length is a display of total modulation and the width indicates predominately short-term modulation. In summary, this chapter provides clear mathematical insight into the nature of observed data.

Chapter 4
Poincaré Plot in Capturing Nonlinear Temporal Dynamics of HRV

Abstract The method and importance of capturing temporal variation using standard descriptors (*SD1* and *SD2*) of Poincaré plot have been presented in Chap. 2. However, this does not include the temporal variation at point-to-point level of the plot. In addition, *SD1* and *SD2* descriptors are linear statistics (Brennan et al., IEEE Trans. Biomed. Eng. **48**:1342–1347, 2001) and hence the measures do not directly quantify the nonlinear temporal variations in the time series contained in the Poincaré plot. Although *SD1*/*SD2* is considered as a nonlinear measure, it yields mixed results when applied to the data sets that form multiple clusters in a Poincaré plot due to complex dynamic behaviours (Brennan et al., IEEE Trans. Biomed. Eng. **48**:1342–1347, 2001). This is because the technique relies on the existence of a single cluster or a defined pattern (Christopher et al., Biophys. J. **82**:206–214, 2002; Schechtman et al., Pediatr. Res. **40**:571–577, 1996). Therefore, further studies are required in defining new descriptors for analysing temporal variability of time series using Poincaré plots. Another driving force behind this study is the fact that the visual pattern of the Poincaré plot of heart rate variability signals relies upon clinical scenarios and the application of the existing standard descriptors in various studies has resulted in limited success.

4.1 Introduction

The method and importance of capturing temporal variation using standard descriptors (*SD1* and *SD2*) of Poincaré plot have been presented in Chap. 2. However, this does not include the temporal variation at point-to-point level of the plot. In addition, *SD1* and *SD2* descriptors are linear statistics [112] and hence the measures do not directly quantify the nonlinear temporal variations in the time series contained in the Poincaré plot. Although *SD1*/*SD2* is considered as a nonlinear measure, it yields mixed results when applied to the data sets that form multiple clusters in a Poincaré plot due to complex dynamic behaviours [112]. This is because the technique relies on the existence of a single cluster or a defined

A.H. Khandoker et al., *Poincaré Plot Methods for Heart Rate Variability Analysis*,
DOI 10.1007/978-1-4614-7375-6_4,

pattern [128,129]. Therefore, further studies are required in defining new descriptors for analysing temporal variability of time series using Poincaré plots. Another driving force behind this study is the fact that the visual pattern of the Poincaré plot of heart rate variability signals relies upon clinical scenarios and the application of the existing standard descriptors in various studies has resulted in limited success.

The inherent assumption behind using consecutive RR points in Poincaré plot is that the "present-RR-interval" significantly influences the "following-RR-interval". Various researchers reported that varying lags of Poincaré plot give better understanding about the autonomic control of the heart rate that influence the short-term and long-term variability of the heart rate [57,91]. A system can have different short- and long-term correlations on different time scales. When the sampling interval is less than the short-time correlation length, then these short-time correlations can be predominantly seen [130]. So in the context of short- or long-term variability, any point can influence at least a few successive points. Lerma et al. [131] reported that the current RR interval can influence up to approximately eight subsequent RR intervals in the context of the short-term variability. In another study, Thakre and Smith examined the theoretical demand with different lags and showed that there is a curvilinear relationship between lag Poincaré plot indices for normal subjects, which is lost in congestive heart failure (CHF) patients [132]. The relation between *lag*s and width of Poincaré plot (*SD1*) has been reported by Goshvarpour et al. [133]. Therefore, measurement from a series of lagged Poincaré plots (multiple lag correlation) can potentially provide more information about the behaviour of the underlying system than the conventional *lag-1* plot measurements [131].

The hypothesis of this chapter is that any descriptor that captures temporal information and is a function of multiple lag correlation, would provide more insight into the system rather than conventional measurements of variability of Poincaré plot (*SD1* and *SD2*), which are parameters of a *lag-1* correlation. In order to test this hypothesis, we propose a novel descriptor, complex correlation measure (*CCM*), for Poincaré plot that can be applied to measure the temporal variation of the Poincaré plot and is a function of multiple lag correlation of the signal.

4.2 Nonlinear Dynamics

4.3 Limitation of Standard Descriptors of Poincaré Plot

SD1 and *SD2* represent the distribution of the signal in 2D space and carry only spatial (shape) information. It should be noted that many possible RR interval series result in identical plot with exactly similar *SD1* and *SD2* values irrespective of different temporal structures. For example, two signals with similar *SD1* and *SD2* values, top panels (Fig. 4.1), are different in terms of temporal structure, bottom panels (Fig. 4.1).

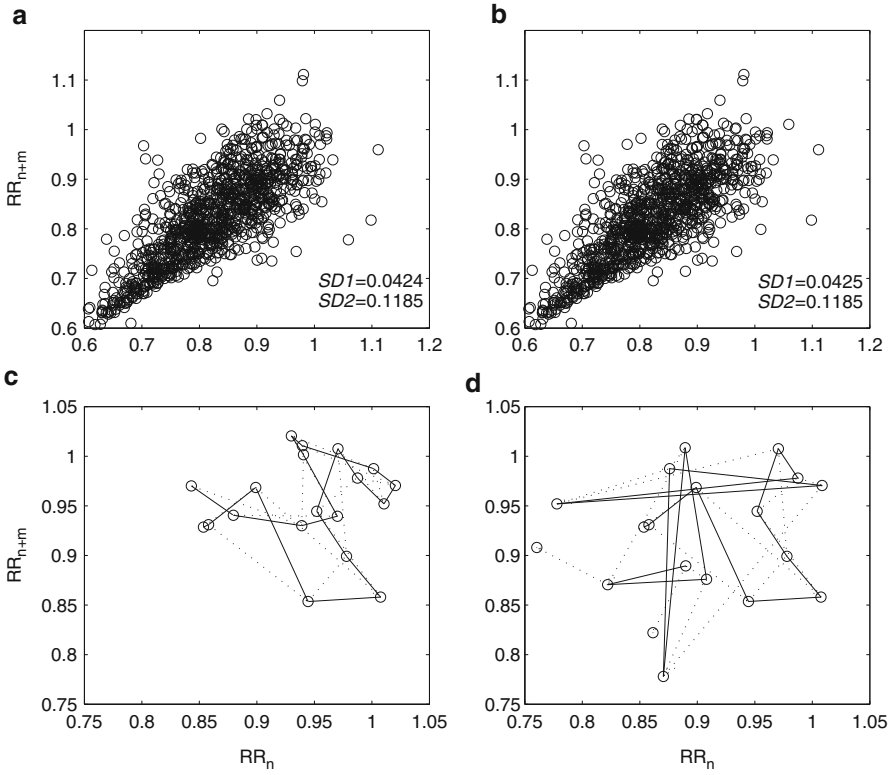

Fig. 4.1 Two different time series of length N ($N = 1,000$) with similar *SD1* and *SD2* values are shown ($m = 2$) on *top panel* (**a** and **b**). In the *bottom panel* (**c** and **d**) the underlying dynamics of first 20 points of both time series are shown to be different

Lerma et al. have shown that the measurement from a multiple lag Poincaré plot provides more information than any measure from single lag Poincaré plot [131]. Indeed, the Poincaré plot at any *lag-m* is more of a generalized scenario, where other levels of temporal variation of the dynamic system are hidden. As shown in equation sets 2.14 and 2.15, for any m, the descriptors *SD1* and *SD2* only indicate m lag correlation information of the plot. This essentially conveys overall behaviour of the system neglecting its detail temporal variation. The Poincaré plot of RR interval time series for three different lags is shown in Fig. 4.2. From the plots, it is obvious that for any time-series signal, different lag plots better reveal the behaviour of the signal than the single lag plot. The *CCM* is not only related to the *SD1* and *SD2*, but it also provides temporal information, which can be used to quantify the temporal dynamics of the system.

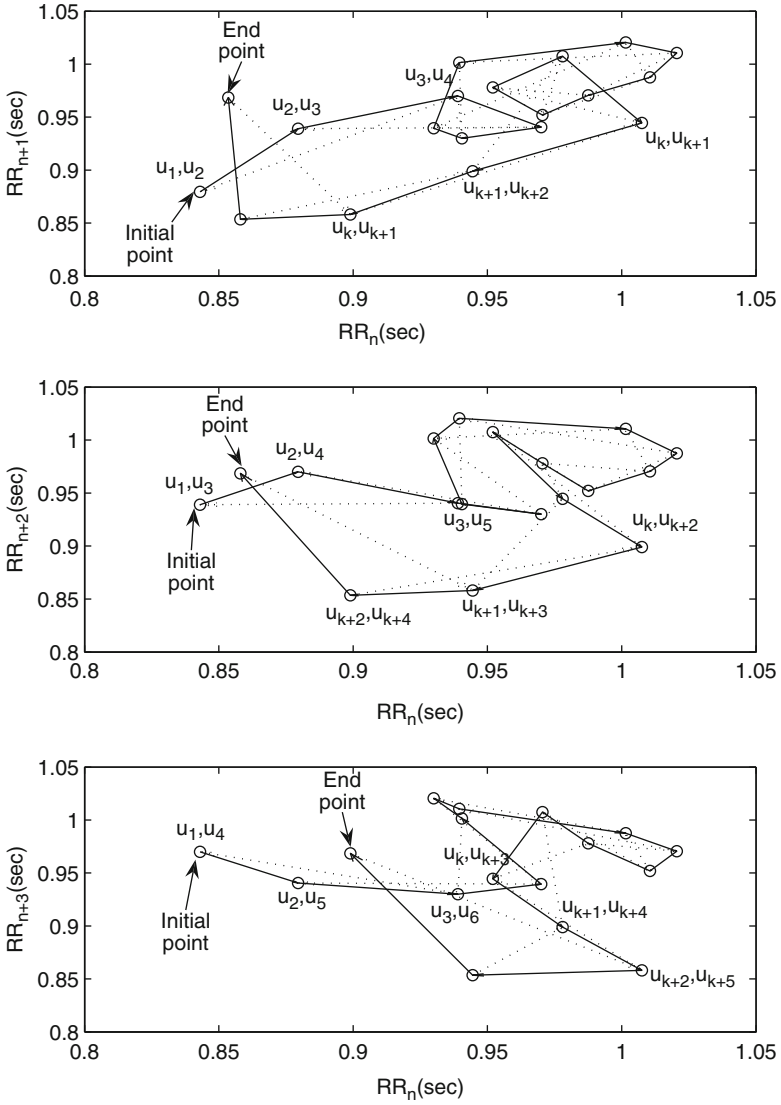

Fig. 4.2 Sequence of points (RR_n, $RR_{n+\tau}$) plotted and the *triangle* formed by each consecutive three points. Here, $m = \{1, 2, 3\}$ and $RR \equiv \{u_1, u_2, \ldots\ldots, u_N\}$.

4.4 Complex Correlation Measures in Poincaré Plot: A Novel Nonlinear Descriptor

The proposed descriptor *CCM* is computed using a moving window which embeds the temporal information of the signal. This moving window is comprised of three consecutive points from the Poincaré plot and the area of the triangle formed by

these three points is computed. This area measures the temporal variation of the points in the window. If three points are aligned on a line then the area is zero, which represents the linear alignment of the points. Moreover, since the individual measure involves three points of the two-dimensional plot, it is comprised of at least four different points of the time series for lag $m = 1$ and at most six points in case of lag $m \geq 3$. Hence the measure conveys information about four different lag correlations of the signal. Now, suppose the ith moving window is comprised of points $a(x1, y1)$, $b(x2, y2)$ and $c(x3, y3)$ then the area of the triangle (A) for ith window can be computed using the following determinant:

$$A(i) = \frac{1}{2}\begin{vmatrix} x1 & y1 & 1 \\ x2 & y2 & 1 \\ x3 & y3 & 1 \end{vmatrix}, \tag{4.1}$$

where A is defined on the real line $\Re$ and

$$\begin{aligned} A(i) &= 0, \text{ if points } a, b \text{ and } c \text{ are on a straight line} \\ &> 0, \text{ counterclockwise orientation the points } a, b \text{ and } c \\ &< 0, \text{ clockwise orientation of the points } a, b \text{ and } c. \end{aligned}$$

If Poincaré plot is composed of N points then the temporal variation of the plot, termed as *CCM*, is composed of all overlapping three point windows and can be calculated as

$$CCM(m) = \frac{1}{C_n(N-2)} \sum_{i=1}^{N-2} \|A(i)\|, \tag{4.2}$$

where m represents lag of Poincaré plot and C_n is the normalizing constant which is defined as $C_n = \pi * SD1 * SD2$ and represents the area of the fitted ellipse over Poincaré plot. The lengths of major and minor axis of the ellipse are $2SD1$ and $2SD2$.

Let the RR time series be composed of N RR interval values and defined as $RR \equiv u_1, u_2, \ldots, u_N$. As shown in Fig. 4.2, the *lag-1* Poincaré plot consists of $N-1$ numbers of 2D set of points PP, where $PP \in \{\Re, \Re\}$ can be represented by $PP \equiv \{(u_1, u_2), (u_2, u_3), \ldots, (u_{N-1}, u_N)\}$ and similarly for lag of m, $N-m$ numbers of 2D points are expressed as

$$PP \equiv \{(u_1, u_1+m), (u_2, u_2+m), \ldots, (u_{N-m}, u_N)\}.$$

Hence, for *lag-m* Poincaré plot, the first window will be composed of points $\{(u_1, u_{1+m}), (u_2, u_{2+m}), (u_3, u_{3+m})\}$ and from Eq. 4.1, the area A can be calculated as

$$A(1) = \frac{1}{2}[u_1u_{2+m} - u_1u_{3+m} + u_3u_{1+m} - u_2u_{1+m} + u_2u_{3+m} - u_3u_{2+m}]. \tag{4.3}$$

Similarly the second and $(N-m-2)$th window is composed of points $\{(u_2, u_{2+m}), (u_3, u_{3+m}), (u_4, u_{4+m})\}$ and $\{(u_{N-m-2}, u_{N-2}), (u_{N-m-1}, u_{N-1}), (u_{N-m}, u_N)\}$ respectively. Hence, the area, A, for second and $(N-m-2)$th window can be calculated as

$$\begin{aligned} A(2) = \frac{1}{2}[&u_2u_{3+m} - u_2u_{4+m} + u_4u_{2+m} - u_3u_{2+m} \\ &+u_3u_{4+m} - u_4u_{3+m}] \end{aligned} \tag{4.4}$$

$$\begin{aligned} A(N-m-2) = \frac{1}{2}[&u_{N-m-2}u_{N-1} - u_{N-m-2}u_N + u_{N-m}u_{N-2} \\ &-u_{N-m-1}u_{N-2} + u_{N-m-1}u_N - u_{N-m}u_{N-1}]. \end{aligned} \tag{4.5}$$

Using Eqs. 4.2–4.5, $CCM(m)$ is calculated as follows:

$$\begin{aligned} CCM(m) = \frac{1}{2C_n(N-2)} \Bigg[&u_{N-m}u_{N-1} + u_2u_{1+m} - u_{N-1-m}u_N - u_1u_{2+m} + \sum_{i=3}^{N-m} u_iu_{i-2+m} \\ &-2\sum_{i=2}^{N-m} u_iu_{i-1+m} + 2\sum_{i=1}^{N-1-m} u_iu_{i+1+m} - \sum_{i=1}^{N-2-m} u_iu_{i+2+m} \Bigg]. \end{aligned} \tag{4.6}$$

Since RR intervals are discrete signal, the autocorrelation at lag $m = j$ can be calculated as

$$\gamma_{RR}(j) = \sum_{n=1}^{N} RR_nRR_{n+j}. \tag{4.7}$$

Using Eqs. 2.14, 2.15, 4.6 and 4.7, $CCM(m)$ can now be expressed as a function of autocorrelation at different lags. Hence,

$$CCM(m) = F\left[\gamma_{RR}(0), \gamma_{RR}(m-2), \gamma_{RR}(m-1), \gamma_{RR}(m+1), \gamma_{RR}(m+2)\right]. \tag{4.8}$$

In the Eq. 4.8, $CCM(m)$ represents the point-to-point variation of the Poincaré plot with *lag-m* as a function of autocorrelation of lags $0, m-2, m-1, m+1$ and $m+2$. This supports our hypothesis that *CCM* is measured using multiple lag correlation of the signal rather than single lag. For the conventional *lag-1* Poincaré plot $CCM(1)$ can be represented as

$$CCM(1) = F\left[\gamma_{RR}(-1), \gamma_{RR}(0), \gamma_{RR}(2), \gamma_{RR}(3)\right]. \tag{4.9}$$

4.5 Mathematical Analysis of *CCM*

The *CCM* has been mathematically defined and its relation with multiple lag correlation information of the signal has been presented in the previous section. In this section, we explore the different properties of *CCM* with synthetic RR interval data.

4.5.1 Sensitivity Analysis

The sensitivity is defined as the rate of change of the value due to the change in temporal structure of the signal. The change in temporal structure of the signal in a window is achieved by surrogating the signal (i.e. data points) in that window. Sensitivity analysis of *CCM* will reveal the minimum length of the signal required to obtain a consistent *CCM* value. From the mathematical definition of *CCM*, we anticipated that *CCM* would be more sensitive to changes in temporal structure within the signal than the standard descriptors. We have compared the sensitivity of *CCM* with standard descriptors (*SD1*, *SD2*) in order to validate our assumption. A synthetic RR interval (*rr02*) time-series data from the open-access Physionet database [134] is used to validate the sensitivity analysis.

4.5.1.1 Sensitivity to Changes in Window Length

The sensitivity of *CCM* with different window lengths was analysed in order to define how it was affected by increasing the amount of change in temporal structure. The minimum number of samples required for using *CCM* as a measurement tool can also be defined using this analysis. The sensitivity to changes in window length is measured by increasing the window length in each step, changing the temporal structure of that window using surrogation and then calculating the *CCM* of the changed signal. Increased window length effectively increases the number of surrogating points, which results in increased probability of the amount of change in temporal structure of the time-series signal. At each step the number of surrogated points is increased by 50. We calculated *SD1*, *SD2* and *CCM* of the RR interval signal by increasing the number of surrogating points at a time. For a selected window length, we have shuffled the points 30 times, to minimize impact of bias of randomization, and calculated all descriptors each time after shuffling. Finally the surrogated values of descriptors were taken as a mean of the calculated values.

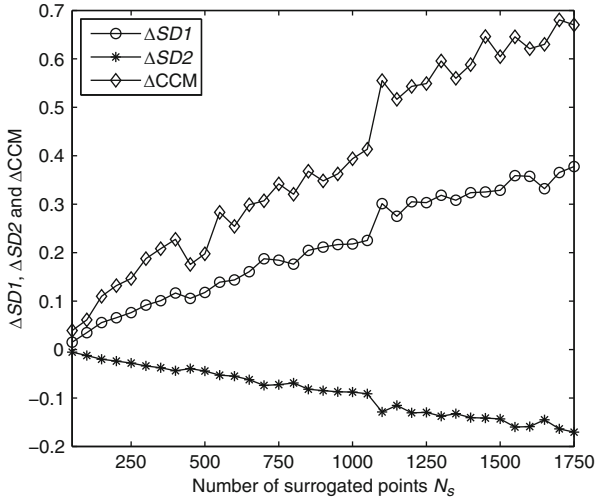

Fig. 4.3 Sensitivity of *SD1*, *SD2* and *CCM* with number of shuffled points N_s. At each step the number of shuffled points increased by 50. Each time the signal has been shuffled for 30 times and its mean has been taken to calculated the sensitivity

Then the sensitivity of descriptors $\Delta SD1_j$, $\Delta SD2_j$ and ΔCCM_j was calculated using Eqs. 4.10–4.12:

$$\Delta SD1_j = \frac{SD1_j - SD1_0}{SD1_0} \tag{4.10}$$

$$\Delta SD2_j = \frac{SD2_j - SD2_0}{SD2_0} \tag{4.11}$$

$$\Delta CCM_j = \frac{CCM_j - CCM_0}{CCM_0}, \tag{4.12}$$

where $SD1_0 = 0.36$, $SD2_0 = 0.08$ and $CCM_0 = 0.16$ were the parameters measured for the original data set without surrogation and j represents the window number whose data were surrogated and where, $SD1_j$, $SD2_j$ and CCM_j represent the *SD1*, *SD2* and *CCM* values, respectively, after surrogation of jth step.

The change of descriptors *SD1*, *SD2* and *CCM* with increasing number of shuffled RR intervals is presented in Fig. 4.3. From Fig. 4.3 it is obvious that the rate of change with number of shuffled RR intervals was higher for *CCM* at any point than *SD1* and *SD2*. Therefore, we can conclude that *CCM* is more sensitive than *SD1* and *SD2* with respect to change in temporal structure or the change in autocorrelation of the signal which was earlier reported by Karmakar et al. [135]. Moreover, sensitivity of *CCM* with small number of RR intervals increases its applicability to short-length HRV signal analysis.

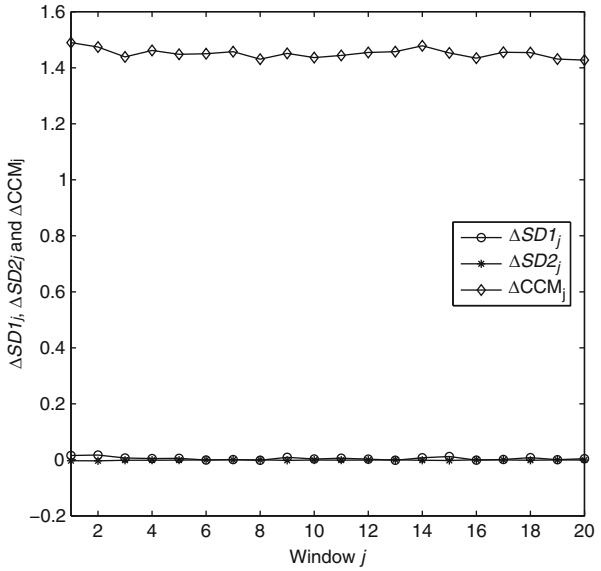

Fig. 4.4 Rate of change of values of *SD1*, *SD2* and *CCM* with surrogated data points within a window j over the whole data set

4.5.1.2 Homogeneity to Changes in Temporal Structure

In order to observe the homogeneity of sensitivity of *CCM* with changes in temporal structure over the whole timeline of the signal, we have used a fixed-length moving window, changed the temporal structure of that window using surrogation and then calculated *CCM* value of the changed signal. We have divided the signal into 20 windows with 200 samples in each of them. To minimize the bias from surrogated values, we have shuffled the points of each window 30 times and calculated all descriptors each time after shuffling. Finally, the surrogated values of descriptors were taken as a mean of the calculated values. Since we divided the entire signal into 20 windows, it resulted in 20 values of *SD1*, *SD2* and *CCM*. The sensitivity of descriptors $\Delta SD1_j$, $\Delta SD2_j$ and ΔCCM_j was calculated using Eqs. 4.10–4.12. Similar to the previous section, $SD1_0$, $SD2_0$ and CCM_0 were the parameters measured for the original data set without surrogation and j represents the window number whose data were surrogated.

Value of ΔCCM is significantly higher than $\Delta SD1$ and $\Delta SD2$ which indicates that *CCM* is much more sensitive than *SD1* and *SD2* to the underlying temporal structure of the data (Fig. 4.4). This supports the mathematical definition of *CCM* as a sensitive measure of temporal variation of the signal. The little variation in ΔCCM value shows that different temporal position of changes in temporal structure does not impact the *CCM* value, which means the homogeneity of *CCM* over time. Hence, *CCM* reflects changes in temporal structure of the signal irrespective of the time.

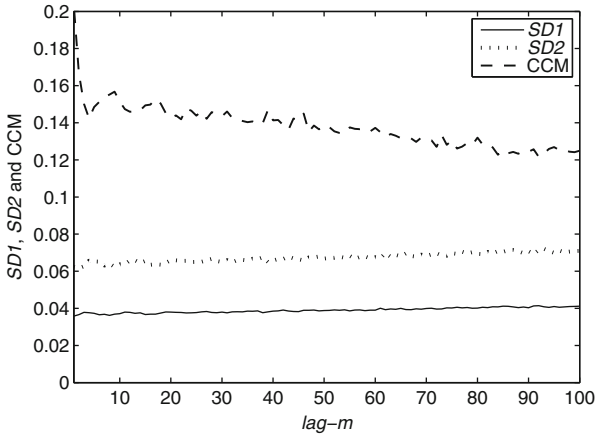

Fig. 4.5 Values of *SD1*, *SD2* and *CCM* for different *lag-m*

4.5.1.3 Examining the Influence of Various *lag*s of Poincaré Plot

One of the variations commonly used in order to optimize the use of the Poincaré plot as a quantitative tool is the lagged Poincaré plot [112, 136]. In several studies, it is also reported that the use of quantitative tool on multiple lagged Poincaré plot might be useful to distinguish normal from pathological heart rate signal [131, 132, 136]. Therefore, analysis of lag response might give a comprehensive idea about the use of *CCM*, as a new quantitative tool, in different physiological conditions.

To quantify the influence of various lags of Poincaré plot on *SD1*, *SD2* and *CCM*, values of all descriptors were calculated for different time delays or lags (*m* was varied in increments from 1 to 100). At each step, *lag-m* Poincaré plot was constructed and then *SD1*, *SD2* and *CCM* values were calculated for the plot.

The relationship of *CCM*, *SD1* and *SD2* with different lags (*m* was varied from 1 to 100) is shown in Fig. 4.5. A unit lag is used to create the Poincaré plot which confirms the maximum linear correlation among data points. This lag selection may have obscured the low-level nonlinearities of the signal and as a result *CCM* may be unable to show better performance over standard poincaré descriptors. In contrast, at higher lags, the standard descriptors are unable to capture the system dynamics. It is also established in the literature that studying behaviour of descriptors as a function of lags is more informative [132]. In our analysis, we have found that over different lags, *CCM* shows more variability than *SD1* and *SD2*. Among the three descriptors the change in values for *CCM* was higher than both *SD1* and *SD2* which again supports our claim of sensitivity of *CCM* with signal dynamics. Hence, we conclude that the change in underlying temporal structure due to lag of the Poincaré plot has higher impact on *CCM* than the traditional descriptors.

4.6 Physiological Relevance of *CCM* with Cardiovascular System

In this chapter, we demonstrate the physiological significance of the novel measure *CCM* by analysing the effects of perturbations of autonomic function on Poincaré plot descriptors (*SD1* and *SD2*) in HRV signal of young healthy human subjects caused by the 70° head-up tilt test, atropine infusion and transdermal scopolamine patch administration. A surrogate analysis is also performed on the data to show that changes found in different phases of the activity are due to perturbed autonomic activity rather than noise.

4.6.1 Subjects and Study Design

In this analysis, five subjects were studied with normal sinus rhythm, who did not smoke, had no cardiovascular abnormalities and were not taking any medications. Subjects were aged between 20 and 40 years (30.2 ± 7.2 years). All studies were performed at the same time of the day without any disturbances. No respiration control was performed because all phases of the study were conducted in the resting state. An intravenous cannula was inserted into an antecubital vein and subjects then rested 20 min before commencement of data collection. The length of the study varied from 10 to 20 min. For autonomic perturbations the following sequence of protocol was performed. At least 20 min was allowed between each phase to permit the heart rate to return to baseline. Details of the study design and data collection were published in [94]. The sequence of phases was maintained strictly as follows:

Baseline Study

All baseline studies were conducted in subjects in the post-absorptive state after resting for 10 min in the supine position.

Seventy Degree Head-Up Tilt

Data were collected after subjects were tilted 70° on a motorized table. This manoeuvre increases sympathetic and decreases parasympathetic nervous system activity [137]. To permit the heart rate to stabilize at new position, data were collected 5 min after the subjects were tilted.

Atropine Infusion

Atropine sulphate (1.2 mg) was added to 50 ml of 5 intravenous dextrose and infused at a rate of 0.12 mg/min for 5 min and then at a rate of 0.24 mg/min until completion of this phase of study. Use of this dose regimen reduces parasympathetic nervous system activity significantly [138]. After 10 min of infusion of atropine, the data collection started.

Transdermal Scopolamine

One week after the above studies, a low-dose transdermal scopolamine patch (hyoscine 1.5 mg) was applied overnight to an undamaged hair-free area of the skin behind the ear. The patch remained in situ for the duration of this period of the study. La Rovere et al. have shown that low-dose transdermal scopolamine increases parasympathetic nervous system activity [139].

4.6.2 Results

The RR intervals and the corresponding Poincaré plot for all four phases of the experiment with the same subject are shown in Fig. 4.6. From Fig. 4.6 it is eminent that the atropine infusion strongly reduces the size of plot by reducing both the RR interval (increase in heart rate) and its variation. Whereas, the head-up tilt position reduces the RR interval (increase in heart rate) variability markedly with respect to the baseline. In contrast, use of low-dose transdermal scopolamine increases the RR interval (reduces heart rate) and its variability resulted into a wider Poincaré plot in terms of width in both directions (perpendicular to line of identity and along the line of identity).

The mean and standard deviation of heart rate variability features of all subjects in all four phases are summarized in Table 4.1. Short-term variability (*SD1*) was increased in scopolamine phase and decreased in atropine phase. A similar trend was also found for long-term variability (*SD2*). Changes of *SD1* values from phase to phase were much higher than that of *SD2*. *CCM* value was also minimum in atropine phase and maximum at scopolamine phase. Changes in mean values of *CCM* between study phases were higher than both *SD1* and *SD2* (Table 4.1). Moreover, changes in *CCM* values in atropine, 70° head-up tilt and scopolamine phases from baseline are found significant ($p < 0.01$). Whereas, *SD1* values were significantly different in atropine and 70° Head-up tilt phases and *SD2* values only in atropine phase.

The errorbars of log-scaled *SD1*, *SD2* and *CCM* values for four groups of subjects are shown in Fig. 4.7. The atropine administration resulted into reduction in mean value of *SD1* (*SD* of ΔRR) all subjects which was also reported by Kamen et al. [94]. The similar effect was also found for *SD2* and *CCM*. The use of scopolamine patch increased both the width and height of the Poincaré plot which resulted in the

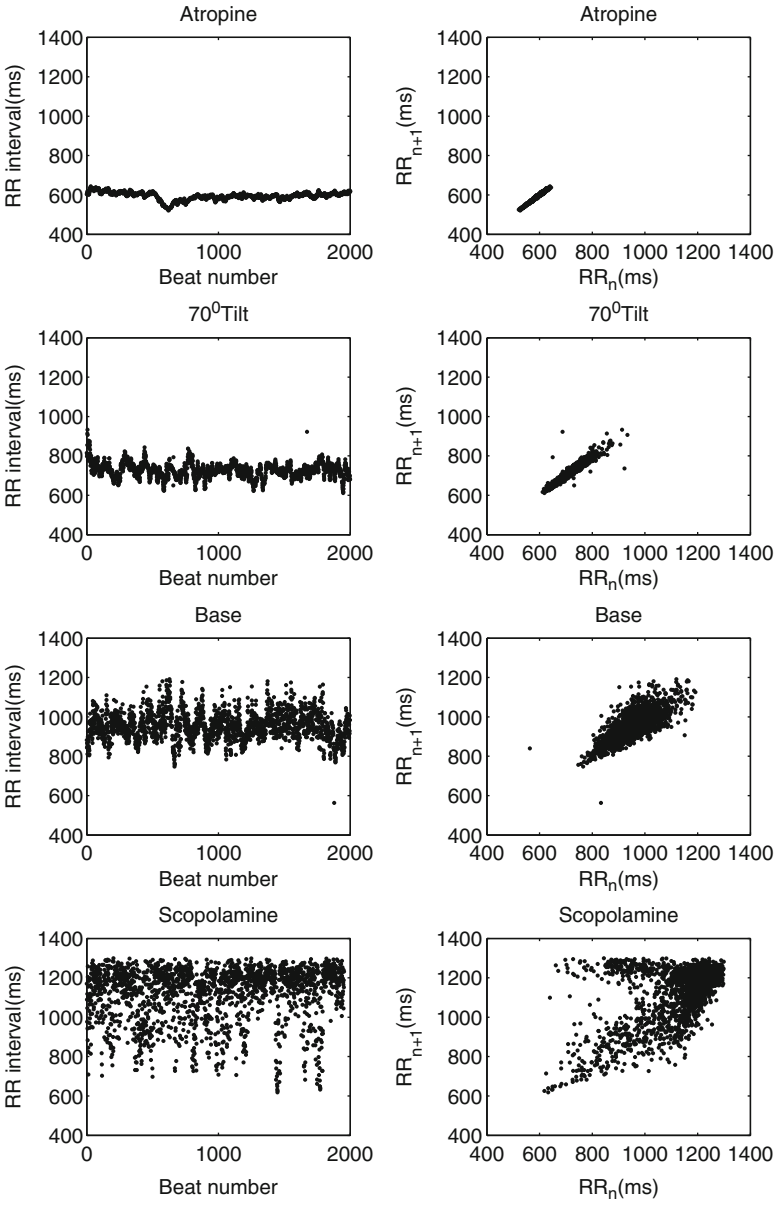

Fig. 4.6 RR interval time series for single subject from all four phases of study with corresponding Poincaré plot

Table 4.1 *Mean* and standard deviation *SD* of values of all descriptors for *lag-1* Poincaré plot

Feature	*SD1* (mean ± sd) (ms)	*SD2* (mean ± sd) (ms)	*CCM* (mean ± sd)
Atropine	4.45 ± 2.45*	43.11 ± 13.79*	3.88E-02 ± 1.05E−02*
Head-up tilt	11.96 ± 5.47	70.77 ± 13.98	6.29E-02 ± 2.08E−02*
Baseline	28.74 ± 9.28	85.94 ± 11.27	1.50E-01 ± 3.40E-02
Scopolamine	69.90 ± 21.25*	103.05 ± 20.05	2.75E-01 ± 2.14E−02*

SD1, *SD2* and *CCM* values of all subjects ($N = 5$) were calculated for four phases as described in Sect. 4.6.1. * indicates the value of the feature in corresponding phase is significantly ($p < 0.01$) different from baseline phase using Wilcoxon rank-sum test

increase in mean values of *CCM* as well as *SD1* and *SD2*. All subjects have shown a marked reduction in *SD1*, *SD2* and *CCM* values in 70° head-up tilt phase compared to the baseline.

4.6.3 Physiological Relevance of CCM

Quantitative Poincaré plot analysis was used to assess the changes in HRV during parasympathetic blockade [111] and compared the results with power spectral analysis of HRV, which was the commonly used method in the measurement of sympathovagal interaction [13, 103, 111, 140]. It was also reported that Poincaré analysis method can provide the heart rate dynamics that is not detected by the conventional time-domain methods [111]. The present quantitative analysis was performed to measure the instantaneous beat-to-beat variance of RR intervals (*SD1*), the long-term continuous variance of all RR intervals (*SD2*) and the variation in temporal structure of all RR intervals (*CCM*). Instantaneous changes in RR intervals are mediated by vagal efferent activity, because vagal effects on the sinus node are known to develop faster than sympathetically mediated effects [101, 124]. The maximum reduction in *SD1* during atropine infusion compared to baseline values confirms that *SD1* quantifies the vagal modulation of heart rate, which was also reported by Kamen et al. [94] and Tulppo et al. [111]. Similar reduction in *CCM* value could be observed (Table 4.1 and Fig. 4.7), which indicates that *CCM* might correlate the parasympathetic nervous system activity. The lowest value of *CCM* has also been found during atropine infusion which reduced the parasympathetic activity and reduces instantaneous changes in HRV signal. Moreover, significant ($p < 0.01$) change in *CCM* values in all phases from baseline phase compared to *SD1* and *SD2* indicates that *CCM* is more sensitive to changes in parasympathetic activity (Table 4.1). On the contrary, changes in *SD1* values are insignificant in 70° head-up tilt phase and changes in *SD2* values are insignificant both in 70° head-up tilt and scopolamine phases.

Reciprocal changes in sympathetic and parasympathetic activity occur during head-up tilt phase. The RR interval decreases and the high-frequency power of RR intervals decreases during the head-up tilt phase as evidence of withdrawal

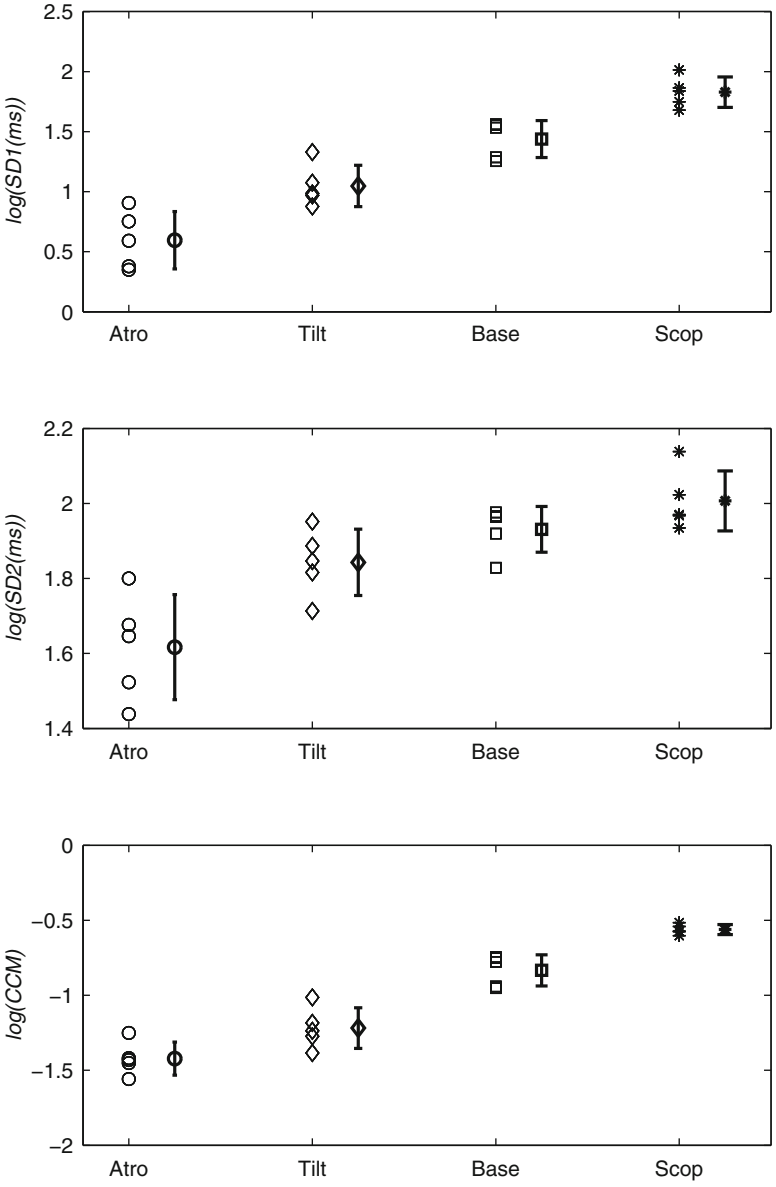

Fig. 4.7 Errorbar ($n = 5$) of $log(SD1)$, $log(SD2)$ and $log(CCM)$ for atropine (Atro), 70° head-up tilt (Tilt), baseline (Base) and scopolamine (Scop) phase. All values were calculated for short-segment (~ 20 min) RR interval time-series signal

of vagal activity (decrease in parasympathetic activity) [104, 141, 142]. The short-term variability measure of Poincaré plot (*SD1*) also decreases and correlates with high-frequency power as reported by Kamen et al. [94]. In this study, *SD1* value decreased during 70° head-up tilt phase compared to baseline, which supports the results reported by previous studies [94, 137]. The *CCM* value has also decreased in 70° head-up tilt phase compared to baseline, which indicates that *CCM* value is modulated by the vagal tone (parasympathetic activity). Therefore, changes in autonomic regulation caused by 70° head-up tilt phase resulted in concordant changes in the temporal structure of the Poincaré plot of RR intervals.

The low-dose transdermal scopolamine patch may decrease heart rate by a paradoxical vagomimetic effect [139]. Delivery by transdermal patch substantially increases both baseline and reflexly augmented levels of cardiac parasympathetic activity over 24 h in normal subjects [143, 144]. Both time-domain HRV (mean, SD) and frequency-domain HRV (high-frequency power) increased to a greater extent during administration of low-dose scopolamine, which indicates the increase in parasympathetic activity [139]. The increase in parasympathetic activity decreases the heart rate and increases the RR interval as well as instantaneous variance in the RR, as measured by *SD1* of Poincaré plot. The increased value of *SD1* correlates with increase high-frequency power and supported by the previous study reported by Kamen et al. [94]. In this study, the variability in the temporal structure of the Poincaré plot (measured as *CCM*) was also found to be increased with increase in parasympathetic activity during administration of low-dose scopolamine (Fig. 4.7, Table 4.1). The increase in *CCM* value indicates that it reflects the change in parasympathetic activity harmoniously.

4.7 Clinical Case Studies Using *CCM* of Poincaré Plot

In order to validate the proposed measure "*CCM*" two case studies were conducted on RR interval data. The data from MIT-BIH Physionet database are [145] used in the analysis. The medical fraternity has utilized Poincaré plot, using both qualitative and quantitative approaches, for detecting and monitoring arrhythmia. Compared to arrhythmia, fewer attempts have been made to utilize Poincaré plot to evaluate CHF. In this study, we have analysed the performance of *CCM* and compared it with that of *SD1* and *SD2* for recognizing both arrhythmia and CHF using HRV signals.

4.7.1 HRV Studies of Arrhythmia and Normal Sinus Rhythm

In this study, we have used 54 long-term ECG recordings of subjects in normal sinus rhythm (30 men, aged 28.5–76, and 24 women, aged 58–73) from Physionet Normal Sinus Rhythm database [145]. Furthermore, we have also used NHLBI-sponsored cardiac arrhythmia suppression trial (CAST) RR-Interval Sub-study database for the arrhythmia data set from Physionet. Subjects of CAST database had an acute

myocardial infarction (MI) within the preceding 2 years and 6 or more ventricular premature complexes (PVCs) per hour during a pre-treatment (qualifying) long-term ECG (Holter) recording. Those subjects enrolled within 90 days of the index MI were required to have left ventricular ejection fractions less than or equal to 55 %, while those enrolled after this 90 day window were required to have an ejection fraction less than or equal to 40 %.

The database is divided into three different study groups, among which we have used the Encainide (e) group data sets for our study. From that group we have chosen 272 subjects belonging to subgroup baseline (no medication). The original long-term ECG recordings were digitized at 128 Hz, and the beat annotations were obtained by automated analysis with manual review and correction [145]. *lag-1* Poincaré plots were constructed for both normal and arrhythmia subjects and the new measure *CCM* was computed along with *SD1* and *SD2*. The *SD1* and *SD2* were calculated to characterize the distribution of the plots, whereas *CCM* values were used for characterizing the temporal structure of the plots.

Figure 4.8a represents box-whiskers (BW) plot for $log(SD1)$ and it is obvious that boxes (interquartile range) of normal and arrhythmia subjects are non-overlapping. But the whiskers (upper quartile) of normal subjects completely overlap with the whiskers (lower quartile) of the arrhythmia subjects. In Fig. 4.8b, the BW plot of $log(SD2)$ is shown and it is apparent that the BW of normal subjects completely overlapped with the whiskers (lower quartile) of the arrhythmia subjects. But the box of arrhythmia subjects is still non-overlapping with the whiskers (upper quartile) of the normal subjects. In Fig. 4.8c, the BW plot of $log(CCM)$ is shown and it is obvious that both of them are non-overlapping and distinct.

The p values obtained from ANOVA analysis between two groups for *SD1*, *SD2* and *CCM* are given in Table 4.2. Using ANOVA, for *CCM*, $p = 6.28 \times 10^{-18}$ is obtained, whereas for *SD1* and *SD2*, it is 7.6×10^{-3} and 8.5×10^{-3}, respectively. In case of $p < 0.001$ to be considered as significant, only *CCM* would show the significant difference between two groups which indicates that *CCM* is a better descriptor of HRV signal than *SD1* and *SD2* when comparing arrhythmia with normal sinus rhythm subjects.

4.7.2 HRV Studies of Congestive Heart Failure and Normal Sinus Rhythm

For this case study, we have used 29 long-term ECG recordings of subjects (aged 34 to 79) with CHF (NYHA classes I, II and III) from Physionet CHF database along with 54 ECG recordings of subjects with normal sinus rhythm as discussed earlier [145]. The same ECG acquisition with beat annotations was used as discussed in the previous case study. Similar to the previous case study, *lag-1* Poincaré plots were constructed for both normal and CHF subjects and the new descriptor *CCM* was computed as per traditional descriptors.

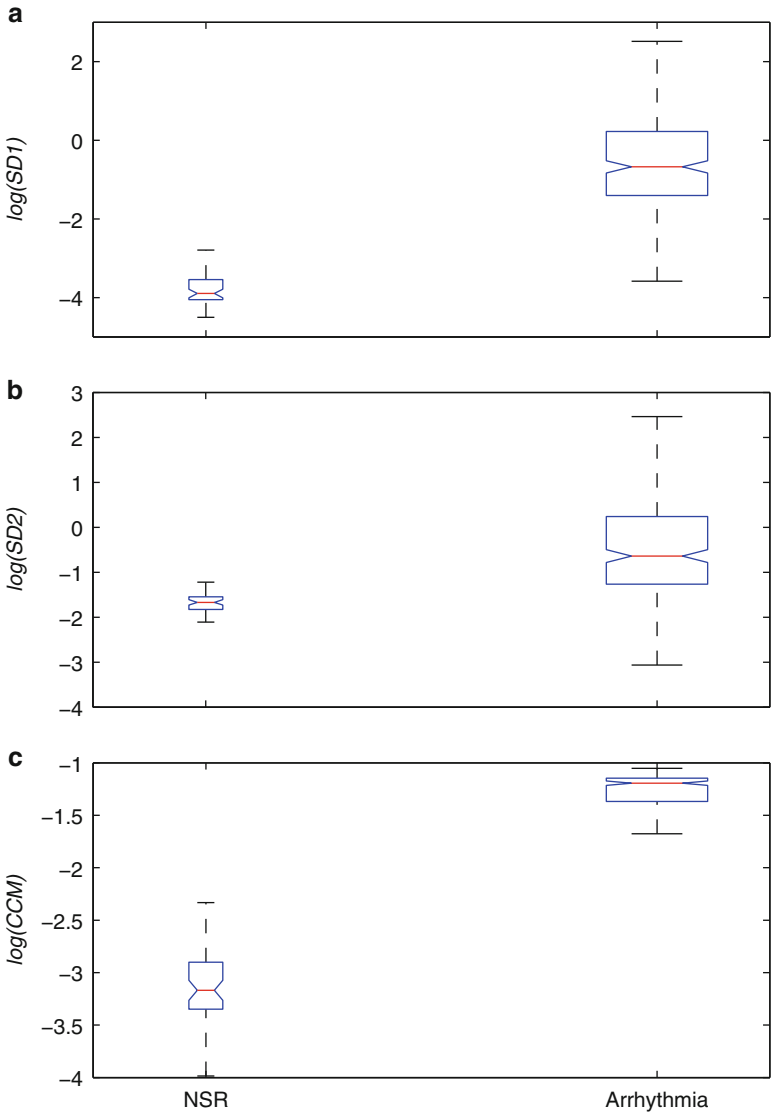

Fig. 4.8 Box-whiskers plot of (**a**) *SD1*, (**b**) *SD2* and (**c**) *CCM* for normal sinus rhythm (NSR, $n = 54$) and arrhythmia ($n = 272$) subjects

Figure 4.9a represents BW plot for $log(SD1)$ and it is apparent that boxes (interquartile range) of normal and CHF subjects are overlapping. The BW of normal subjects is completely overlapped with the box and whisker (lower quartile) of the CHF subjects. In Fig. 4.9b, the box-whiskers plot of $log(SD2)$ is shown and boxes are apparently non-overlapped. But the BW plot of normal subjects mostly

Table 4.2 *Mean* ± *standard deviation* of *SD1*, *SD2* and *CCM* for normal and arrhythmia subjects

	SD1	*SD2*	*CCM*
Normal	0.03 ± 0.02	0.19 ± 0.04	0.05 ± 0.03
arrhythmia	1.92 ± 5.18	2.30 ± 5.86	0.26 ± 0.08
p value (ANOVA)	7.60E−3	8.50E−3	6.28E−18

p values from ANOVA analysis are given in the last row

overlaps with the whisker (upper quartile) of the CHF subjects. In Fig. 4.9c, the BW plot of $log(CCM)$ is shown to be non-overlapping and only the upper quartile (box) and whisker of normal subjects are overlapped with the whisker (lower quartile) of the CHF subjects.

The values of the mean and the standard deviation for both types of subjects are shown in Table 4.3. Last row represents the p value obtained from ANOVA analysis between the two groups for *SD1*, *SD2* and *CCM*. Though *SD2* and *CCM* show similar difference between the mean of two subject groups, the *standard deviation* of *CCM* is lower which concentrates with the distribution of *CCM* values around mean comparing with that of *SD2*. The p value, obtained from ANOVA analysis for *CCM* ($p = 9.07 \times 10^{-14}$), shows more significance than *SD1* and *SD2*.

4.8 Critical Remarks on *CCM*

The main motivation for using Poincaré plot is to visualize the variability of any time-series signal. In addition to this qualitative approach, we propose a novel quantitative measure, *CCM*, to extract underlying temporal dynamics in a Poincaré plot. Surrogate analysis showed that the standard quantitative descriptors *SD1* and *SD2* were not as significantly altered as did *CCM*, this is shown in Fig. 4.3. Both *SD1* and *SD2* are second-order statistical measures [112], which are used to quantify the dispersion of the signal perpendicular and along the line of identity, respectively. Moreover, *SD1* and *SD2* are functions of *lag-m* correlation of the signal for any m lag Poincaré plot. In contrast, *CCM* is a function of multiple lag ($m-2$, $m-1$, m, $m+1$, $m+2$) correlations and hence, this measure was found to be sensitive to changes in temporal structure of the signal as shown in Fig. 4.3.

From the theoretical definition of *CCM* it is obvious that the correlation information measured in *SD1* and *SD2* is already present in *CCM*. But this does not mean that *CCM* is a derived measure from existing descriptors *SD1* and *SD2*. Rather, *CCM* can be considered as an additional measure incorporating information obtained in *SD1* and *SD2* (as the *lag-m* correlation is also included in *CCM* measure). In a Poincaré plot, it is expected that lag response is stronger at lower values of m and it attenuates with increasing values of m. This is due to the dependence of Poincaré descriptors on autocorrelation functions. The autocorrelation function monotonically decreases with increasing lags and in case of RR interval time series,

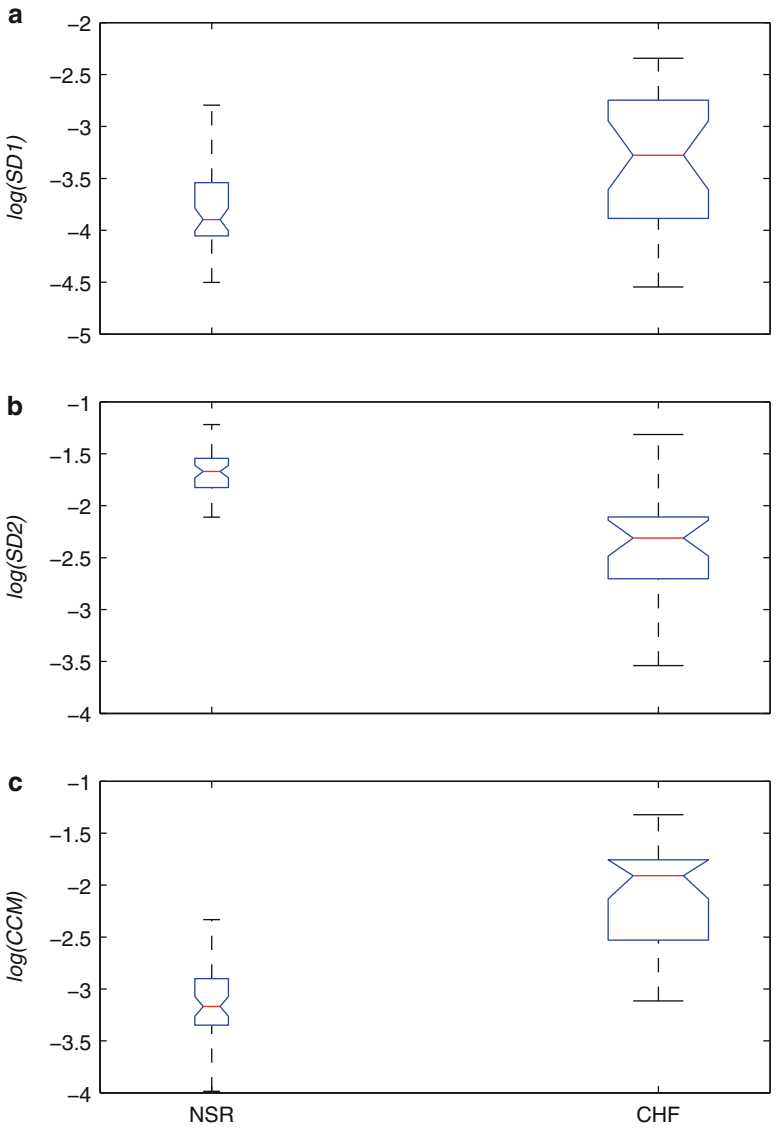

Fig. 4.9 Box-whiskers plot of (**a**) *SD1*, (**b**) *SD2* and (**c**) *CCM* for normal sinus rhythm (NSR, $n = 54$) and congestive heart failure (CHF, $n = 29$) subjects

usually the current beat influences only about six to eight successive beats [132]. In this study, we also found that all measured descriptors *SD1*, *SD2* and *CCM* changed rapidly at lower lags and the values are stabilized with higher lag values (Fig. 4.5). Since *CCM* is also a function of the signals autocorrelations, it shows a

Table 4.3 *Mean* ± *standard deviation* of *SD1*, *SD2* and *CCM* for normal and congestive heart failure (CHF) subjects

	SD1	*SD2*	*CCM*
Normal	0.03 ± 0.02	0.19 ± 0.04	0.05 ± 0.03
CHF	0.04 ± 0.02	0.11 ± 0.06	0.14 ± 0.06
p value (ANOVA)	5.65E−4	5.04E−12	9.07E−14

p values from ANOVA analysis are given in the last row

similar lag response to that shown by *SD1* and *SD2*. Therefore, *CCM* may be used to study the lag response behaviour of any pathological condition in comparison with normal subjects or controls.

HRV measure is considered to be a better marker for increased risk of arrhythmic events than any other non-invasive measure [146, 147]. An earlier study has shown that Poincaré plots exposed completely different 2D patterns in the case of arrhythmia subjects [148]. These abnormal medical conditions have complex patterns due to reduced autocorrelation of the RR intervals. Consequently due to the changes in autocorrelation, we have found that the variability measure using Poincaré (*SD1*, *SD2*) was higher than normal subjects (shown in Table 4.2). Moreover, the fluctuations of these variability measures were also very high in the case of arrhythmias. This may be due to different types of arrhythmia along with subjective variation of HRV. In arrhythmia subjects, *CCM* was found to be higher compared to NSR subjects, but the deviation due to subjective variation is much smaller than *SD1* and *SD2*. As a result, *CCM* linearly separates these two groups of subjects which means that the effect of different types of arrhythmia and subjective variation are reduced while using *CCM* than other variability measures. Therefore, we may conclude that *CCM* is a better marker for recognizing arrhythmia than the traditional variability measures of Poincaré plot.

In case study, we have also shown how the Poincaré plot can be used to characterize CHF subjects from normal subjects using RR interval time series. Compared to *SD2*, *SD1* and *CCM* values were found to be higher in CHF subjects. This finding might indicate that the short-term variation in HRV is higher in CHF subjects; however, the long-term variation is reduced. Since *CCM* captures the signal dynamics at short level (i.e, three points of the plot), it appears to be affected by short-term variation of the signal in CHF subjects. In the case of recognition of CHF subjects, although *SD2* showed good results, *CCM* was found to be more significant (Table 4.3).

So far the discussion indicates that *CCM* is an additional descriptor of Poincaré plot along with *SD1* and *SD2*. This also implies that *CCM* is a more consistent descriptor compared to *SD1* and *SD2*. Considering the presented case studies, it is clear that neither *SD1* nor *SD2* alone can independently distinguish NSR subjects from CHF and arrhythmia subjects. However, in the same scenario, *CCM* has the ability to perform the classification task independently. This justifies the usefulness of the proposed descriptors as a feature in a pattern recognition scenario. Our primary motivation for detecting pathology with a novel descriptor like *CCM*

rather than by observing a visual pattern is achieved, as shown by the case studies described. Although we have not looked at the physiological interpretation of *CCM*, the following remarks are relevant. The Poincaré plot reflects the autocorrelation structure through the visual pattern of the plot. The standard descriptors *SD1* and *SD2* summarize the correlation structure of RR interval data as shown by Brennan et al. [112]. *CCM* is based on the autocorrelation at different lags of the time series, hence giving an in-depth measurement of the correlation structure of the plot. Therefore, the value of *CCM* decreases with increased autocorrelation of the plot. In arrhythmia, the pattern of the Poincaré plots becomes more complex [148], thus reducing the correlation of the signal (RR_i, RR_{i+1}). In case of healthy subjects the value of *CCM* is lower than that of arrhythmic subjects. In the future, the performance of CCM for other pathologies might be worth looking.

4.9 Conclusion

CCM is developed based on the limitation of standard descriptors *SD1* and *SD2*. The analysis carried out confirms the hypothesis that *CCM* measures the temporal variation of the Poincaré plot. In contrast to the standard descriptors, *CCM* evaluates point-to-point variation of the signal instead of gross variability. *CCM* is more sensitive to changes in temporal variation of the signal and varies with different lags of Poincaré plot. Besides the mathematical definition of *CCM* and analysing properties of the measure, *CCM* was found to be effective in the assessment of different physiological and pathological conditions.

Chapter 5
Heart Rate Asymmetry Analysis Using Poincaré Plot

Abstract Physiological systems are inherently complex and subject to energy, entropy and information fluxes across their boundaries. These systems function in disequilibrium in healthy condition and their self-organizing capability is related to asymmetricity of the underlying processes (Costa et al., Phys. Rev. Lett. **95**:1–4, 2005). In pathological perturbations, a loss of self-organizing capability associated with aging or disease is a function of loss of asymmetricity (Costa et al., Phys. Rev. Lett. **95**:1–4, 2005). Intuitively, asymmetry refers to the lack of symmetry; in other words, the distribution of signals is imbalanced. This imbalance or dissimilarity can easily be observed in geometry of the phase space plots. Asymmetry is expected to be present in physiological systems (Chialvo and Millonas, Phys. Rev. Lett. **209**:26–30, 1995) as it is the fundamental property of a non-equilibrium system (Prigogine and Antoniou, Ann. N. U. Acad. Sci. **879**:8–28, 2007). Furthermore, asymmetry is linked with the time irreversibility, which is reported as highest in systems with healthy physiology (Costa et al., Phys. Rev. Lett. **95**:1–4, 2005; Costa et al., Phys. Rev. Lett. **89**:062102, 2002). Thus, asymmetry represents the presence of complex nonlinear dynamics in physiological signals. So far, very little work has been published in defining and measuring asymmetry in physiological signals (Piskorski and Guzik, Phys. Rev. Lett. **28**:287–300, 2007).

5.1 Introduction

Physiological systems are inherently complex and subject to energy, entropy and information fluxes across their boundaries. These systems function in disequilibrium in healthy condition and their self-organizing capability is related to asymmetricity of the underlying processes [149]. In pathological perturbations, a loss of self-organizing capability associated with aging or disease is a function of loss of asymmetricity [149]. Intuitively, asymmetry refers to the lack of symmetry; in other words, the distribution of signals is imbalanced. This imbalance or dissimilarity can easily be observed in geometry of the phase space plots. Asymmetry is expected

A.H. Khandoker et al., *Poincaré Plot Methods for Heart Rate Variability Analysis*,
DOI 10.1007/978-1-4614-7375-6_5,

to be present in physiological systems [150] as it is the fundamental property of a non-equilibrium system [151]. Furthermore, asymmetry is linked with the time irreversibility, which is reported as highest in systems with healthy physiology [149, 152]. Thus, asymmetry represents the presence of complex nonlinear dynamics in physiological signals. So far, very little work has been published in defining and measuring asymmetry in physiological signals [153].

Heart rate variability (HRV), the variation of the time period between consecutive heartbeats, is thought to reflect the heart's adaptability to the changing physiological conditions. HRV is a net effect of extrinsic regulation and intrinsic heart rhythm. It is however predominantly dependent on the extrinsic regulation of the heart rate [114]. The autonomic nervous system [sympathetic (SNS) and parasympathetic (PNS)] plays a major role in regulating heart rate. Sympathetic activity is responsible for increasing the heart rate while the parasympathetic activity lowers the heart rate. Both of them work concurrently to control the heart rate in a given range. In practice there is always some variability in heart rate, due to imbalances in the activity levels of SNS and PNS. Hence, any heart rate cannot increase or decrease indefinitely but instead will be followed by an opposite trend. However, it is unlikely that any increase or decrease in RR interval has a reversing effect on the very next RR interval. The speed at which the heart rate increases or decreases is variable, which implies that the periods of increasing or decreasing RR interval are also not equal. As a result, heart rate asymmetry (HRA) should be a common phenomena present in a healthy heart, which is also reported by Piskorski and Guzik [153] and Porta et al. [154] and the main focus of this chapter.

An obvious phenomenon in a typical Poincaré plot is asymmetry with respect to the line of identity (line with 45° slope and passes through the origin). Porta et al. have examined the asymmetry of Poincaré plot and shown the interrelationship between time reversibility, pattern asymmetry and nonlinear dynamics [154]. While doing so, the authors have used three different indices, Guzik's index (*GI*), Porta's index (*PI*) and Ehlers' index (*EI*) [155–157]. Guzik et al. [156] analysed the asymmetry of short-segment HRV signal (5 min) and extended to long segment (30 min) [153]. It has been reported that about 80 % of healthy subjects showed HRA. Since asymmetry is a phenomenon of a healthy physiological system [149, 152], it is concluded that in a resting situation, the healthy heart should always exhibit the asymmetry.

5.2 Existing Indices of HRA

The traditional asymmetry indices used in previous studies are *GI*, *PI* and *EI* [154–157] . For defining all the indices, let us assume that the increasing cloud I and decreasing cloud D are a set of points as shown below, respectively:

$$I \equiv \bigcup_{i=1}^{M} P_i(RR_i, RR_{i+1})$$

and

$$D \equiv \bigcup_{i=1}^{K} P_i(RR_i, RR_{i+1}),$$

where M and K represent the number of points in increasing and decreasing cloud.

5.2.1 Guzik's Index

Guzik et al. have defined the index for measuring the HRA using the Poincaré plot [156]. For defining GI, the distance of the plotted points from the line of identity is used. For ith point $P_i(RR_i, RR_{i+1})$ of the plot, the distance can be calculated as

$$D_i = \frac{|\, RR_i - RR_{i+1} \,|}{\sqrt{2}}$$

P_i^+ represents the point above the line of identity ($RR_i < RR_{i+1}$) and the distance D_i is denoted as D_i^+, whereas P_i^- is the point below the line of identity, i.e. $RR_i < RR_{i+1}$, and the distance is denoted by D_i^-. Guzik's index (GI) is defined as

$$GI = \frac{\sum_{i=1}^{C(P_i^+)} (D_i^+)^2}{\sum_{i=1}^{N-1} (D_i)^2} \times 100\,\%, \tag{5.1}$$

where $C(P_i^+)$ gives the number of points above the line of identity. In the new definition of asymmetry, the line of identity is not used for grouping the plotted points into two different clouds. As a result, it is not possible to calculate the new GI using Eq. 5.1. The set of points $\{P_i^+\}$ used in Eq. 5.1 is equivalent to the increasing cloud defined in the new definition of asymmetry. Hence, using the increasing cloud I, Eq. 5.1 can be redefined using the proposed definition:

$$GI_p = \frac{\sum_{i=1}^{M} (D_i)^2}{\sum_{i=1}^{N-1} (D_i)^2} \times 100\,\%, \tag{5.2}$$

where the numerator corresponds to the increasing cloud, the denominator corresponds to the total number of points and GI_p is the redefined Guzik's index.

5.2.2 Porta's Index

Porta et al. have also defined the asymmetry with respect to the line of identity [155]. Rather than considering the relative distance of the points with respect to the line of identity, the authors have assessed asymmetry by evaluating the number of points

below the line of identity with respect to the overall number of points not on the line of identity. Hence, *PI* is defined as

$$PI = \frac{C(P_i^-)}{C(P_i^+) + C(P_i^-)} \times 100\,\%. \tag{5.3}$$

According to the proposed definition, the set of points P_i^- is equivalent to the set of points belonging to the decreasing cloud *D*. Hence, Eq. 5.3 can be redefined as:

$$PI_p = \frac{K}{M+K} \times 100\,\%, \tag{5.4}$$

where *K* and *M* are the number of points in cloud *D* and *I*, respectively.

5.2.3 Ehlers' Index

Ehler et al. have used the first derivative of the RR interval series for assessing asymmetry of the given distribution [157]. Skewness is measured over the first derivative signal to estimate the asymmetry of the distribution. Hence, for RR interval time series, it can be defined as

$$EI = \frac{\sum_{i=1}^{N-1} (RR_i - RR_{i+1})^3}{(\sum_{i=1}^{N-1} (RR_i - RR_{i+1})^2)^{\frac{3}{2}}}. \tag{5.5}$$

Ehlers' index (*EI*) can be redefined with the proposed definition splitting into positive and negative cloud as

$$EI_p = \frac{\sum_{i=1}^{M} (\Delta I_i)^3 + \sum_{i=1}^{K} (\Delta D_i)^3}{(\sum_{i=1}^{N-1} (RR_i - RR_{i+1})^2)^{\frac{3}{2}}}, \tag{5.6}$$

where

$$\Delta I_i = RR_{i+1} - RR_i, P_i(RR_i, RR_{i+1}) \in I$$

and

$$\Delta D_i = RR_i - RR_{i+1}, P_i(RR_i, RR_{i+1}) \in D.$$

Normalization of Indices

For the sake of comparison, normalization of the indices to a convenient scale is recommended. Both *GI* and *PI* values range between 0 and 100, with the index value of symmetry $S = 50$. Asymmetricity of the signal is ranked based on the difference

of the index value from S. Index value > 50 represents that the distribution is positively skewed, either by the magnitude or by the number of points, whereas index value < 50 corresponds to the reverse distribution. The symmetricity in EI ($EI \in [-1, 1]$) is characterized as $S = 0$ and values > 0 or < 0 rank the asymmetricity of the signal. Therefore, to compare EI with GI and PI, it is necessary to use a normalized scale for the index value calculated. In this study, we have defined a range, R, for the index values to define asymmetricity. The range is defined as 1% of the difference between minimum and maximum index values, where *index* is either GI, PI or EI. Now, if $index \in (S \pm R)$ then the signal is symmetric, otherwise asymmetric. The redefined indices (GI_p, PI_p and EI_p) are also normalized in the same manner.

5.3 New Definition of Asymmetry in RR Interval Time Series

The line of identity in Poincaré plot is defined as the line that passes through the origin at an angle of 45° with *x-axis*. Therefore, any point $P(x, y)$ on the line of identity can be expressed as $x = y$. Brennan et al. have defined the line of identity and shown that *SD1* is the standard deviation perpendicular to the line of identity and *SD2* is the standard deviation of plotted points along the line of identity [112]. But the mathematical formulation given for *SD1* and *SD2* by Brennan et al. [112] does not comply with the concept of line of identity which is shown by Piskorski and Guzik [153]. Piskorski and Guzik have also shown that the line of identity defined by Brennan et al. [112] is a line, which actually passes through the moment of inertia or centroid of the plotted data points with slope of 45° [153]. The authors have named that line as $l1$ and showed the difference in calculation of *SD1* and *SD2* with respect to the line of identity and $l1$ (Fig. 5.1). The standard descriptors calculated with respect to the line of identity and $l1$ show negligible difference. As the line of identity has a special criteria $x = y$, Piskorski et al. suggested that the line of identity will be the best option for measuring *SD1* and *SD2*. In our work, we have followed Piskorski and Guzik [153] in defining the line of identity.

The asymmetry indices GI and PI are defined based on the asymmetry definition by Piskorski and Guzik [153]. On the other hand, EI does not depend on any specific definition of asymmetry. It is directly calculated from the time-series information by computing skewness of the first derivative of the signal, i.e. the points of the Poincaré plot are not necessarily divided into two groups (increasing and decreasing). The details for calculating all indices are given in Sect. 5.4. In [153], asymmetry is defined with respect to the line of identity. All points on the line of identity ($x = y$) have equal consecutive RR intervals. Hence, any point above the line of identity corresponds to increasing RR interval (i.e. decreasing heart rate) and any point below corresponds to decreasing RR interval (i.e. increasing heart rate). Based on this, asymmetry is defined and quantified using different indices. Moreover, this HRA can visually be observed as the clouds of points above and below the line of identity. In healthy condition, the heart shows continuous short-term variability

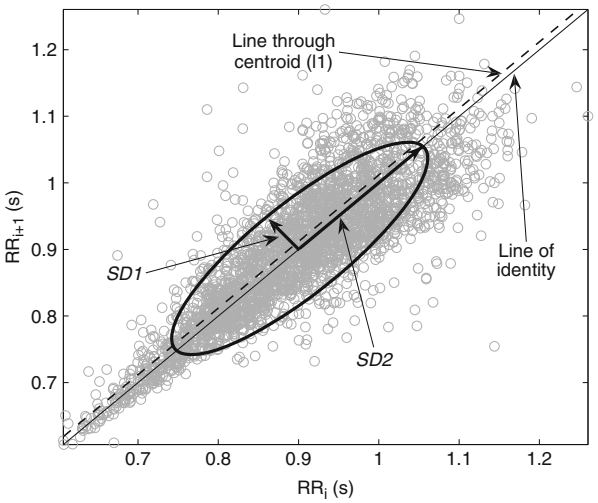

Fig. 5.1 A standard Poincaré plot of RR intervals of a healthy person ($N = 3000$). The line of identity (*solid line*) and line through centroid, $l1$, (*dashed line*) are also shown. Figure adapted from Karmakar et al. [165]

owing to SNS and PNS activities, which impacts on the formation of cloud around the line of identity. However, this definition of asymmetry does not represent true increasing or decreasing pattern in the heart rate. To overcome this problem, we have defined the asymmetry of heart rate in Poincaré plot independent of the line of identity, i.e. decision about a point whether it is increasing or decreasing is not made based on its position with respect to line of identity on the 2D Poincaré map. In the proposed definition, the cloud of points is partitioned into three parts: (1) points belonging to the increasing pattern of RR interval (I); (2) points belonging to the decreasing pattern of RR interval (D); and (3) points belonging to the stable pattern in RR interval (N). The decision about a point as to whether it belongs to one of the above three classes is made based on the neighbouring point in the Poincaré plot. Therefore, the analysis corresponds to at least three consecutive RR intervals of the RR interval time series for *lag-1* Poincaré plot. Let the vector $\mathbf{RR}$ be defined as $\mathbf{RR} \equiv \{RR_1, RR_2, RR_3, \ldots, RR_N\}$ where RR_i is the ith RR interval and N is the total number of RR intervals. Furthermore, let $\mathbf{P}$, the set of all points in a *lag-1* Poincaré plot, be defined as $\mathbf{P} \equiv \bigcup_{i=1}^{N-1} P_i(RR_i, RR_{i+1})$.

For any two points $P_i(RR_i, RR_{i+1})$ and $P_{i+1}(RR_{i+1}, RR_{i+2})$ of the Poincaré plot, which involves three RR intervals $\{RR_i, RR_{i+1}, RR_{i+2}\}$, the status of the point P_{i+1} with respect to clouds of points is defined as:

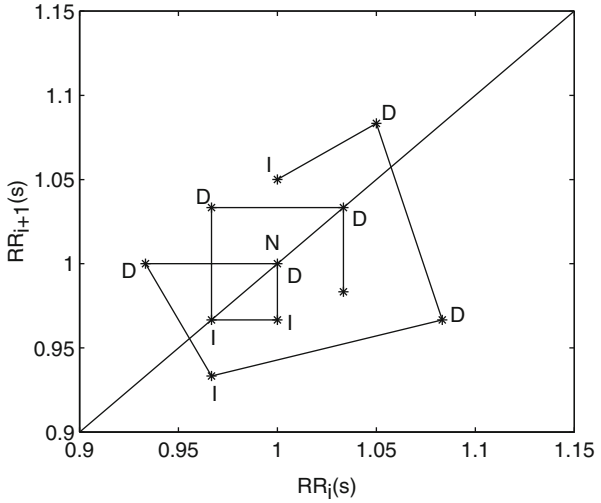

Fig. 5.2 Poincaré plot points marked with cloud initials *I*, *D* and *N*, which indicates that the point belongs to increasing, decreasing and stable cloud, respectively. Figure adapted from Karmakar et al. [165]

$$
\begin{aligned}
P_i \in I: \; & (RR_i < RR_{i+1} \bigwedge RR_{i+1} < RR_{i+2}) \bigvee \\
& (RR_i \geq RR_{i+1} \bigwedge RR_{i+1} < RR_{i+2}) \bigvee \\
& (RR_i > RR_{i+1} \bigwedge RR_{i+1} \leq RR_{i+2}) \\
\in D: \; & (RR_i > RR_{i+1} \bigwedge RR_{i+1} > RR_{i+2}) \bigvee \\
& (RR_i \leq RR_{i+1} \bigwedge RR_{i+1} > RR_{i+2}) \bigvee \\
& (RR_i < RR_{i+1} \bigwedge RR_{i+1} \geq RR_{i+2}) \\
\in N: \; & RR_i = RR_{i+1} = RR_{i+2}.
\end{aligned} \tag{5.7}
$$

After defining the clouds, the asymmetry is defined between the points of *I* and *D*, i.e. the asymmetry is defined as the lack of symmetry among the distribution of points in *I* and *D*. Hence, any point belonging to cloud *N* is not considered for calculating asymmetry. According to this definition, it is possible to find points *I* or *D* on both sides of the line of identity as shown in Fig. 5.2. Examples of the proposed definition with the RR intervals series shown in Fig. 5.2 are given in Fig. 5.3.

5.4 Modified HRA Indices Using Poincaré Plot

In this section, the asymmetry indices are redefined in accordance with the proposed definition of asymmetry. For redefining all the indices, let us assume that the increasing cloud *I* and decreasing cloud *D* are a set of points as shown below, respectively:

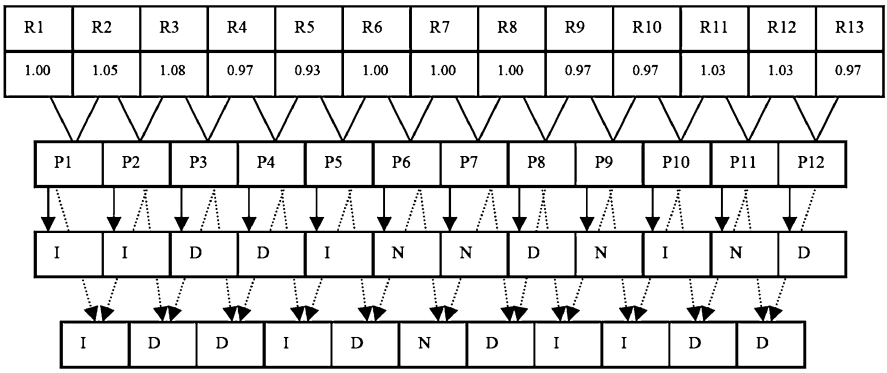

Fig. 5.3 RR interval time series of length N (= 13). The cloud type (I, D or N) corresponds to the point $\{P_i(RR_i, RR_{i+1})\}$ for Guzik's definition and point $\{P_i(RR_i, RR_{i+1}), P_{i+1}(RR_{i+1},RR_{i+2})\}$ for the new definition. Figure adapted from Karmakar et al. [165]

$$I \equiv \bigcup_{i=1}^{M} P_i(RR_i, RR_{i+1})$$

and

$$D \equiv \bigcup_{i=1}^{K} P_i(RR_i, RR_{i+1}),$$

where M and K represent the number of points in increasing and decreasing cloud.

5.4.1 *Guzik's Index (GI_p)*

In the new definition of asymmetry, the line of identity is not used for grouping the plotted points into two different clouds. As a result, it is not possible to calculate the new GI using Eq. 5.1. The set of points $\{P_i^+\}$ used in Eq. 5.1 is equivalent to the increasing cloud defined in the new definition of asymmetry. Hence, using the increasing cloud I, Eq. 5.1 can be redefined using the proposed definition:

$$GI_p = \frac{\sum_{i=1}^{M} (D_i)^2}{\sum_{i=1}^{N-1} (D_i)^2} \times 100\,\%, \tag{5.8}$$

where the numerator corresponds to the increasing cloud, the denominator corresponds to the total number of points and GI_p is the redefined Guzik's index.

5.4.2 Porta's Index (PI_p)

According to the proposed definition, the set of points P_i^- is equivalent to the set of points belonging to the decreasing cloud D. Hence, Eq. 5.3 can be redefined as

$$PI_p = \frac{K}{M+K} \times 100\,\% \tag{5.9}$$

where K and M are the number of points in cloud D and I, respectively.

5.4.3 Ehlers' Index (EI_p)

Ehlers' index (EI) can be redefined with the proposed definition splitting into positive and negative cloud as

$$EI_p = \frac{\sum_{i=1}^{M} (\Delta I_i)^3 + \sum_{i=1}^{K} (\Delta D_i)^3}{(\sum_{i=1}^{N-1} (RR_i - RR_{i+1})^2)^{\frac{3}{2}}}, \tag{5.10}$$

where,

$$\Delta I_i = RR_{i+1} - RR_i, P_i(RR_i, RR_{i+1}) \in I$$

and

$$\Delta D_i = RR_i - RR_{i+1}, P_i(RR_i, RR_{i+1}) \in D.$$

5.5 Application of HRA in Clinical Research

5.5.1 Presence of HRA in Healthy Subjects

One important hypothesis about the HRA is that in resting condition a healthy heart should exhibit asymmetricity. In this section we have tested this hypothesis using both existing and redefined HRA indices.

5.5.1.1 Data and Results

In order to validate the new definition of asymmetry, GI, PI and EI using Guzik's definition and GI_p, PI_p and EI_p using the proposed definition of asymmetry are calculated for RR interval data of short segment (5 min) and long segment (30 min)

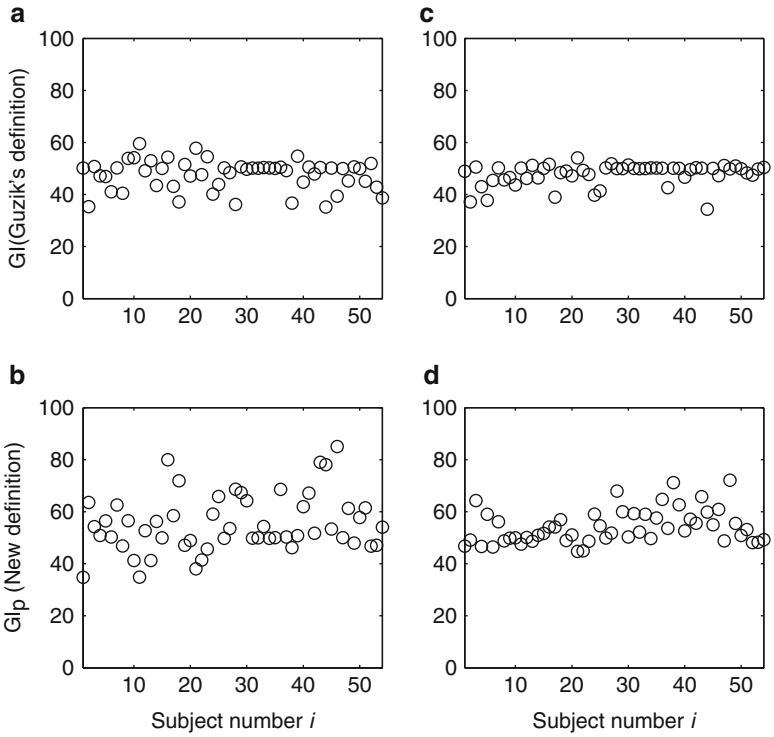

Fig. 5.4 Guzik's index (*GI*) of asymmetry for short-segment (5 min, panels a and b) and long-segment (30 min, panels c and d) RR interval signal of normal sinus rhythm subjects ($n = 54$). *Top panel* (**a** and **c**) shows the *GI* (see Eq. 5.1) values using Guzik's asymmetry definition and *bottom panel* (**b** and **d**) shows GI_p (see Eq. 5.8) values using proposed asymmetry definition. Figure adapted from Karmakar et al. [165]

which belongs to short-term HRV analysis [55]. The data from MIT-BIH Physionet database are used in this analysis [145]. RR intervals of 54 subjects with normal sinus rhythm (30 men, aged 28.5–76, and 24 women, aged 58–73) have been used from the Physionet Normal Sinus Rhythm database [145] for evaluating the proposed definition. Hence we had 54 sets of recordings, of which the first 5 and 30 min were used for short- and long-segment analysis, respectively. The original long term ECG recordings were digitized at 128 Hz, and the beat annotations were obtained by automated analysis with manual review and correction [145]. The short- and long-segment RR interval series were taken from the beginning of each subject's RR interval, but the time of the day or night cannot be mentioned as it was not clearly stated in the Physionet database. Details about the RR interval time series can be found in [158].

The *GI* values for short-segment (panels a and b) and long-segment (panel, c and d) RR interval time series are shown in Fig. 5.4. Top panel (a and c) of Fig. 5.4 represents the *GI* values. For short segment, 61.11 % of the subjects are found to be

asymmetric, $GI \in (49,51)$, with GI values 52.37 ± 5.72 (mean $\pm$ sd). Furthermore, 53.74 % of the subjects are found to be asymmetric, $GI \in (49,51)$, with GI values 52.18 ± 4.13 for long-segment study. The presence of asymmetry using Guzik's definition is not consistent and the reason for this is reported as unknown [156]. The GI_p values for both short- and long-segment RR interval signals are shown in the bottom panel (b and d) of Fig. 5.4. In the short-segment case, the GI_p values range within 44.72 ± 11.12 and 79.63 % of the subjects are found to be asymmetric. In addition, 81.48 % of subjects showed asymmetry for long-segment signal with GI_p values 45.81 ± 6.56. This shows significant improvement in consistency of GI_p for defining asymmetry using proposed definition in contrast to Guzik's asymmetry definition.

In Fig. 5.5, PI and PI_p values for short-segment (panel a and b) and long segment (panels c and d) RR interval time series are shown. Top panel (a and c) represents the PI values, whereas the bottom panel (b and d) shows PI_p values. For short-segment signal 61.11 % subjects showed asymmetry, $PI \notin (49,51)$, with PI values 50.11 ± 2.63, whereas 53.70 % of subjects showed asymmetry, $PI_p \notin (49,51)$, with PI_p values 49.94 ± 2.12 in accordance to the proposed definition. In case of long-segment variability, 40.74 % of subjects showed asymmetry with PI values 50.65 ± 1.94. On the other hand, 31.48 % of subjects showed asymmetry with PI_p values 50.27 ± 1.47.

Figure 5.6 shows the values of asymmetry index EI; 50 % of the subjects with EI values 0.0290 ± 0.0711 are found asymmetric in case of short-segment signal with Guzik's definition of asymmetry. On the other hand, 94.44 % of the subjects are screened asymmetric using the proposed definition with EI_p values -0.1979 ± 0.2344. Similarly, for long-segment signal, 20.37 % subjects are found asymmetric with EI values 0.0145 ± 0.0331 using Guzik's definition. However, 85.19 % subjects are screened asymmetric with EI_p values -0.1909 ± 0.2053. Table 5.1 shows mean and standard deviations of values of all indices, and asymmetry subjects (%) for both short- and long-segment signals are given.

5.5.1.2 Discussion

Asymmetry is related with nonlinear dynamics and time irreversibility, which exhibit the most complex interrelationships [149, 152]. It is reported to be highest for healthy physiological systems under resting conditions [149] and decreases with pathology, thus providing a marker for any loss of normal functionality. Guzik et al. [156] have reported that the asymmetry in HRV might be related to the response of the baroreflex to increase or decrease the blood pressure [159]. However, exact reason for such asymmetry is largely unknown.

In this study, a novel way for defining asymmetry of RR interval time series in Poincaré plot has been presented. Two merits of the novel definition are: (1) It is correctly defined from geometrical point of view because it considers pattern rather than a single point of the Poincaré plot to categorize a point either as increasing, decreasing or stable; (2) It captures HRA of healthy subjects using existing

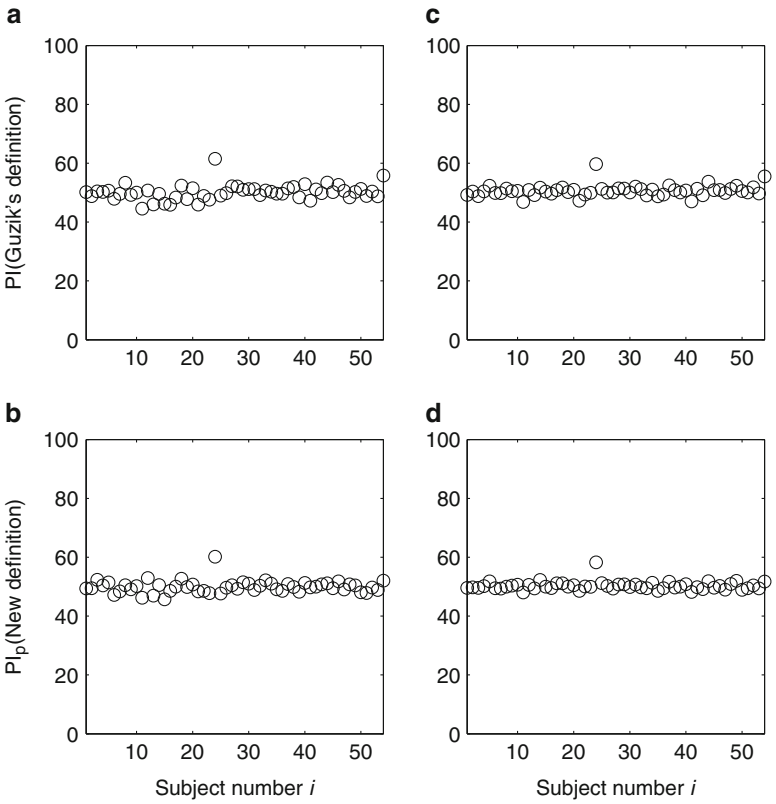

Fig. 5.5 Porta's index (*PI*) of asymmetry for short segment (5 min, panel a and b) and long segment (30 min, panel c and d) RR interval signal of normal sinus rhythm subjects ($n = 54$). *Top panel* (**a** and **c**) shows the *PI* (see Eq. 5.3) values using Guzik's asymmetry definition and *bottom panel* (**b** and **d**) shows PI_p (see Eq. 5.9) values using new asymmetry definition. Figure adapted from Karmakar et al. [165]

asymmetry indices at higher prevalence than that defined by Guzik et al. [156]. Though Guzik's definition of asymmetry is very simple and intuitive, using such a definition may not be physiologically correct. For instance, it is known that HRV signal of normal resting subjects should be asymmetric as reported by Piskorski and Guzik [153] and Costa et al. [149]. In our study, using Guzik's definition, only 62% of such subjects showed asymmetry, whereas the new definition showed asymmetry in more than 94 % of the subjects. Also, the regulation of heart rate in resting subjects is not instantaneous but takes a couple of seconds [159]. In such a case, it is important to measure the pattern of changes in heart rate rather than instantaneous effect. Therefore, the consideration of instantaneous changes could be a major limitation of the existing definition. As a result, use of patterns in the proposed definition, rather than instantaneous changes, reveals much higher incidence of asymmetry in healthy subjects.

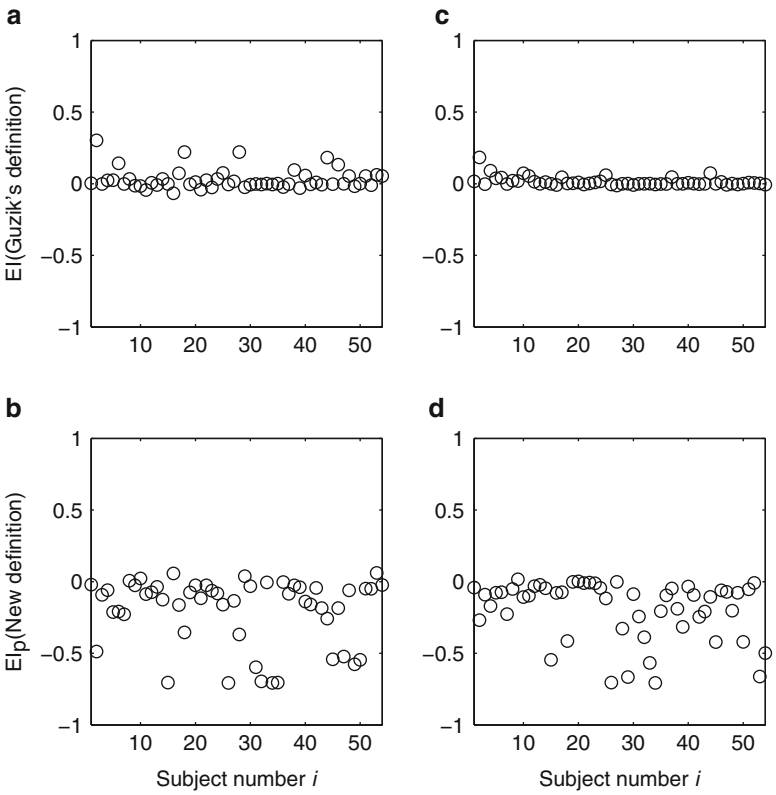

Fig. 5.6 Ehlers' index (*EI*) of asymmetry for short-segment (5 min, panels a and b) and long segment (30 min, panels c and d) RR interval signal of normal sinus rhythm subjects ($n = 54$). *Top panel* (**a** and **c**) shows the *EI* (see Eq. 5.5) values using Guzik's asymmetry definition and *bottom panel* (**b** and **d**) shows EI_p (see Eq. 5.10) values using new asymmetry definition. Figure adapted from Karmakar et al. [165]

Table 5.1 Mean and standard deviation (SD) of Guzik's index (*GI*), Porta's index (*PI*) and Ehlers' index (*EI*) for 5 and 30 min signal of subjects, $n = 54$, with normal sinus rhythm

Index	Length (min)	Guzik's definition		New definition	
		Mean ± SD	Asymmetry (%)	Mean ± SD	Asymmetry (%)
Guzik's index	5	47.63 ± 5.72	61.11	55.28 ± 11.12	79.63
	30	47.82 ± 4.13	53.74	54.19 ± 6.56	81.48
Porta's index	5	50.11 ± 2.63	61.11	49.94 ± 2.12	53.70
	30	50.65 ± 1.94	40.74	50.27 ± 1.47	31.48
Ehlers' index	5	0.0290 ± 0.0711	50.00	−0.1979 ± 0.2344	94.44
	30	0.0145 ± 0.0331	20.37	−0.1909 ± 0.2053	85.19

Subjects (%) found to be asymmetric using both definition for all indices are also given

This analysis exploits the physiological phenomena of the system to define the asymmetry in the signal. Important findings of this study are: (a) Existing asymmetry indices are more sensitive to capture asymmetricity with the proposed definition of asymmetry than the existing definition (Figs. 5.4–5.6, Table 5.1). (b) *GI* and *EI* capture the asymmetricity better than the *PI*; i.e. for both definitions, use of location of points in the 2D map with respect to the line of identity for calculating the indices performs better than using only the information about the number of points in the distribution (Figs. 5.4–5.6, Table 5.1). Furthermore, the asymmetricity has been calculated for subjects with normal sinus rhythm using both definitions. The results are in accordance with the reported asymmetry in HRV [149, 154–156]. In this analysis, we have found that 79.63 % and 81.48 % of subjects are shown to be asymmetric using the proposed definition compared to 61.11 % and 53.74 % of subjects with Guzik's definition for short-segment and long-segment signals, respectively (Fig. 5.4).

However, other than the definition of HRA, the index calculated by Piskorski and Guzik [153] and Porta et al. [154] was also different than the way we have calculated in this study. We have used the bidirectional and normalization criteria (as discussed in Sect. 5.2.3) to compare among different indices popularly used for asymmetry measurement. Moreover, if we used the same asymmetry measure as used by Piskorski and Guzik [153], then it would be 48.15 % and 40.74 % for short and long segment, respectively, in our results. Hence, use of bidirectional criteria for defining asymmetry has increased the prevalence of having asymmetry. However, the intention of using bidirectional criterion has been supported by the time reversibility or asymmetry theory. In reference to the result published by Piskorski and Guzik [153], the 81 % or 82 % subjects showing asymmetry can not be comparable to this study as the data set used in their study was different. In this study, only 61.11 % and 53.74 % of subjects were showing asymmetry using Guzik's definition with bidirectional and normalization criteria for short and long segment, respectively.

Using Guzik's definition and Porta's index (*PI*), 61.11 % of the subjects are classified as having asymmetry in case of short-segment signal and 40.74 % in the case of long-segment signal, in contrast to the findings reported in [155]. However, using the new definition, PI_p was reduced to 53.70 % and 31.48 % for short-segment and long-segment signals, respectively. The reason behind the reduced performance of PI_p against *PI* is the difference of the number of points used for calculating the index. If we observe the two definitions closely, there is hardly any difference in the number of points in the increasing and decreasing clouds. Hence similar numbers were expected. The use of the number of points has been shown by Porta et al. to work well in certain conditions like foetal heart rate monitoring [155]. In this study, we did not find any specific advantage with Porta's index. This justification is strongly supported by the result obtained using EI_p, which showed 94.44 % and 85.19 % of subjects having asymmetry for both short-segment and long-segment signals, using the new definition. In contrast, 50.00 % and 20.37 % of subjects are found to be asymmetric using Guzik's definition for the short-segment and long-segment signals, respectively. Therefore, we confirm that our definition performs better in quantifying asymmetry using existing indices than the previous ones.

Piskorski and Guzik [153] performed surrogate analysis to show that HRA is related to some unknown underlying dynamics rather than a random behaviour and showed that the presence of asymmetry or the time reversibility is abolished in randomized HRV signal. Piskorski and Guzik [153] used random shuffling surrogate method, in which the signals were randomly shuffled so that the probability of distribution remained the same but the temporal correlations were destroyed [160, 161]. However, nonlinear measurement is not necessarily be affected by such surrogation [162]. The discrimination, by any measure either linear or nonlinear, of the original time series from this type of surrogation only suggests the presence of hidden correlation in the original time series. Therefore, we conclude that the effect of surrogation does not have a specific impact on nonlinear properties like asymmetry or time reversibility. However, it has impact on asymmetricity measured with respect to line of identity, because the correlation of the signal changes with surrogation and it affects the distribution of points in Poincaré plot around the line of identity. Therefore, results of surrogate analysis have no affect on this proposed definition.

5.5.2 Correlation Between HRA and Parasympathetic Activity

In this section we assess the changes in HRA in experimental conditions using Poincaré plot during parasympathetic blockade (atropine infusion) and parasympathetic enhancement (scopolamine administration). The correlations between HRA and the frequency-domain parameters are also analysed to better explain the changes in HRA with respect to PNS activity.

5.5.2.1 Clinical Study Methodology

Eight subjects with normal sinus rhythm, non-smokers, without cardiovascular abnormalities and who were not taking any medications were studied. Subjects were aged between 20 and 40 years (30.5 ± 7.3).

All recordings were performed at the same time of the day without any disturbances. No respiration control was performed because all phases of the study were conducted in the resting state. An intravenous cannula was inserted into an antecubital vein and subjects then rested 20 min before recording of data. The length of the study varies from 10 to 20 min. For autonomic perturbations the following sequence of protocol was performed. At least 20 min was allowed between each phase to permit the heart rate to return to baseline. Details of the study design and data collection are reported by Kamen et al. [94] and the sequence of phases was maintained strictly as follows:

Baseline Study

All baseline studies were conducted in subjects in the post-absorptive state after resting for 10 min in the supine position.

Atropine Infusion

Atropine sulphate (1.2 mg) was added to 50 ml intravenous dextrose and infused at a rate of 0.12 mg/min for 5 min and then at a rate of 0.24 mg/min until completion of this phase of study. Use of this dose regimen reduces PNS activity significantly [138]. After 10 min of infusion of atropine, the data collection started.

Transdermal Scopolamine

One week after the above studies, a low-dose transdermal scopolamine patch (hyoscine 1.5 mg) was applied overnight to an undamaged hair-free area of the skin behind the ear. The patch remained in situ for the duration of this period of study. It has been shown in [139] that low-dose transdermal scopolamine increases PNS activity.

5.5.2.2 Deviation from Symmetry $Dist_{\text{sym}}$

Deviation of the asymmetry index (GI_p) from symmetric range of the index is defined as $Dist_{\text{sym}}$. For ith subject $Dist_{\text{sym}}$ is calculated as

$$Dist_{\text{sym}} = |GI_p(i) - GI_p(\text{sym})|$$

where $GI_p(\text{sym})$ is the index value for symmetric range and defined as

$$\begin{aligned} GI_p(\text{sym}) &= 49, \quad GI_p(i) < 49 \\ GI_p(\text{sym}) &= 51, \quad GI_p(i) > 51 \\ GI_p(\text{sym}) &= GI_p, \quad \text{otherwise} \end{aligned}$$

Finally, $Dist_{\text{sym}} = 0$ indicates the absence of HRA, whereas $Dist_{\text{sym}} > 0$ indicates presence of HRA.

5.5.2.3 Power Spectral Analysis

The HRV time series was generated as a function of heartbeats and the resulting interval tachogram is thus a series of RR intervals plotted as a function of the interval number. In this study we have used the MATLAB R2009b implementation of Welch's method for calculating power spectrum density (PSD). In this method the

data are zero-padded to length of the FFT and divided into overlapping segments. The PSD of each segment is computed and the PSD estimates are averaged out, which is the result of the power spectral analysis. This averaging decreases the variance of the estimate relative to a single periodogram estimate of the entire data record [163]. We have used FFT length of 128 data points which is divided into eight segments with 50 % overlap between them. The resultant PSD vector length is 65 which also represents the number of frequency bin. The resolution of each bin is 1/128 (i.e. 0.0078 cycles/interval). In order to express the result in true frequency domain (Hz), the spectral units are then divided by the mean RR interval as discussed in [94].

5.5.2.4 Statistics

MATLAB statistics toolbox was used to perform a Spearman nonparametric correlation coefficient [164] analysis between frequency-domain features (LF, HF and LF/HF) and HRA index GI_p. The coefficient is signified by R (rho), and can take on the values from -1.0 to 1.0, where -1.0 is a perfect negative (inverse) correlation, 0.0 is no correlation and 1.0 is a perfect positive correlation.

5.5.2.5 Results from HRA Analysis

RR intervals and corresponding Poincaré plots of all three phases of studies are shown in Fig. 5.7. Results of power spectral analysis of HRV signal of all subjects for all phases of study are summarized in Table 5.2. Subjects displayed a marked reduction both in low-frequency power (0.04–0.15 Hz) and high-frequency (> 0.15 Hz) power during atropine infusion. In contrast, *LF/HF* (ratio between low-frequency and high-frequency power) increased significantly during this phase. Moreover, only 5 out of 8 subjects are found to be asymmetric which is lower than the total number of subjects (7 out of 8) found asymmetric during baseline phase. On the other hand, all eight subjects are screened asymmetric during scopolamine phase.

The HRA index values of all subjects for all three phases of the study are plotted in Fig. 5.8. The dotted lines represent the range of HRA index value that is considered symmetric. In this analysis, we have used the HRA index value $49 \leq GI_p \leq 51$ as symmetric as suggested in our previous study [165]. The HRA index GI_p during atropine infusion phase shows that 3 out of 8 subjects lie inside the symmetric range (panel a, Fig. 5.8). On the other hand, GI_p value of only 1 out of 8 subject lies inside the symmetric range in baseline phase (panel b, Fig. 5.8). It is interesting to discover that all subjects lie outside the symmetric range in scopolamine administration phase (panel c, Fig. 5.8). This indicates that the HRA reduces in the subjects during atropine infusion, whereas it increases in scopolamine administration.

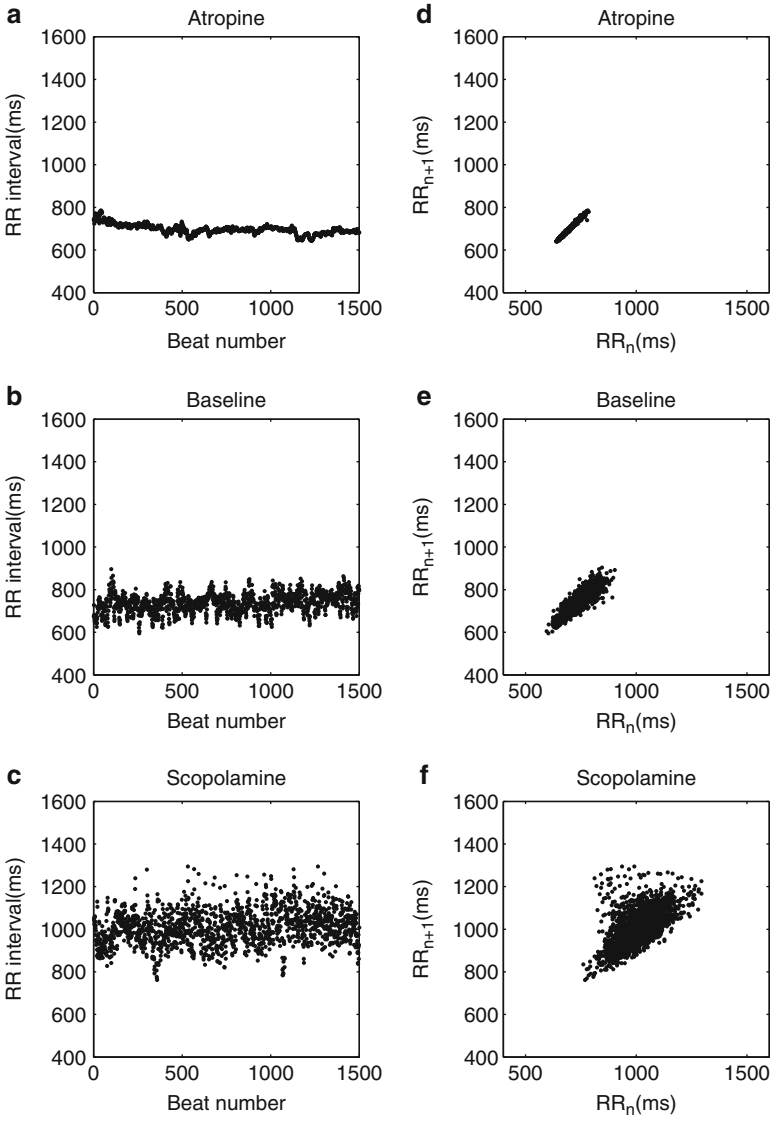

Fig. 5.7 RR interval time series for single subject from all three phases of study with corresponding Poincaré plot

The effect of parasympathetic activity on HRA can be also measured as deviation of HRA index (GI_p) values from symmetricity, $Dist_{\text{sym}}$, is shown in Fig. 5.9. In the atropine infusion phase 5 out of 8 subjects were found asymmetric with lowest $mean(Dist_{\text{sym}})Atro$ value as depicted using solid line among all phases. In scopolamine administration phase all 8 subjects (out of 8) were found asymmetric with the

Table 5.2 HRV parameters from subjects exposed to parasympathetic perturbations

Feature	Atropine (mean ± SD)	Baseline (mean ± SD)	Scopolamine (mean ± SD)
LF (ms^2)	704.10 ± 94.00	1095.93 ± 224.71	1286.39 ± 207.70
HF (ms^2)	34.22 ± 13.36	253.38 ± 252.71	503.39 ± 286.94
LF/HF	22.20 ± 5.00	7.43 ± 4.02	3.43 ± 2.02
No. of asymmetric subjects (out of 8)	5	7	8

All values are presented as (mean ± standard deviation)
Abbreviations: *LF* low-frequency power, *HF* high-frequency power, *LF/HF* ratio between low-frequency and high-frequency power, *Asymmetry* percentage of subjects screened asymmetric

highest $mean(Dist_{\text{sym}})Scop$ value as depicted using dash-dot line among all phases, whereas at baseline 7 out of 8 subjects found asymmetric with a $mean(Dist_{\text{sym}})Base$ higher than $mean(Dist_{\text{sym}})Atro$ and lower than $mean(Dist_{\text{sym}})Scop$.

The correlation between frequency-domain parameters and asymmetry is shown in Table 5.3 and Fig. 5.10. Top panels a, b and c of Fig. 5.10 shows the correlation of GI_p with LF, HF and LF/HF during atropine infusion phase. Accounting for intersubject variation, the overall measure has shown a significantly strong negative correlation of GI_p with LF ($R = -0.76, p = 0.037$) and stronger with HF ($R = -0.95, p = 0.001$) (Fig. 5.10a, b). LF/HF also demonstrated significant positive correlation ($R = 0.83, p = 0.015$) with GI_p (Fig. 5.10c). In the baseline phase only LF/HF demonstrated (Fig. 5.10f) significant negative correlation with GI_p having ($R = -0.76, p = 0.037$); however, the correlation coefficient of LF and HF with GI_p was positive but insignificant with $R = 0.67, p = 0.083$ and $R = 0.69$, $p = 0.069$, respectively. In the scopolamine administration phase, LF and HF also demonstrated (Fig. 5.10g, h) positive correlation with GI_p; however, those relations were not significant, $R = 0.42$, $p = 0.296$ and $R = 0.61$, $p = 0.111$, respectively. However, LF/HF demonstrated a nearly significant negative correlation ($R = -0.69, p = 0.066$) with GI_p (Fig. 5.10i).

5.5.2.6 Discussion

HRV data have been analysed using both frequency-domain and time-domain techniques. Quantitative Poincaré plot analysis was used to assess the changes in HRV during parasympathetic blockade [111] and compared the results with power spectral analysis of HRV, which was the commonly used method in the measurement of sympathovagal interaction [13, 103, 111, 140]. The potential use of Poincaré plot to measure HRA has also been explored by Karmakar et al. [165], Porta et al. [154] and Guzik et al. [156]. In this chapter, we have shown that HRA correlates with the changes with parasympathetic activity. In addition, we compared the changes in HRA due to change in parasympathetic activity with results of power spectral analysis.

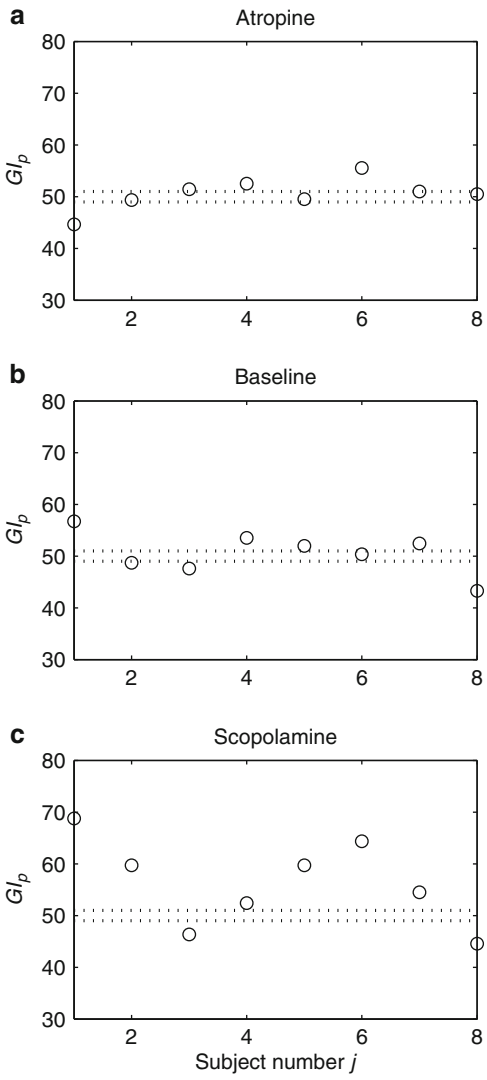

Fig. 5.8 Asymmetry index, GI_p values of HRV signal for all three phases of the study. *Dotted line* represents the symmetric range, i.e. any index values falling in this range indicate that the Poincaré plot of the subject is symmetric. Panels: (**a**) GI_P values of atropine infusion phase; (**b**) GI_P values of baseline phase; (**c**) GI_P values of scopolamine administration phase

Asymmetry is related with nonlinear dynamics and time irreversibility, which exhibit the most complex inter-relationships [149, 152]. It is reported to be highest for healthy subjects under resting conditions [149, 156] and decreases with pathology, thus providing a marker for any loss of normal functionality. Previous studies [156, 159] reported that the asymmetry in HRV may be related to the baroreflex to increase or decrease the blood pressure. However, exact reason for such asymmetry is largely unknown and therefore more information is required on the dynamics of HRV. In this chapter, we have shown that the changes in HRA correlate with

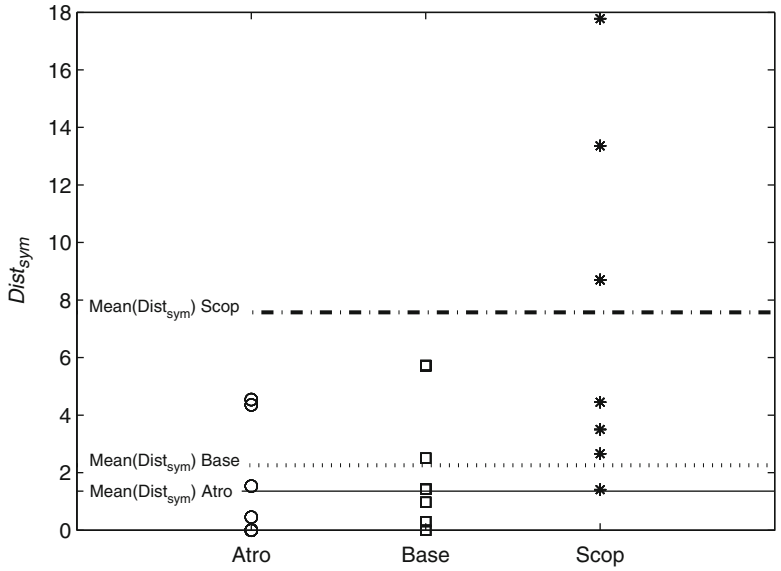

Fig. 5.9 Distance of HRA index (GI_p) from the symmetric range for atropine infusion, baseline and scopolamine administration phase. Mean distance of all subjects for each phase is shown using *solid line* (atropine), *dashed line* (baseline) and *dash-dot line* (scopolamine)

Table 5.3 Spearman correlation coefficient (R) and significance (p) of GI_p with LF, HF and LF/HF for parasympathetic perturbations

GI_p \ Phase		Atropine	Baseline	Scopolamine
LF	R	−0.76	0.67	0.42
	p	0.037*	0.083	0.296
HF	R	−0.95	0.69	0.61
	p	0.001**	0.069	0.111
LF/HF	R	0.83	−0.76	−0.69
	p	0.015*	0.037*	0.066

Statistical significance: $^*p < 0.05$; $^{**}p < 0.01$

parasympathetic activity in healthy subjects which is the first time it has been shown to our knowledge.

Subjects displayed a marked reduction in high-frequency power during atropine infusion. Similarly, the HRA index value (GI_p) also closest to the symmetric region, measured as the deviation from symmetricity (Fig. 5.9) compared to baseline phase, indicates that changes in parasympathetic activity affect the presence of HRA as well as deviation of HRA index values (GI_p) from symmetricity. Moreover, these results are also supported by the significant correlation of HF with GI_p in atropine infusion phase (Fig. 5.10b and Table 5.3). However, the insignificant relation between HF and GI_p might be due to the small number of subjects.

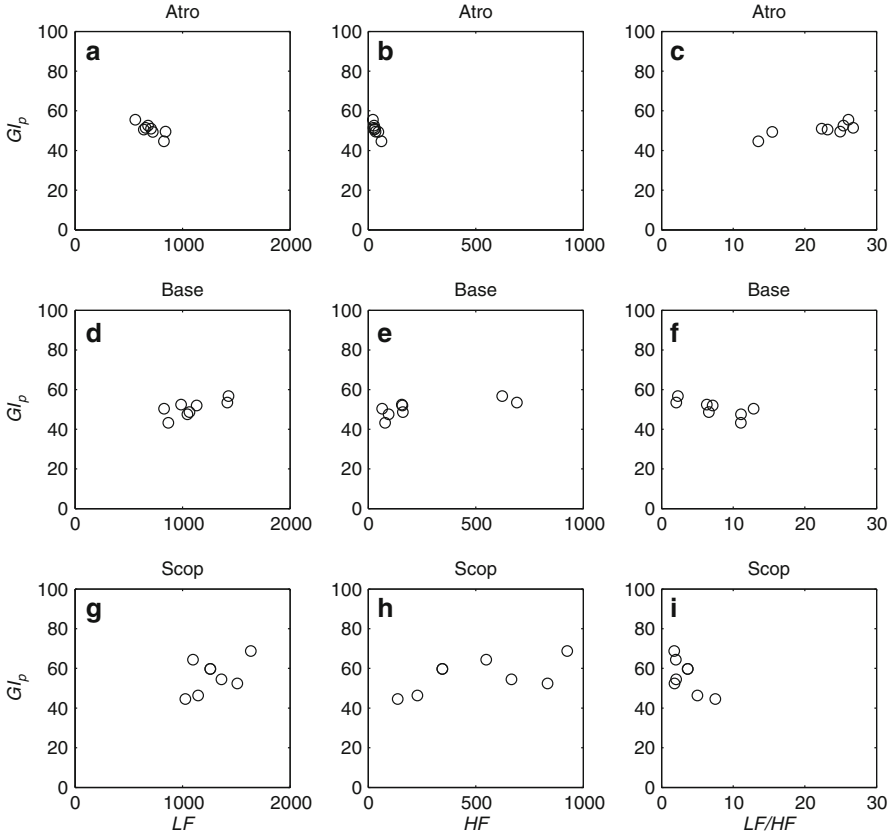

Fig. 5.10 Correlation between frequency-domain parameters (*LF* low-frequency power, *HF* high-frequency power, and LF/HF their ratio) with asymmetry index (GI_p). *Top panel* (**a**), (**b**) and (**c**) shows the correlation of GI_p with LF, HF and LF/HF during atropine infusion. *Middle panel* (**d**), (**e**) and (**f**) shows the correlation of GI_p with LF, HF and LF/HF during baseline condition. *Bottom panel* (**g**), (**h**) and (**i**) shows the correlation of GI_p with LF, HF and LF/HF during scopolamine administration

The low-dose scopolamine may decrease heart rate by a paradoxical vagomimetic effect [139]. Delivery of scopolamine by transdermal patch substantially increases both baseline and reflexly augmented levels of cardiac parasympathetic activity over 24 h in normal subjects [143, 144]. HF increased to a greater extent during administration of scopolamine (Table 5.2), which is consistent with an increase in PNS activity [139]. This increase in parasympathetic activity increases screened HRA subject number to 8 out of 8 as compared to 7 out of 8 in baseline phase which indicates that HRA reflects an effective change in parasympathetic activity. In addition, although intersubject variation can be noticed in GI_p values, the HRA index value (GI_p) moves further from the symmetric region (Fig. 5.9) compared

to the baseline phase. However, correlation of HF with GI_p was found to be insignificant during scopolamine administration phase which could be due to the low number of subjects.

Instantaneous changes in RR intervals (short-term variability) are mediated by vagal efferent activity, because vagal effects on the sinus node are known to develop faster than sympathetically mediated effects [101,124]. As a result, atropine infusion reduces the short-term variability in HRV signal which reduces the HF as shown in this study as well as reported by Kamen et al. [94] and Tulppo et al. [111]. In contrast, scopolamine increases the short-term variability which is reflected as increase in HF as compared to baseline. Since the detection of HRA implies the presence of nonlinear dynamics [155], our results support presence of nonlinear short-term heart period variability in a significant percentage of healthy young humans in baseline phase [149, 154, 156, 165–167] which reduces with atropine infusion and increases with scopolamine administration.

LF/HF ratio depends on changes in both low-frequency and high-frequency powers. In our study, we found a strong and significant correlation of GI_p with LF/HF both in atropine infusion and baseline phases of experiment. Although strongly criticized, the ratio of LF/HF is believed to be an indirect index of (or at least to be related to) the sympathovagal balance [55,116,168,169]. The correlations found in the present study suggest that HRA is related to both LF and HF (Table 5.3) to some extent and which is strongly reflected with LF/HF in all phases.

5.6 Conclusion

The redefinition of asymmetry in Poincaré plot provides an improvement in analysing asymmetricity of physiological time-series signal. The three asymmetry indices Guzik's index, Porta's index and Ehlers', index which are used to represent asymmetry have been redefined according to the new definition. The indices GI_p and EI_p have been shown to perform better in detecting asymmetry in heart rate series of normal healthy subjects with a slight reduction in performance using PI_p with the new definition. The experiment described here has resulted in relatively better performance compared to the existing definition.

In addition, we have observed that atropine infusion and scopolamine administration result in changes in HRA. The HRA index (GI_p) values are significantly correlated with changes in high-frequency power in both atropine infusion and baseline phases. This study provides an insight about the physiological link between HRA and parasympathetic activity; however further studies with larger population and relation with sympathetic activity may provide a complete physiological explanation of HRA with respect to sympathovagal activity.

Although the concept of HRA is not new, the modified definition has shown superior performance in detecting HRA in healthy humans during rest. However, the exact physiological reason behind HRA is yet to be revealed. To better understand the physiological relevance of HRA, in the next chapter, the correlation of HRA with changes in PNS activity is examined.

Chapter 6
Segmented Poincaré Plot Analysis and Lagged Segmented Poincaré Plot Analysis

Abstract Traditional Poincaré plot analysis (PPA) represents a two-dimensional graphical and quantitative representation of a time series dynamics. However, traditional PPA indices measure mainly linear aspects of the heart rate variability (HRV).

Therefore, we introduced a new method of PPA - the segmented Poincaré plot analysis (SPPA) that retains essential nonlinear characteristics of the HRV and other time series.

Additional insights into the underlying physiological mechanisms have been gained by extending the methodology of SPPA. Thus we developed the lagged SPPA (LSPPA) that investigates time correlations of the BBI.

For the first time we could demonstrate that an HRV index from SPPA was able to contribute to risk stratification in patients suffering from DCM. LSPPA provides a prognostic preview for DCM patients regarding several associated symptoms such as endothelial dysfunctions and increased risk stratification in DCM to 92% accuracy.

SPPA was also applied to BBI time series and blood pressure signals to investigate the coupling between those two time series.

In several studies we could demonstrate that the applications of SPPA and LSPPA lead to much more information about impaired autonomic regulation and have the potential to be applied in much more fields of medical diagnosis and risk stratification.

6.1 Introduction

Traditional Poincaré plot analysis (PPA) [59,87,89,91] represents a two-dimensional graphical and quantitative representation of a time series dynamics. Babloyantz and Destexhe [170] were the first to introduce this nonlinear method for heart rate variability (HRV) analysis including both the pseudo-phase space and phase space quantification methods. Two-dimensional pseudo-phase space plots represent

A.H. Khandoker et al., *Poincaré Plot Methods for Heart Rate Variability Analysis*,
DOI 10.1007/978-1-4614-7375-6_6,

univariate system behaviour investigating signal values (NN_{n+1}) as a function of their previous ones (NN_n), whereas phase space plots represent multivariate system behaviour investigating interactions of at least two different signals.

Typically the following indices from PPA are calculated: short-term (*SD1*) and long-term (*SD2*) fluctuations of the investigated system and the ratio $SD1/SD2$ [87, 89]. An ellipse can be drawn into the plot along the line of identity whereas the centre represents the mean value of the time series and the axes are *SD1* and *SD2*. Even PPA is a nonlinear method where these indices appear insensitive to the nonlinear characteristics of the beat-to-beat intervals (BBI) [112].

Previous studies of patients suffering from dilated cardiomyopathy (DCM) have not evaluated the contribution of traditional PPA in risk stratification for sudden death [171, 172]. One reason for this is that these PPA indices measure mainly linear aspects of the BBI. Therefore, we recently introduced an enhanced method of PPA—the segmented Poincaré plot analysis (SPPA) [173] that retains essential nonlinear characteristics of the HRV time series. SPPA is characterized by a rotated and segmented Poincaré plot into a grid of 12×12 rectangles based on the centre of the cloud of points. Each rectangle is adapted to the *SD1* (height) and *SD2* (width).

In this chapter the ability of SPPA to differentiate between linear, nonlinear and Gaussian noise-caused dependencies is first tested by simulating and analysing such BBI time series. Then, surrogate analysis is performed to prove the ability of SPPA to obtain nonlinear behaviour in time series. Further, we represent a first study to investigate high- and low-risk patients suffering from DCM which subsequently use an extended SPPA method to investigate the Poincaré plot in a more detailed way by dividing the plot into 24×24 rectangles (adapted to *SD1*/2 and *SD2*/2) as well as into 48×48 rectangles (adapted to *SD1*/4 and *SD2*/4). Following this, SPPA will be performed to investigate age dependencies in healthy subjects.

The next step will be to apply SPPA to other cardiovascular signals such as systolic blood pressure (SBP) and diastolic blood pressure (DBP) in pregnant women suffering from hypertensive pregnancy disorders such as chronic or gestational hypertension and pre-eclampsia.

Even if the SPPA increases risk stratification [173], it still provides less information about the physiological background of the impaired autonomous regulation. Therefore, the objective was to investigate if time correlations will provide such information. As a consequence, the Lagged SPPA (LSPPA) method was developed to provide high-resolution analysis particularly in the very low (VLF = 0.0033–0.04 Hz) and low-frequency (LF = 0.04–0.15 Hz) bands [174]. In contrast to the traditional linear methods of HRV analysis [172, 175] and to PPA (related to BBIs) [172] which did not contribute to risk stratification, indices from LSPPA enhance risk stratification and provide some additional insights into the underlying physiological mechanism of heart rate regulation which will be later discussed.

Finally, we will discuss newer studies as well as first concepts to further improve these kinds of analysis methods to open up new fields of application. In this context, we will investigate other bio-signals such as respiratory signals and enhance the analysis method by introducing the interaction analysis using two-dimensional

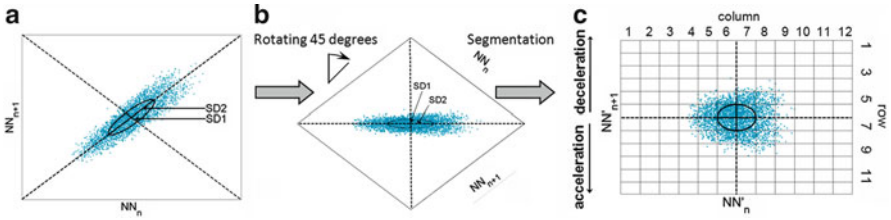

Fig. 6.1 The principle of SPPA; (**a**) traditional Poincaré plot, the calculation of *SD1* and *SD2*; (**b**) rotated Poincaré plot (45°); (**c**) a segmented Poincaré plot including SPPA indices

(2D SPPA) and three-dimensional (3D SPPA) approaches. This method improvement could lead to further enhanced information concerning alterations produced by coupled physiological systems.

6.2 Segmented Poincaré Plot Analysis

6.2.1 SPPA Method

The SPPA retains nonlinear features from a system based on PPA, representing an enhanced pseudo-phase space quantification method [173]. The Poincaré plots are two-dimensional graphical representations (as a cloud of points) of a time series plotted against its subsequent one. The calculation of PPA standard indices provides the basis for SPPA.

The SPPA method functions as follows:

1. The linear indices of *SD1* and *SD2* (Fig. 6.1a), representing short- and long-term fluctuations of the investigated system, are calculated according to traditional PPA (Eqs. 6.1–6.4), where Var is the variance, NN_n is a value of the time series with $n = 1,\ldots,N-1$ (N is the length of time series) and NN_{n+m} is the shifted version of the same time series shifted by a lag of $m = 1$ [89, 112, 176]:

$$N_n = (NN_1, NN_2, \ldots, NN_{N-1}) \tag{6.1}$$

$$NN_{n+1} = (NN_2, NN_3, \ldots, NN_N) \tag{6.2}$$

$$SD1 = \sqrt{\mathrm{VAR}\left(\frac{NN_n - NN_{n+1}}{\sqrt{2}}\right)} \tag{6.3}$$

$$SD2 = \sqrt{\mathrm{VAR}\left(\frac{NN_n + NN_{n+1}}{\sqrt{2}}\right)}. \tag{6.4}$$

2. The cloud of points presented by PPA is then rotated $\alpha = 45°$ around the main focus of the plot (Eq. 6.5), allowing for a simplified *SD1*/*SD2* adapted probability-estimating procedure (Fig. 6.1b), whereby z is the axis of rotation and $\overline{NN_n}$ and $\overline{NN_{n+1}}$ are the mean values of the original (NN_n) and shifted versions (NN_{n+1}) of a time series, respectively:

$$\begin{bmatrix} NN_n' \\ NN_{n+1}' \\ z' \end{bmatrix} = \begin{bmatrix} \overline{NN_n} \\ \overline{NN_{n+1}} \\ z \end{bmatrix} + \left(\begin{bmatrix} \cos\alpha & -\sin\alpha & 0 \\ \sin\alpha & \cos\alpha & 0 \\ 0 & 0 & 1 \end{bmatrix} \times \begin{bmatrix} NN_n - \overline{NN_n} \\ NN_{n+1} - \overline{NN_{n+1}} \\ z \end{bmatrix} \right). \tag{6.5}$$

3. Starting from the centre of the cloud of points, a grid of 12×12 rectangles (Fig. 6.1c) is drawn into the plot. The size of each rectangle is adapted to *SD1* (height) and *SD2* (width).
4. The number of points within each rectangle (M_{ij}) related to the total number of points (N) was counted to obtain the single probabilities (p_{ij}). Based on these probabilities, all row (i) and column (j) probabilities were calculated by summation of the related single probabilities (Eqs. 6.6 and 6.7):

$$p_{ri} = \sum_{j=1}^{12} p_{ij} \tag{6.6}$$

$$p_{cj} = \sum_{i=1}^{12} p_{ij}. \tag{6.7}$$

6.2.2 Applying SPPA on Simulated BBI Time Series

The ability of SPPA to discriminate between different system states can be demonstrated with simulated time series. To compare SPPA to PPA, different BBI time series were simulated that are characterized by similar values of PPA indices *SD1* and *SD1*. The four simulated time series were:

- S1: Noise
  Normal distributed white noise (Gaussian noise):

$$h(x) = \frac{1}{\sqrt{2\pi\delta^2}} * \mathrm{e}^{-\frac{(x-\Delta x)^2}{2*\delta^2}}. \tag{6.8}$$

- S2: Nonlinear signal
  Lorenz attractor:

$$\mathrm{d}x = (-\sigma x + \sigma y)\mathrm{d}t \tag{6.9}$$

$$\mathrm{d}y = (\rho x - y - xz) \tag{6.10}$$

$$\mathrm{d}z = (-\beta z + xy)\mathrm{d}t. \tag{6.11}$$

- S3: Linear/nonlinear noisy signal
  Three sinusoidal functions with Gaussian noise and Lorenz attractor:

$$x(t) = S1+S2+\sin(0.2*2*pi*t)+\sin(0.15*2*pi*t)+\sin(0.01*2*pi*t). \tag{6.12}$$

- S4: Linear surrogated noisy signal
  Three sinusoidal functions with Gaussian noise and the surrogated Lorenz attractor:

$$\begin{aligned} x(t) &= S1 + \text{surrogate}(S2) + \sin(0.2*2*pi*t) \\ &\quad + \sin(0.15*2*pi*t) + \sin(0.01*2*pi*t). \end{aligned} \tag{6.13}$$

Applying the amplitude adjusted Fourier transform (AAFT) algorithm introduced by Theiler et al. [160], we generated surrogate time series which have the amplitude distribution and the power spectrum of the original BBI time series. The idea of the AAFT algorithm is to first rescale the values in the original time series to make them Gaussian. Then the Fourier transform (FT) algorithm is used to create surrogate time series including the same Fourier spectrum as the rescaled data. Finally, the Gaussian surrogate is rescaled back to have the same amplitude distribution as the original time series. A significant difference between the nonlinear values for the original and the surrogate time series shows that SPPA can reliably distinguish linear from nonlinear time series (see also Sect. 6.2.3). Therefore, we compare S3 (as the original signal including nonlinearities) with S4 (the surrogated signal) where S4 differs from S3 only in the surrogated part of the Lorenz signal part (S2).

The simulated BBI time series (S1–S4) were generated for $t = 30$ min each with a sampling frequency of 1,000 Hz (Fig. 6.2). Physiological properties somewhat representing human HRV were simulated by including sinusoidal signals of the most prominent frequency bands HF (0.2 Hz), LF (0.15 Hz) and VLF (0.01 Hz) with regard to the coupled signals S3 and S4. Additionally, the amplitudes of the signals have been adjusted without suppressing any dependencies within the coupled signals and ensuring similar linear indices calculated by traditional PPA as much as possible.

In relation to the totalized value of amplitudes concerning all simulated BBI time series (S1–S4), we generated percentage amplitudes, respectively (Gaussian noise (S1, S3, S4): 4%; Lorenz attractor (S2–S4): 70%; sinusoidal functions (S3, S4): 14%).

Validating the defined dependencies within the simulated BBI time series, we applied the auto correlation function (ACF), which investigates linear dependencies, and the auto mutual information function (AMIF), which investigates linear and nonlinear dependencies in the simulated BBI time series (see Fig. 6.3). The concept of mutual information is based on an assessment of information flow I, defined by means of a probability distribution p [177–179] in the case of a discrete random number.

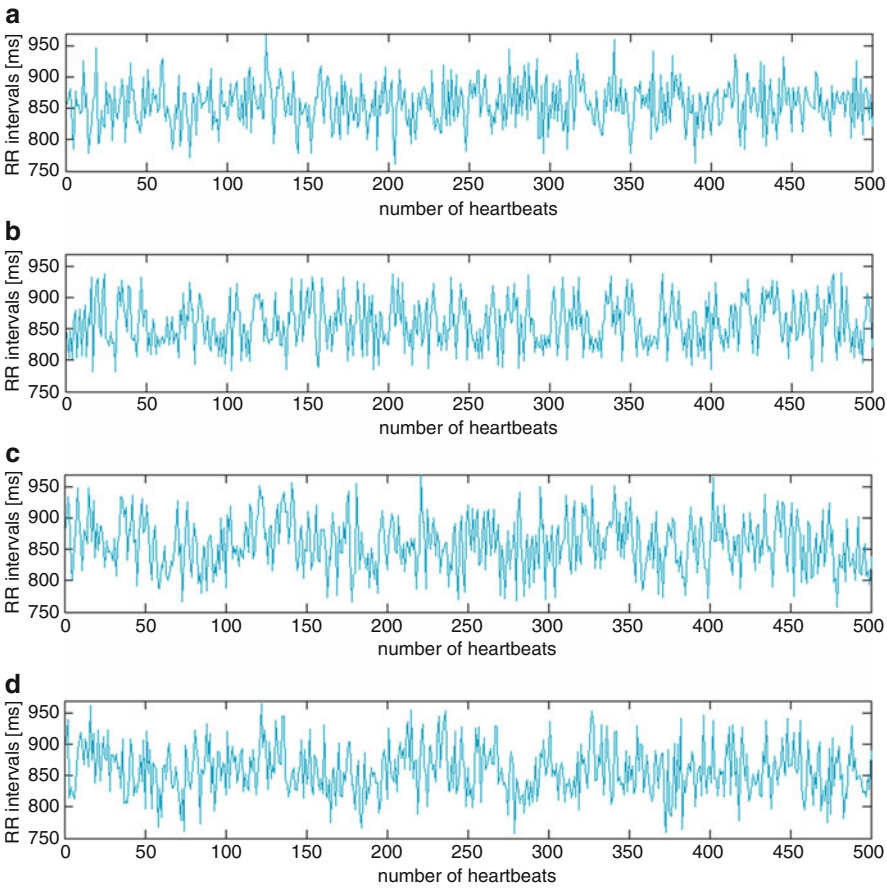

Fig. 6.2 Simulated BBI time series: (**a**) S1: Gaussian noise; (**b**) S2: Lorenz attractor; (**c**) S3: linear/nonlinear noisy signal including three sinusoidal functions (0.2 Hz, 0.15 Hz and 0.01 Hz) with Gaussian noise and Lorenz attractor; (**d**) S4: linear surrogated noisy signal including three sinus functions (0.2 Hz, 0.15 Hz and 0.01 Hz) with Gaussian noise and the surrogated Lorenz attractor

In Gaussian noise, both functions are almost zero for each τ except for $\tau = 0$ (S1—Fig. 6.3a). In case of pure nonlinearity (S2—Fig. 6.3b) and the nonlinear coupled time series (S3—Fig. 6.3c), significant nonlinear dependencies in the AMIF which are too wide peaks at $\tau = 0$ can been shown. The arrows in Fig. 6.3c, d (S4) show the difference between the coupled time series. While the nonlinear part (Lorenz attractor) within S3 causes a wide peak, S4 does not exhibit this peak because of the destroyed nonlinear structures within the surrogated Lorenz attractor. In ACF a few linear dependencies can be shown in which S3 and S4 are coupled with three sinus functions.

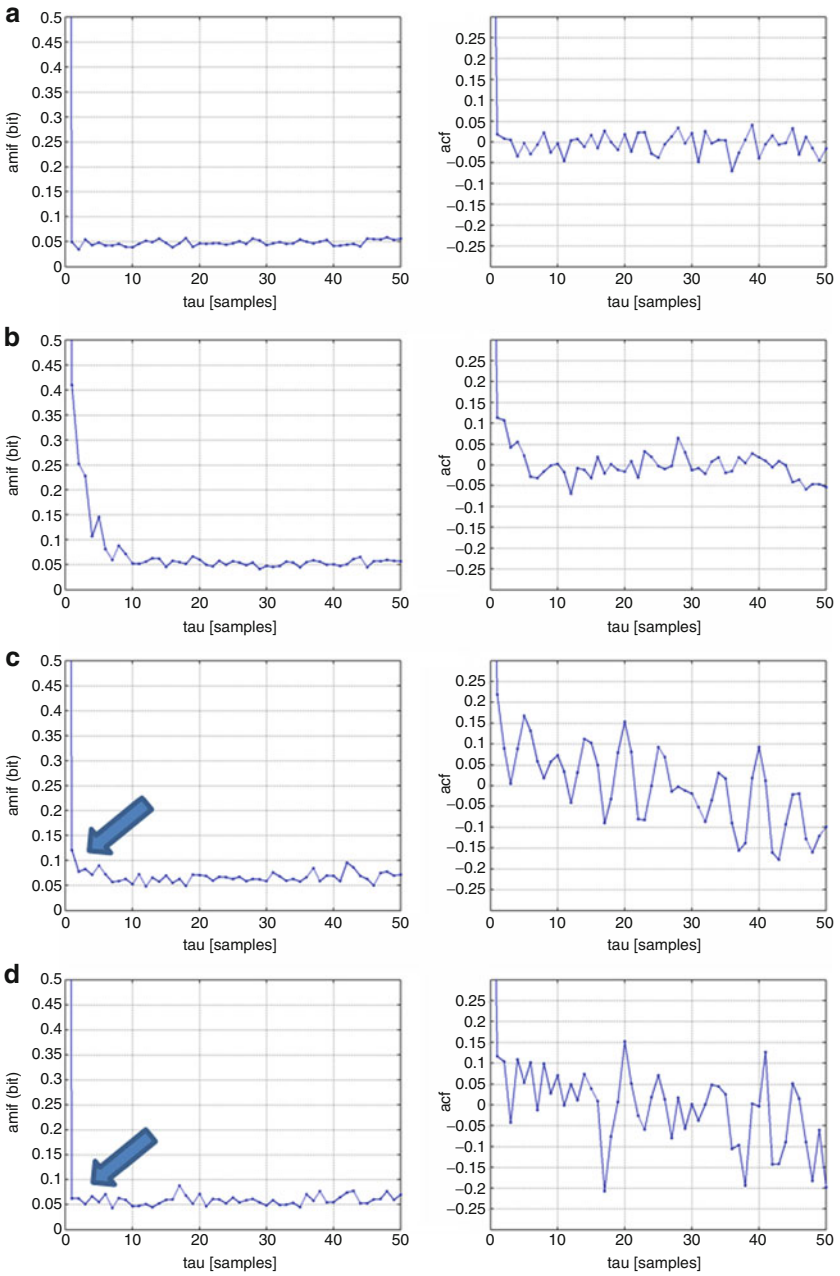

Fig. 6.3 Results of AMIF (*left*) and ACF (*right*) applying simulated BBI time series, respectively: (**a**) S1: Gaussian noise; (**b**) S2: Lorenz attractor; (**c**) S3: linear/ nonlinear noisy signal including three sinusoidal functions (0.2 Hz, 0.15 Hz and 0.01 Hz) with Gaussian noise and Lorenz attractor; (**d**) S4: linear surrogated noisy signal including three sinus functions (0.2 Hz, 0.15 Hz and 0.01 Hz) with Gaussian noise and the surrogated Lorenz attractor; the arrow highlights the different behaviour of the (surrogated) Lorenz attractor

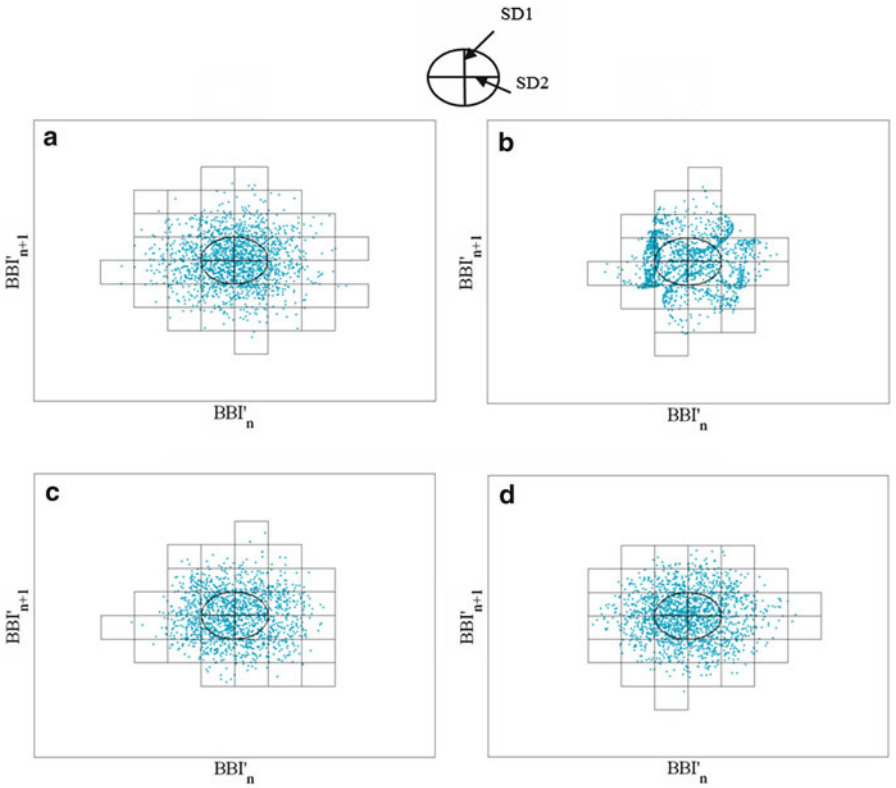

Fig. 6.4 SPPA plots applying simulated BBI time series: (**a**) S1: Gaussian noise; (**b**) S2: Lorenz attractor; (**c**) S3: linear/nonlinear noisy signal including three sinusoidal functions (0.2 Hz, 0.15 Hz and 0.01 Hz) with Gaussian noise and Lorenz attractor; (**d**) S4: linear surrogated noisy signal including three sinus functions (0.2 Hz, 0.15 Hz and 0.01 Hz) with Gaussian noise and the surrogated Lorenz attractor

The simulated BBI time series are presented in pseudo-phase space plots (Fig. 6.4), applying SPPA. This method provides a grid of 12×12 rectangles and a size adapted to *SD1* and *SD2* was applied (see also Sect. 6.2.1).

The shape of the cloud of points concerning Gaussian noise (S1—Fig. 6.4a) and nonlinear Lorenz attractor (S2—Fig. 6.4b) is typical for these dependencies. The coupled signals are barely distinguishable (S3—Fig. 6.4c and S4—Fig. 6.4d).

Differences in SPPA are shown in spite of similar linear PPA indices. Mean deviations of 0.14% (mean value of BBI), 6.21% (*SD1*), 14.95% (*SD2*) and 12.81% (*SD1*/*SD2*) were reached when applying traditional PPA.

In addition, we calculated the row and column probabilities of the simulated BBI time series by applying SPPA. With regard to column 6 and rows 5–8, we calculated lower mean deviations (2.76–6.73%) by applying SPPA as compared to the traditional PPA. However, there are considerably higher mean deviations with regard to columns 3–5 (19.20–73.32%) and 7–10 (16.85–66.67%) as well as row 3 (67.41%), 4 (19.38%), 9 (24.04%) and 10 (66.67%).

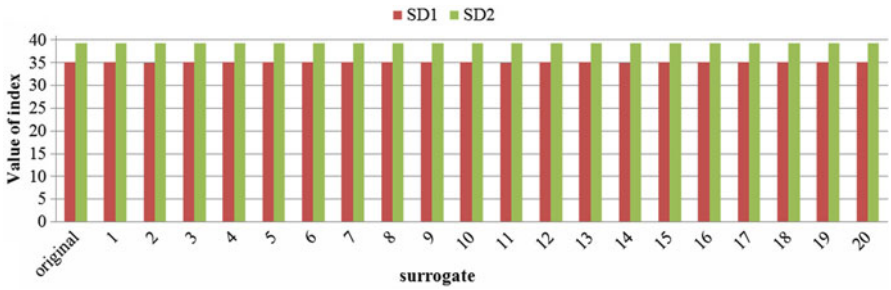

Fig. 6.5 Traditional linear PPA indices (*SD1* and *SD2*) applying the original nonlinear BBI time series (Lorenz attractor) and its 20 surrogated BBI time series each

To summarize, we could achieve considerably higher mean deviations by applying SPPA (2.76–73.32%) as compared to PPA (0.14–14.95%), confirming the assumption of SPPA to increase the differentiation between various dependencies such as Gaussian noise, nonlinearity and several coupled signals.

6.2.3 The Ability of SPPA to Obtain Nonlinear Behaviour in Time Series When Applying Surrogate Data Analysis

As previously mentioned in Sect. 6.2.2, surrogate data analysis techniques are applied, testing nonlinearity in time series by constructing surrogate data sets. Therefore, the AAFT algorithm described by Theiler et al. [160] is used to destroy nonlinear structures within time series while linear structures are maintained.

The aim of the following surrogate analysis is to test the ability of SPPA to obtain nonlinear structures represented in nonlinear BBI time series. In this study, 20 surrogate time series were generated by shuffling an original BBI time series.

The surrogate data analysis technique is applied for simulated nonlinear BBI time series (S2: Lorenz attractor—Sect. 6.2.2) consisting of three nonlinear parts (Eqs. 6.9–6.11). To illustrate the dependencies within the investigated BBI time series, the behaviour of two linear PPA indices (*SD1* and *SD2*—see Fig. 6.5) and one nonlinear SPPA index (fourth column—Fig. 6.6) are shown as an example. Thus, the figures represent the value of the original BBI time series compared to the values of the surrogated BBI time series, respectively.

It could be shown that linear indices (*SD1* and *SD2*) exhibit small deviations especially in relation to the value of the original BBI time series as compared to the nonlinear index (column 4), which presents significantly higher deviations.

Table 6.1 represents SPPA and traditional PPA indices by applying the original nonlinear BBI time series as well as the averaged one applying 20 surrogate BBI time series, whereas the most important indices are marked which significantly discriminate high- and low-risk DCM patients in a subsequent study applying the lagged segmented Poincaré plot analysis (LSPPA—see also Sect. 6.4.2).

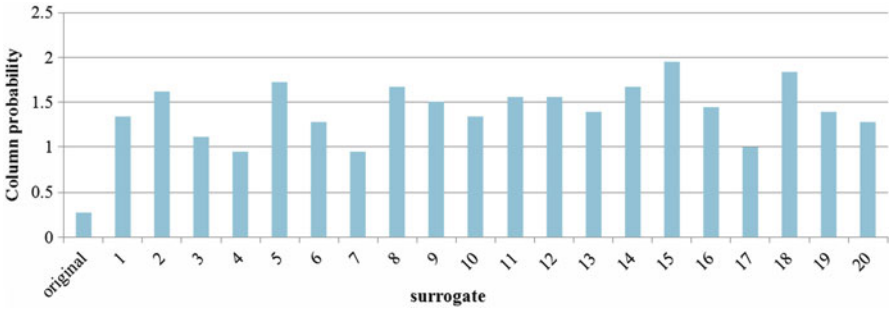

Fig. 6.6 Typical SPPA indices (column 4) applying the original nonlinear BBI time series (Lorenz attractor) and its 20 surrogated BBI time series

Table 6.1 Column and row occurrences applying the most important SPPA and PPA indices investigating the original simulated BBI time series (Lorenz attractor) and the averaged mean value of BBI and its standard deviation (SD), calculating 20 surrogated BBI time series; the difference in % specifies the deviation between the original index and its averaged surrogated BBI time series; significant LSPPA indices are marked

Method	Indices	Original	Surrogate Mean BBI	SD	Difference in %
SPPA	Column 3	0.0000	0.0000	0.0000	0.00
	Column 4	0.2781	1.3745	0.3421	79.77
	Column 5	19.4105	15.4535	0.5934	20.39
	Column 6	33.9822	34.1208	0.9934	0.41
	Column 7	25.5840	32.2259	1.2327	20.61
	Column 8	19.5217	14.0623	0.8743	27.97
	Column 9	1.2236	2.7462	0.4657	55.44
	Column 10	0.0000	0.0167	0.0408	100.00
	Row 3	0.1112	0.0083	0.0204	92.50
	Row 4	1.3904	2.1536	0.2075	35.44
	Row 5	14.9055	14.4713	0.6289	2.91
	Row 6	34.3715	33.3695	0.4916	2.92
	Row 7	32.9255	33.3528	0.4625	1.28
	Row 8	14.5718	14.4741	0.6482	0.67
	Row 9	1.6129	2.1619	0.2271	25.40
	Row 10	0.1112	0.0083	0.0204	92.50
PPA	Mean	857.7575	857.7144	0.0211	0.01
	SD1	35.0760	36.2740	1.1795	3.30
	SD2	39.3134	38.0830	1.0708	3.13
	SD1/*SD2*	0.8922	0.9540	0.0569	6.48

Calculating the deviations of surrogate BBI time series ($SD1 = 35.08 \pm 0.024$; $SD2 = 39.31 \pm 0.021$) and the original BBI time series ($SD1 = 35.07$; $SD2 = 39.31$), we obtained small ones when applying PPA (difference: 0.001–0.009%). In comparison, there are higher deviations (difference: 1.47–100%) when applying

Table 6.2 Classification of healthy subjects (REF) and DCM patients

	REF	DCM group	DCM_HR	DCM_LR
Number of subjects (male/female)	21 (12/9)	91 (70/21)	14 (11/3)	77 (59/18)
Age (year)	35 ± 13	55 ± 10	54 ± 11	56 ± 10
EF (%)	–	36 ± 12	31 ± 6	37 ± 12
NYHA (I-IV)	–	2.2 ± 0.8	2.6 ± 0.9	2.1 ± 0.8
LVEDD (mm)	–	63.5 ± 8	68.8 ± 10	62.5 ± 7

SPPA as seen by the representative example found in column 4 (original: 0.28; surrogate $= 1.43 \pm 0.28$; difference: 80.53%). In conclusion, we could confirm that indices from PPA represent linear dependencies, whereas SPPA indices obtain nonlinear dependencies representing considerable differences, as seen by the selected nonlinear structures.

6.2.4 Application of SPPA for Risk Stratification in Dilated Cardiomyopathy Patients

DCM is a chronic disease of the heart muscle characterized initially by a dilated left ventricle or dilation of both ventricles. This is attached to normal or reduced wall thickness and an impaired systolic function [180]. In the industrialized countries with aging populations, DCM is one of the most common public health problems (mortality of 5% per year) and occurs much more frequently (1,856,000 patients in the USA [181]) than other major forms of cardiomyopathy [182].

Various studies were performed to indicate risk stratification in patients with DCM. In former studies it was demonstrated that linear and nonlinear methods of HRV and baroreflex sensitivity (BRS) analysis could not considerably contribute to risk stratification in those patients [175, 183]. Therefore, the aim of this study is to analyse the suitability of SPPA to improve the risk stratification in DCM patients.

We enrolled 91 DCM patients (70 male and 21 female) and 21 references (healthy subjects; REF). The diagnosis of all DCM patients was confirmed by experienced cardiologists using coronary angiography and echocardiography (Table 6.2). From every patient a thirty-minute high-resolution ECG (orthogonal corrected Frank lead ECG, 22-bit resolution, 1,600 Hz sampling frequency) was recorded.

After a two-year follow-up, the DCM patients were divided into two groups: DCM without progression of the disease (low-risk, DCM_LR) and patients who died due to a cardiac event or were reanimated because of a life-threatening arrhythmic event (high-risk, DCM_HR). BBI were extracted using self-developed wavelet-based pattern recognition software [172]. The ECGs and the patients' data were stored in a database. A heart rate time series (tachogram) consisting of successive BBI were extracted from the ECG data. Applying an adaptive variance estimation algorithm, ectopic beats and artefacts were rejected and interpolated. These disturbances could considerably influence the PPA and, in particular, the SPPA [173, 183].

The nonparametric Mann-Whitney U-test was performed to determine the highly significant indices ($p < 0.01$) and the significant indices ($0.01 \leq p < 0.05$), differentiating between DCM patients and healthy subjects as well as between high-risk and low-risk DCM patients. The receiver operating characteristic (ROC) was computed univariate as well as multivariate, estimating the sensitivity for each value vs. the specificity. To validate a specific method, the performance of each index was assessed by estimating the area under the ROC curve (AUC).

Former studies of ECG could not improve risk stratification in patients suffering from DCM [171, 172]. The aim of this method is to prove the ability for both discrimination between DCM_HR and DCM_LR and between DCM and REF, as well as to perform basic testing for LSPPA. The results of the group tests applying SPPA are demonstrated in Table 6.3.

SPPA partly discriminates between the investigated groups. Highly significant indices of the group test between DCM patients and REF could be calculated as seen in columns 4 ($p = 0.0014$), 9 ($p = 0.0002$) and 10 ($p = 0.0007$) and in row 11 ($p = 0.0052$). One significant index (column 5: $p = 0.0241$) and one highly significant index (column 8: $p = 0.0005$) could be determined as risk predictors in DCM patients differentiating between DCM_HR and DCM_LR. Therefore, column 8 represents the highest AUC value of 80.0% with a sensitivity of 75.3% and a specificity of 71.4%.

The highest significant columns (columns 5 and 8) for risk stratification in DCM patients are shown in Fig. 6.7 and are exemplary for DCM_HR and DCM_LR patients, respectively.

The percentage of measuring points within the highly significant columns is higher in DCM_HR patients (column 5: mean $= 1.223 \pm 0.124$; column 8: mean $= 1.249 \pm 0.106$) than in DCM_LR patients (column 5: mean $= 0.990 \pm 0.214$; column 8: mean $= 1.021 \pm 0.167$). This means a higher dispersion of measuring points in patients with DCM_HR when compared to DCM_LR patients of DCM.

The highly significant columns (5 and 8) are located at a distance of *SD2* apart, the mean of both BBI_n (mean_BBI_n). In general, the borders of the highly significant columns can be described as follows:

- Column 5: from mean_$BBI_n - 2 * SD2$ to mean_$BBI_n - SD2$
- Column 8: from mean_$BBI_n + 2 * SD2$ to mean_$BBI_n + SD2$

The distance between the centre of the cloud of points and the significant columns of SPPA (columns 5 and 8) is equal in both directions (*SD2*). The significant columns are ranged very symmetrically around the centre of the cloud of points. Przibille et al. [184] were the first to study the influence of the standard deviation of all BBI (SDNN) within the Poincaré plots. Therefore, it could be shown that patients with an SDNN <50 ms died due to a cardiac event. They identified HRV analysis as being highly significant for DCM patients [184]. In our study, we found no significant differences in SDNN investigating high- and low-risk DCM patients, but highly differences discriminating between DCM patients and healthy subjects. These differences are caused probably due to the considerable limitations and the low number of enrolled patients in the compared study.

Table 6.3 Most significant SPPA indices discriminating DCM_HR vs. DCM_LR and DCM vs. REF including mean values and their SD in normalized row and column probabilities of occurrences; sensitivity (SENS), specificity (SPEC) and AUC (N.S. not significant; $*p < 0.05$; $**p < 0.01$)

	p (DCM_LR vs. DCM_HR)	p (DCM vs. REF)	Mean ± SD in % (DCM_HR)	Mean ± SD in % (DCM_LR)	Mean ± SD in % (REF)	SENS in %	SPEC in %	AUC in %
Column 4	N.S.	0.0014**	2.41 ± 1.10	2.12 ± 1.03	1.68 ± 0.63	81.0	63.7	72.4
Column 5	0.0241*	N.S.	12.01 ± 2.81	14.16 ± 2.93	13.12 ± 2.45	67.5	64.3	69.0
Column 8	0.0005**	N.S.	12.63 ± 2.10	14.42 ± 1.20	13.59 ± 2.42	75.3	71.4	80.0
Row 9	N.S.	0.0002**	1.76 ± 0.63	1.55 ± 0.71	1.14 ± 0.64	71.4	68.1	76.6
Row 10	N.S.	0.0007**	0.26 ± 0.18	0.23 ± 0.19	0.11 ± 0.14	76.2	67.0	73.9
Row 11	N.S.	0.0052**	0.06 ± 0.05	0.04 ± 0.06	0.01 ± 0.03	81.0	49.5	67.8

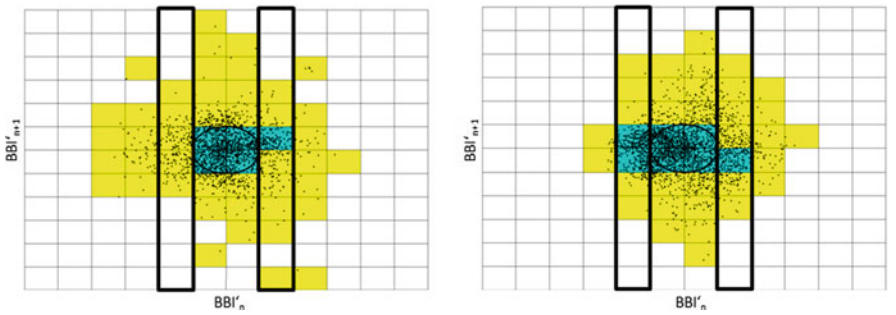

Fig. 6.7 Examples of SPPA plots applying DCM_HR (*left*) and DCM_LR (*right*) patients, respectively; *yellow marked rectangles* generally include measuring points and the *blue* ones exhibit a single probability of more than 5%; the most significant columns 5 and 8 are framed

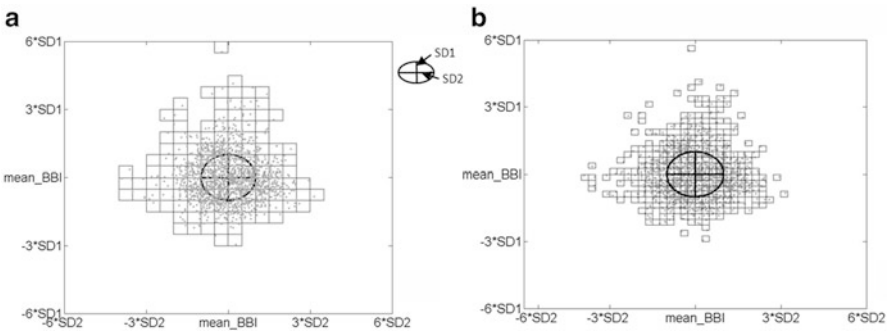

Fig. 6.8 Additional SPPA plots with different rectangle sizes; (**a**) test method I: $SD1/2$, $SD2/2$ and 24×24 rectangles; (**b**) test method II: $SD1/4$, $SD2/4$ and 48×48 rectangles

In conclusion, for the first time HRV indices from PPA were able to contribute to risk stratification (AUC value of 80.0%) in patients suffering from DCM. Further on, the SPPA retains nonlinear features, and therefore, overcomes limitations of traditional PPA.

6.2.5 *Investigating the Influence of Rectangle Size*

The standard SPPA method (see Sect. 6.2.1) fits a grid of 12×12 rectangles into the cloud of points where the size of the rectangles is adapted to the standard deviations *SD1* and *SD2*. Investigating the influence of the rectangles' size, we decreased the size of the rectangles by a half (*SD1*/2, *SD2*/2) or quarter (*SD1*/4, *SD2*/4), leading to an increased number of rectangles within the Poincaré plot.

In order to demonstrate SPPA's performance related to the varying rectangle sizes, we investigated DCM patients (idiopathic DCM) as introduced in Sect. 6.2.4.

Table 6.4 Significant indices applying test method I including the mean value and SD for the group test DCM_HR vs. DCM_LR (N.S. not significant; $*p < 0.05$; $**p < 0.01$)

Assigned column within standard SPPA		2	3	5	8
Related column (test method I)		4	5	10	16
DCM_HR	Mean (%)	0	0.0098	9.4527	4.8851
	SD	0	0.0380	2.2235	1.0513
DCM_LR	Mean (%)	0.0544	0.1058	8.0524	3.7057
	SD	0.1279	0.1656	2.1551	1.1818
p(DCM_HR vs. DCM_LR)		0.0336*	0.0071**	0.0441*	0.0008**

Test Method I

The size of the rectangles is adapted to $SD1/2$ and $SD2/2$, increasing the number of rectangles to 24×24 rectangles (Fig. 6.8a).

Table 6.4 presents significant columns of the BBI time series applying test method I. The coloured columns are located within the highly significant columns of standard SPPA. Therefore, column 10 (test method I: $p = 0.0441$) is located within column 5 (blue-coloured) and column 16 (test method I: $p = 0.0008$) in column 8 (red-coloured) of standard SPPA, as pictured in Fig. 6.9.

Additionally, columns 4 ($p = 0.0336$) and 5 ($p = 0.0071$) could discriminate between the investigated groups of patients when applying test method I.

Test Method II

Test method II quadruples the number of rectangles in comparison to the standard SPPA. Therefore, the size of the rectangles is adapted to $SD1/4$, $SD2/4$, thus dividing the Poincaré plot into 48×48 rectangles (Fig. 6.8b).

Table 6.5 represents significant columns as a result of test method II and discriminating between DCM_HR and DCM_LR patients. Therefore, the coloured columns are part of highly significant columns of standard SPPA. To this end, test method II was assigned four different columns: column 19 ($p = 0.004$) located within column 5 (blue-coloured) and columns 30 ($p = 0.004$), 31 ($p = 0.001$) and 32 ($p = 0.024$) assigned within column 8 (red-coloured) of standard SPPA, also pictured in Fig. 6.9.

Furthermore, we calculated three significant columns (column 9: $p = 0.014$, column 10: $p = 0.018$ and column 11: $p = 0.024$) located within column 3 of standard SPPA.

Therefore, it could be concluded that the results of test method I and test method II are rather similar to the results of standard SPPA.

6.2.6 Investigating Age Dependencies in Healthy Subjects

Even HRV analysis is an established method for characterizing autonomic regulation [114, 185–187] and has various applications [158, 188–197]. The demands for

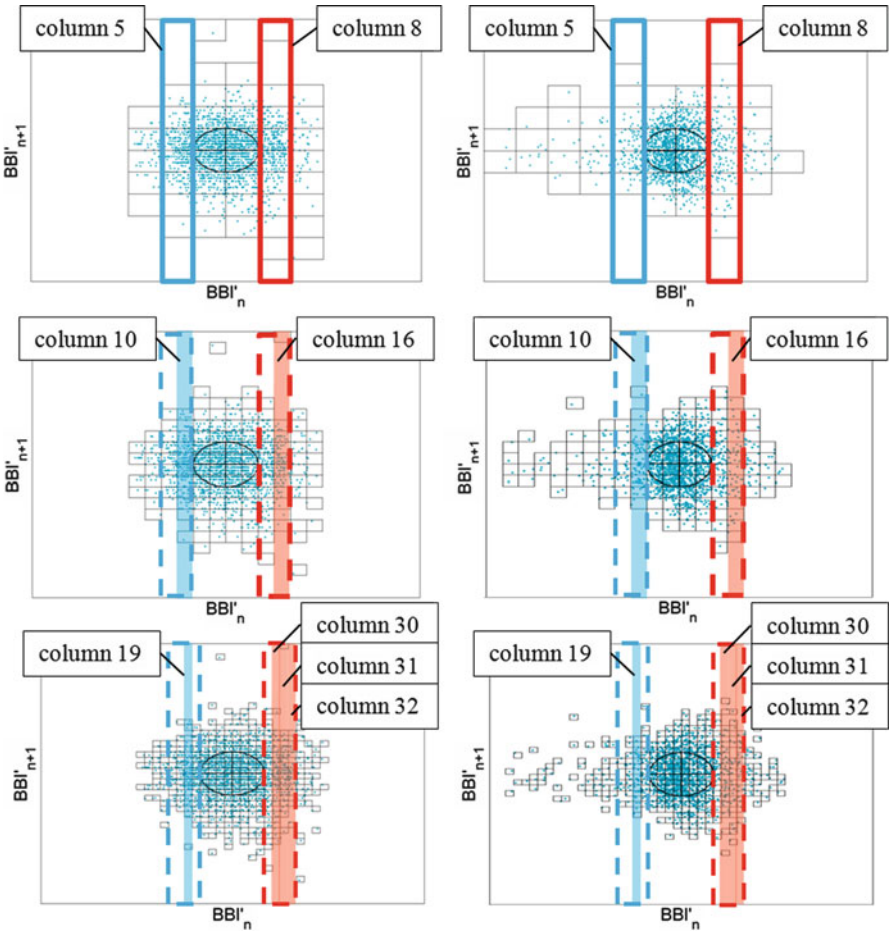

Fig. 6.9 Illustration of significant columns regarding standard SPPA (*top*), test method I (*middle*) and test method II (*bottom*) investigating DCM_HR (*left*) and DCM_LR (*right*)

short-term HRV analysis are continually increasing, especially in the ambulatory sector, to monitor temporary examinations and to obtain an almost immediate test result. There is a great demand for short-term HRV analysis methods determining reference values of linear and nonlinear short-term HRV indices from a healthy population when considering age and sex dependencies.

The objectives of this study are to generally investigate age dependencies of short-term HRV indices and to investigate this age dependency over the course of several decades in healthy subjects [198].

The present study includes 12-lead ECG signals (based on KORA S4 study [199]) recorded under resting conditions over a period of 5 min (sample frequency 500 Hz). The investigated subjects were informed about their participation. Furthermore, the study conforms to the recommendations of the Declaration of Helsinki and has

Table 6.5 Significant indices as a result of test method II for the group test DCM_HR vs. DCM_LR (N.S. not significant; $*p < 0.05$; $**p < 0.01$)

Assigned column within standard SPPA		3	3	3	5	8	8	8
Related column (test method II)		9	10	11	19	30	31	32
DCM_HR	Mean (%)	0	0.010	0.028	4.309	4.237	3.060	1.826
	SD	0	0.037	0.044	1.108	0.546	0.836	0.469
DCM_LR	Mean (%)	0.040	0.065	0.114	3.408	3.544	2.244	1.462
	SD	0.069	0.116	0.144	1.027	0.857	0.681	0.586
p(DCM_HR vs. DCM_LR)		0.014*	0.018*	0.024*	0.004**	0.004**	0.001**	0.024*

Table 6.6 Classification of healthy subjects within each age class (2 and 5 age classes)

2 age classes	N ♂/ ♀	5 age classes	N ♂/♀
25–49 years	1,315 (744/571)	(1) 25–34 years	393 (235/158)
50–74 years	591 (380/211)	(2) 35–44 years	278 (183/95)
		(3) 45–54 years	393 (235/158)
		(4) 55–64 years	278 (183/95)
		(5) 65–74 years	146 (84/62)

been approved by the appropriate medical ethics committee. A total of 1,906 ECG recordings from healthy subjects were selected consisting of 782 women and 1,124 men between the ages of 25 and 74 years (see Table 6.6).

BBI were extracted and ectopic beats (ventricular or supra ectopic beats) and artefacts replaced by interpolated "normal" beats by applying an adaptive filter [183]. The heart rate time series (tachogram) consisting of successive BBI were extracted from the ECG data.

All statistical analyses were performed using the statistical software SPSS 19. Univariate statistical analyses on the basis of descriptive statistics were calculated for PPA and SPPA indices in both age clusters.

The following tests were calculated to determine age dependency of SPPA indices:

Test I: Test for a general age dependency (25–49 years compared with 50–74 years—Table 6.7) using the Mann-Whitney U-test for two independent samples.

Test II: Test for the development of age dependency—age groups (25–34, 35–44, 45–54, 55–64, and 65–74 years—Table 6.8) compared with each other using the Kruskal-Wallis test followed by Mann-Whitney U-tests (Table 6.9).

The indices of the PPA ($SD1$, $SD2$ and $SD1/SD2$) showed highly significant age-dependent differences within tests I and II. In contrast, all represented indices of SPPA showed no significant differences when comparing the respective age decades. Only row 8 represented a slightly significant age-dependent difference

Table 6.7 Results of test I including median values and interquartile ranges applying PPA and SPPA in age clusters 25–49 years and 50–74 years (N.S. not significant; $*p < 0.01$; $**p <$ Bonferroni = 0.0008; $***p < 1 \times 10^{-10}$; $****p < 1 \times 10^{-20}$)

Method	Index	25–49 years $N = 1,315$ Median[lower quartile (0.25) - upper quartile (0.75)]	50–74 years $N = 591$	U-Test Test I
PPA	*SD1*	21.73 (15.51–30.75)	12.9 (9.15–18.69)	****
	SD2	54.24 (42.56–69.78)	39.39 (29.55–52.76)	****
	SD1/*SD2*	0.4 (0.32–0.50)	0.32 (0.25–0.41)	****
SPPA	column 4	1.98 (1.20–2.89)	2.06 (1.29–2.96)	N.S.
	Column 5	12.37 (10.35–14.50)	12.09 (9.58–14.41)	N.S.
	Column 6	34.80 (31.66–37.50)	33.97 (30.80–37.32)	*
	Column 7	34.55 (31.70–38.34)	35.26 (32.49–39.62)	*
	Column 8	13.29 (11.75–14.8)	13.27 (11.53–14.97)	N.S.
	Column 9	1.82 (1.03–2.62)	1.66 (0.66–2.54)	*
	Row 4	1.88 (1.21–2.54)	1.84 (1.24–2.39)	N.S.
	Row 5	13.04 (11.18–14.79)	12.38 (10.36–14.15)	**
	Row 6	35.00 (32.31–37.68)	35.53 (32.89–38.23)	N.S.
	Row 7	33.68 (29.87–36.90)	34.85 (32.05–38.32)	**
	Row 8	14.57 (12.42–16.55)	13.10 (11.07–15.02)	****
	Row 9	1.55 (1.00–2.10)	1.71 (1.18–2.28)	**

when comparing the age decades 45–54 and 55–64 years. The mean values of *SD1*, *SD2* and *SD1*/*SD2* decrease with increasing age when applying tests I and II. In addition, a decreasing trend could be detected only for row 8 of SPPA. Therefore, SPPA indices could perhaps function as very good age-independent indices or risk markers for certain diseases. In a future study, this thesis will be examined by comparing short-term SPPA between patient groups and healthy subjects.

6.3 Application of SPPA to Blood Pressure Signals

Usually Poincaré plots are applied for a two-dimensional graphical and quantitative representation plotting NN_{n+1} against NN_n (see also Sect. 6.2.1). The SPPA method is used to assess successive values of BBI time series and based on simplified phase space embedding so far.

6.3.1 SPPA Adaptation to Blood Pressure (BP)

The present study concentrates on the analysis of SBP as well as DBP measurements plotting SBP_{n+1} over SBP_n and DBP_{n+1} over DBP_n respectively. Therefore, the

Table 6.8 Descriptive statistics results of test II including median values and interquartile ranges applying PPA (*SD1*, *SD2* and *SD1*/*SD2*) and SPPA for different age decades: 25–34, 35–44, 45–54, 55–64 and 65–74 years

	25–34 years $N = 538$	35–44 years $N = 551$	45–54 years $N = 393$	55–64 years $N = 278$	65–74 years $N = 146$
Index	Median [lower quartile (0.25) - upper quartile (0.75)]				
SD1	26.0 (18.5–35.2)	20.8 (15.1–28.9)	15.6 (11.6–21.4)	12.6 (8.8–18.5)	11.6 (7.9–16.4)
SD2	58.7 (46.3–74.8)	53.7 (42.4–70.0)	46.4 (35.1–59.8)	39.0 (29.5–51.4)	34.8 (25.9–45.8)
SD1/*SD2*	0.44 (0.35–0.54)	0.39 (0.31–0.48)	0.33 (0.27–0.42)	0.32 (0.25–0.41)	0.32 (0.25–0.43)
Column 4	1.96 (1.27–2.79)	1.97 (1.10–2.90)	2.05 (1.23–3.02)	2.17 (1.33–2.95)	2.00 (1.27–3.00)
Column 5	12.4 (10.6–14.7)	12.5 (10.4–14.6)	12.1 (9.8–14.3)	11.8 (9.4–14.1)	12.3 (9.7–14.8)
Column 6	35.2 (32.3–37.4)	34.4 (31.4–37.5)	34.5 (31.2–37.1)	33.8 (30.9–37.5)	34.1 (30.4–37.9)
Column 7	34.0 (31.3–37.0)	34.7 (31.8–38.8)	35.4 (32.0–39.4)	35.5 (32.9–39.8)	35.0 (31.9–39.7)
Column 8	13.4 (11.8–14.9)	13.4 (11.7–14.8)	13.0 (11.6–14.9)	13.2 (11.2–14.8)	13.4 (11.9–15.4)
Column 9	1.91 (1.18–2.66)	1.79 (0.96–2.62)	1.62 (0.90–2.62)	1.57 (0.62–2.47)	1.66 (0.73–2.41)
Row 4	1.86 (1.22–2.54)	1.88 (1.18–2.53)	1.87 (1.17–2.48)	1.90 (1.28–2.48)	1.75 (1.14–2.28)
Row 5	13.1 (11.3–14.9)	13.0 (11.2–14.8)	12.9 (10.9–14.5)	12.3 (10.5–14.0)	11.9 (9.6–14.2)
Row 6	34.9 (32.0–37.6)	35.2 (32.3–37.7)	35.2 (33.0–37.7)	35.2 (32.9–38.2)	36.2 (33.2–39.3)
Row 7	33.1 (29.6–36.8)	33.9 (29.9–37.1)	34.2 (31.1–36.9)	34.9 (32.1–38.0)	35.3 (32.4–39.1)
Row 8	15.2 (12.9–17.2)	14.4 (12.2–16.2)	13.8 (11.8–15.6)	13.1 (11.1–14.9)	12.4 (9.6–14.7)
Row 9	1.48 (0.88–2.00)	1.59 (1.05–2.19)	1.66 (1.15–2.20)	1.65 (1.18–2.22)	1.88 (1.25–2.37)

Table 6.9 Results of Kruskal-Wallis test followed by Mann-Whitney U-tests between each two age decades (test II) applying PPA (*SD1*, *SD2* and *SD1*/*SD2*) and SPPA (column 4–9 and row 4–9); 1 = 25–34 years, 2 = 35–44 years, 3 = 45–54 years, 4 = 55–64 years and 5 = 65–74 years (N.S. not significant; $*p < 0.01$; $**p <$ Bonferroni = 0.0008; $***p < 1 \times 10^{-10}$; $****p < 1 \times 10^{-20}$)

		Bonferroni post hoc test									
Index	Kruskal-Wallis test	1 2	2 3	3 4	4 5	1 3	2 4	3 5	1 4	2 5	1 5
SD1	****	****	****	**	N.S.	****	****	**	****	****	****
SD2	****	*	***	**	N.S.	****	****	***	****	****	****
SD1/*SD2*	****	**	**	N.S.	N.S.	****	***	N.S.	****	**	****
Column 4	N.S.	N.S.	N.S.	N.S.	N.S.	N.S.	N.S.	N.S.	N.S.	N.S.	N.S.
Column 5	N.S.	N.S.	N.S.	N.S.	N.S.	*	*	N.S.	*	N.S.	N.S.
Column 6	N.S.	*	N.S.	N.S.	N.S.	*	N.S.	N.S.	*	N.S.	N.S.
Column 7	**	*	N.S.	N.S.	N.S.	**	N.S.	N.S.	**	N.S.	N.S.
Column 8	N.S.	N.S.	N.S.	N.S.	N.S.	N.S.	N.S.	N.S.	N.S.	N.S.	N.S.
Column 9	*	N.S.	N.S.	N.S.	N.S.	**	N.S.	N.S.	**	N.S.	*
Row 4	N.S.	N.S.	N.S.	N.S.	N.S.	N.S.	N.S.	N.S.	N.S.	N.S.	N.S.
Row 5	**	N.S.	N.S.	N.S.	N.S.	N.S.	**	*	**	**	**
Row 6	*	N.S.	N.S.	N.S.	N.S.	N.S.	N.S.	N.S.	N.S.	*	**
Row 7	**	N.S.	N.S.	*	N.S.	*	**	*	**	**	**
Row 8	****	*	*	*	N.S.	**	**	**	***	***	****
Row 9	**	N.S.	N.S.	N.S.	N.S.	**	N.S.	N.S.	**	N.S.	**

equations (Eqs. 6.3 and 6.4) calculating *SD1* and *SD2* are adapted to the investigated blood pressure time series (BP). Furthermore, the ratio *SD1*/*SD2* is calculated. These indices are similarly determined for SBP and DBP.

The SPPA procedure applying BP includes the following four procedures (as seen in Fig. 6.10) which are similar to standard SPPA:

- *SD1* (Eq. 6.14) and *SD2* (Eq. 6.14) are calculated according to traditional PPA (Fig. 6.10a):

$$SD1 = \sqrt{\mathrm{VAR}\left(\frac{BP_n - BP_{n+1}}{\sqrt{2}}\right)} \tag{6.14}$$

$$SD2 = \sqrt{\mathrm{VAR}\left(\frac{BP_n + BP_{n+1}}{\sqrt{2}}\right)}. \tag{6.15}$$

- The cloud of points is rotated by an angle of $\alpha = 45$ around the main focus of the cloud of points (Fig. 6.10b).
- A grid of 12×12 rectangles is fitted to the cloud of points starting from the main focus of the cloud of points where the size of each rectangle is adapted to *SD1* (height) and *SD2* (width) (see Fig. 6.10c).

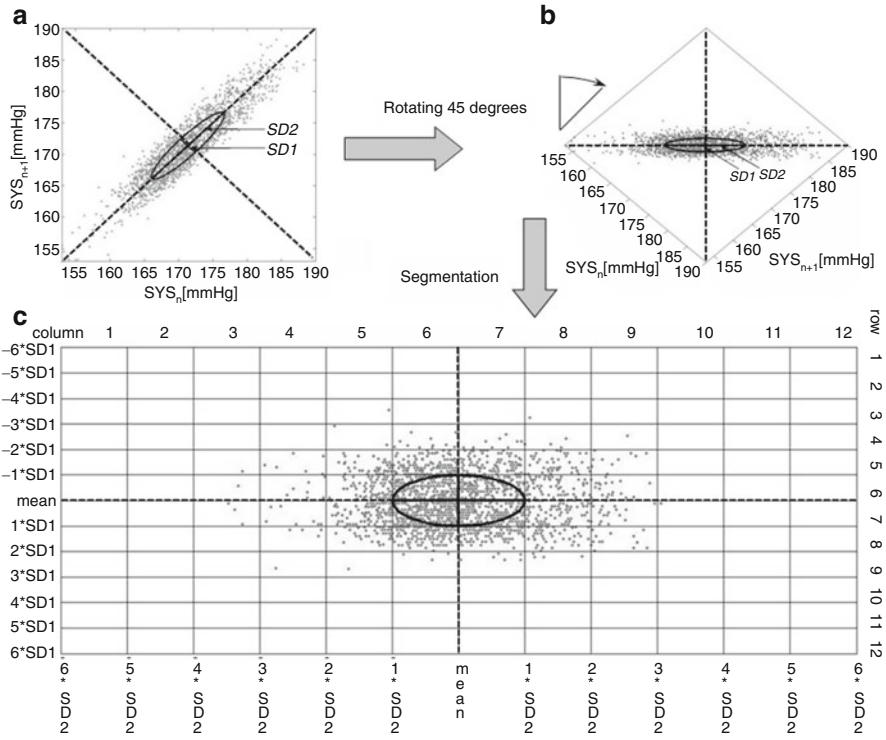

Fig. 6.10 Adaptation of SPPA to blood pressure signals (e.g. SBP): (**a**) traditional Poincaré plot, calculation of *SD1* and *SD2*; (**b**) rotated Poincaré plot (45° around the main focus); (**c**) segmentation of the Poincaré plot (12 × 12 rectangles, based on *SD1* and *SD2*), calculation of row- and column probabilities and declaration of SPPA indices

- For estimating single probabilities (p_{ij}) the number of points within every rectangle is counted and normalized by the total number of points. Based on these single probabilities, all row (i) and column (j) probabilities are calculated by summation of the related single probabilities (Eqs. 6.6 and 6.7).

6.3.2 *Application to Hypertensive Pregnancy Disorders*

Hypertensive pregnancy disorders are a leading cause of maternal and foetal morbidity and mortality and affect 6–8% of all pregnancies. These disorders can result in severe complications for the mother and the foetus of which pre-eclampsia (PE) has the worst perinatal outcome [200]. Several studies suggested that the autonomic nervous system plays an important role in the process of developing hypertensive pregnancy disorders, especially PE [201–204].

Table 6.10 Classification of pregnant women with hypertensive disorders (oHY) and pre-eclampsia (PE) including the number of patients, mean, range and SD of age (in years) and week of gestation (gw)

Group	Number	Age (mean ± SD)	Age range	gw (mean ± SD)	Range gw
oHY	40	28.6 ± 5.0	19–38	32.9 ± 5.8	20–41
PE	29	27.7 ± 5.4	19–38	32.2 ± 4.1	25–39

Table 6.11 Highly significant SPPA indices from SBP and DBP time series (Mann-Whitney U-test) with mean values and SDs differentiating both groups (oHY/PE, probabilities in percentages)

Method	Index	p (oHY vs. PE)	oHY (mean ± SD)	PE (mean ± SD)
	Column 4	1.67×10^{-4}	0.59 ± 0.71	1.59 ± 1.36
	Column 6	4.75×10^{-5}	42.17 ± 7.59	34.02 ± 6.61
SBP	Column 7	2.46×10^{-5}	28.22 ± 4.78	34.79 ± 6.38
	Column 9	2.23×10^{-4}	3.16 ± 1.04	1.99 ± 1.23
	Column 10	4.16×10^{-5}	0.57 ± 0.47	0.15 ± 0.21
DBP	Row 3	2.00×10^{-4}	0.34 ± 0.16	0.22 ± 0.14

Therefore, Seeck et al. [205] investigated whether women suffering from pre-eclampsia could be differentiated from women suffering from various other hypertensive pregnancy disorders employing the SPPA. Continuous blood pressure (BP) recordings (30 min; Portapres, TNO Biomedical Instrumentation) of 69 pregnant women with hypertensive disorders (29 PE, 40 with chronic or gestational hypertension (oHY)) were included (Table 6.10).

To test for significant differences between the investigated groups, we applied the Mann-Whitney U-test (level of significance: $p < 0.001$). The linear discriminant function analysis (LDA) was performed including all highly significant SPPA ($p < 0.001$) indices. The performance of each index was assessed by estimating the area under the ROC curve. Indices achieving an area under the ROC curve (AUC) above 0.75 were combined in sets of two or three and enrolled in LDA again to determine the optimal multivariate set of indices.

SPPA exhibits significant differences between PE and oHY (Table 6.11) of SBP and DBP. Especially columns 4 ($p = 1.67 \times 10^{-4}$), 6 ($p = 4.75 \times 10^{-5}$), 7 ($p = 2.46 \times 10^{-5}$), 9 ($p = 2.23 \times 10^{-4}$) and 10 ($p = 4.16 \times 10^{-5}$) identified highly significant modifications when applying SBP time series. SPPA of DBP time series indicated one highly significant difference in row 3 ($p = 2.00 \times 10^{-4}$).

Furthermore, univariate as well as multivariate LDA (Table 6.12) demonstrated that indices deriving from SPPA are suitable for differentiation between oHY and PE. Therefore, this procedure could contribute to the differential diagnosis of hypertensive pregnancy disorders.

Univariate LDA of highly significant SPPA indices revealed five indices that achieved a ROC value above 0.75, whereas SBP_column7 had the most discriminative power (AUC = 0.781). The optimal multivariate set of indices containing

Table 6.12 SPPA indices with highest values of area under the ROC curve and the best sets of indices when investigating two and three indices

Indices/set of indices	AUC
SBP_column7	0.781
SBP_column10	0.774
SBP_column6	0.771
DBP_row3	0.752
SBP_column4	0.751
SBP_column10, SBP_column7	0.836
SBP_column10, SBP_column7, DBP_row3	0.847

two indices consisted of SBP_column7 and SBP_column10 and improved the ROC value up to 0.836. The best multivariate result was achieved by adding DBP_row3 (AUC = 0.847).

Patterns of SBP and DBP variability differ significantly between hypertensive pregnancy disorders reflecting altered mechanisms of BP regulation. The present study of SPPA in hypertensive pregnancy disorders is a potential technique for analysing BP time series which would allow for differentiation between chronic and gestational hypertension and pre-eclampsia. Therefore, SPPA could contribute to a differential diagnosis of hypertensive pregnancy disorders.

6.4 Lagged Segmented Poincaré Plot Analysis

The objective of LSPPA is to investigate if time correlations will provide information about the physiological background of the impaired autonomous regulation, especially in very low (VLF = 0.0033–0.04 Hz) and low-frequency (LF = 0.04–0.15 Hz) bands. Therefore, we will provide additional insight into the underlying physiological mechanism of heart rate regulation. Furthermore, we will demonstrate enhanced risk stratification by applying indices from the LSPPA method.

6.4.1 Method

The SPPA method (Sect. 6.2.1) considers NN_n as a function of its subsequent NN_{n+m} by a lag of one ($m = 1$). The lag is defined as the distance between the investigated *NN*. For time correlation analysis, LSPPA investigates patterns applying lags from $m = 1 \cdots 100$ (as seen in Fig. 6.11).

For more comparable results, the same time series length for each time series were used by cutting an offset (specific number of *NN*) at the end of each time series (Eq. 6.16). This step yields the following Eqs. 6.17 and 6.18 which are based on Eqs. 6.1 and 6.2:

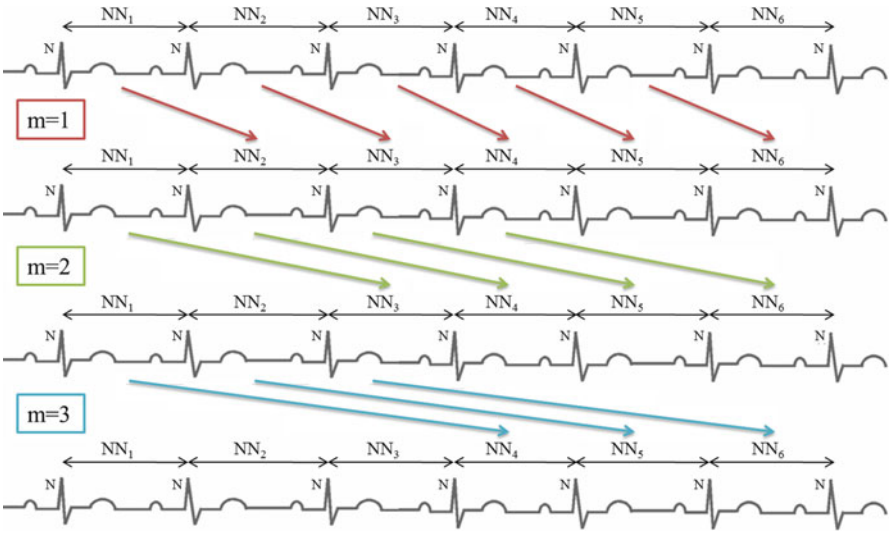

Fig. 6.11 Exemplary principal of time correlation analysis applying LSPPA for *NN* intervals (lags: $m = 1$–3)

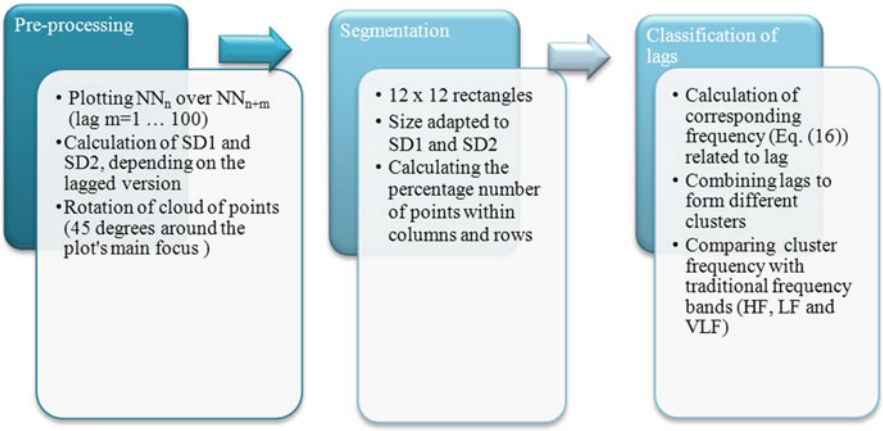

Fig. 6.12 The simplified procedure of lagged segmented Poincaré plot analysis (LSPPA)

$$\text{offset} = 100 - m \tag{6.16}$$

$$NN_n = (NN_1, NN_2, \ldots, NN_{N-m-\text{offset}}) \tag{6.17}$$

$$NN_{n+m} = (NN_{m+1}, NN_{m+2}, \ldots, NN_{N-\text{offset}}). \tag{6.18}$$

The simplified principle of LSPPA shown in Fig. 6.12 is divided into three main parts: preprocessing, segmentation and lag classification.

The corresponding frequency f, related to the lag (m), assuming the mean values of all investigated patients ($meanNN = 867$ ms), is calculated as follows (Eq. 6.19):

$$f \sim 1/(m * meanNN). \tag{6.19}$$

The lags are combined into 8–10 different clusters covering the most significant frequencies. Too many single indices will be avoided since these would probably lead to too much uncertainty. The defined clusters include 5–10 lags. Lower clusters include five lags, whereas the upper ones include ten lags, according to the degree of difference between the frequencies. This procedure must be separately and specifically defined for each study because of its dependency on the meanNN of all investigated subjects. One example of classification of lags will be shown in the next chapter in which LSPPA to DCM patients are implicated (Sect. 6.4.2, Fig. 6.10).

The cardiovascular regulation is influenced by various oscillations which differ in origin. Bernjak et al. [206], Rossi et al. [207] and Tikhonova et al. [208] published the physiological correlations of frequency bands related to respiratory (0.145–0.6 Hz), intrinsic myogenic (0.052–0.145 Hz), neurogenic/sympathetic (0.021–0.052 Hz) and endothelial (0.0095–0.021 Hz) activity.

6.4.2 *Application of LSPPA to Determine Risk Stratification in Patients Suffering from Dilated Cardiomyopathy*

The present study applies LSPPA to DCM patients using similar data pre-processing and statistical methods as that of the application study of SPPA (see Sect. 6.2.4). We enrolled 91 patients (DCM_HR = 14, DCM_LR = 77) suffering from DCM (Table 6.2). The goal of the investigation was to determine whether LSPPA is able to analyse time correlations corresponding to different frequency bands ($f = 0.012 \cdots 1.153$ Hz—Fig. 6.13) and whether this type of analysis could improve risk stratification.

Significant indices for the group test between high- and low-risk patients of DCM applying the BBI time series are presented in Table 6.13. It could be shown that LSPPA presents highly significant indices in all clusters except in cluster II ($p = 0.0241$). The revealed significances of LSPPA could especially be found in column 8 (cluster I: $p = 0.0021$; cluster VII: $p = 0.0002$), column 5 (cluster V: $p = 0.0014$; cluster VI: $p = 0.0019$), row 3 (cluster III: $p = 0.0006$) and row 5 (cluster IV: $p = 0.0002$; cluster VIII: $p = 0.0047$). Therefore, cluster IV (sensitivity = 85.7%; specificity = 71.4%; AUC = 80.89%) and cluster VII (sensitivity = 78.57%; specificity = 74%; AUC = 80.89%) present the best indices (marked in Table 6.13).

By comparison, traditional PPA does not achieve any significant indices investigating *SD1*, *SD2* and their ratio *SD1*/*SD2*. Therefore, calculating the sensitivity, specificity as well as AUC was not performed.

It could be demonstrated that high-risk DCM patients achieve a significantly higher row and column probability compared to low-risk DCM patients. Especially

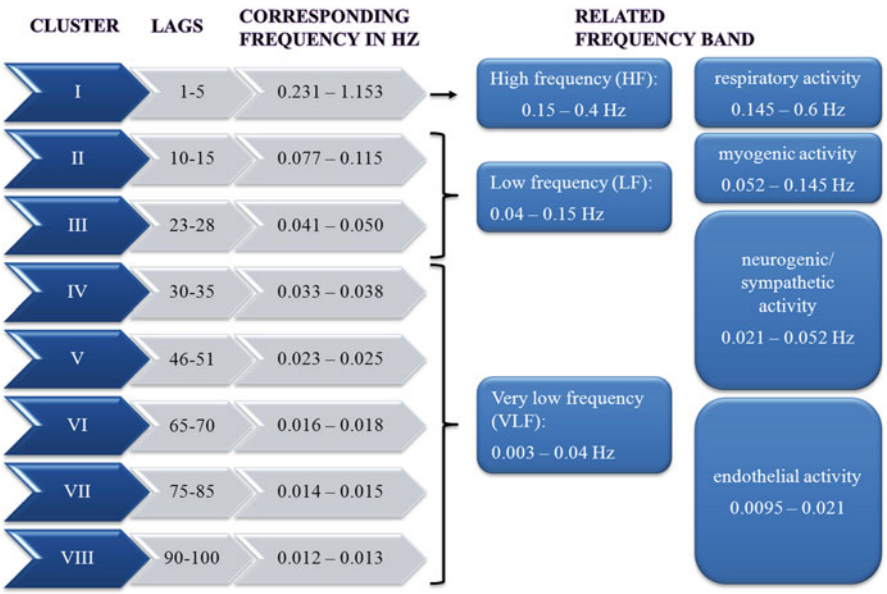

Fig. 6.13 Declaration of clusters of lags including their corresponding frequencies (in Hz) and related frequency bands, with application for DCM patients

Table 6.13 Significant LSPPA and PPA indices (**highly significant ($p < 0.01$); *significant ($0.01 = p = 0.05$); N.S. not significant; n.c. not calculated) differentiating DCM_HR vs. DCM_LR including the mean values and SDs for each group; sensitivity in % (SENS), specificity in % (SPEC) and the area under the curve (AUC) in %

			DCM_LR		DCM_HR		SENS	SPEC	AUC
Cluster	Index	p	Mean	SD	Mean	SD	in %	in %	in %
I	Column 8	0.0021**	12.5264	2.1366	14.2066	1.2742	71.4	72.7	76.16
II	Column 5	0.0241*	12.5567	2.7892	14.4045	2.6267	62.34	57.14	68.37
III	Row 3	0.0006**	0.3588	0.2297	0.1433	0.1604	64.3	85.7	78.9
IV	Row 5	0.0002**	11.7781	1.8335	13.374	0.8906	85.7	71.4	80.89
V	Column 5	0.0014**	13.3114	2.3159	15.5025	2.3892	78.57	80.5	76.72
VI	Column 5	0.0019**	13.2425	2.1543	15.293	2.3726	78.6	72.7	76.35
VII	Column 8	0.0002**	13.5174	1.7237	15.2921	1.2757	78.57	74	80.89
VIII	Row 5	0.0047**	12.3039	1.5853	13.4518	1.5261	71.4	76.6	73.84
PPA	*SD1*	N.S.	30.003	17.554	34.136	18.866	n.c.	n.c.	n.c.
	SD2	N.S.	36.135	18.389	39.18	24.623	n.c.	n.c.	n.c.
	SD1/SD2	N.S.	0.814	0.141	0.885	0.149	n.c.	n.c.	n.c.

the number of points within the more central regions (columns 5 and 8) increased, whereas the number of points within the peripheral regions decreased (column 1–3, 10–12). This represents a reduced variability in high-risk DCM patients.

The most important differences were recognized within LF and VLF bands corresponding to endothelial and neurogenic/sympathetic activities. Oscillations at

frequencies in VLF bands are often related to vasomotor tones of thermoregulation or to the dynamics of hormonal systems, but the origin and frequency of these oscillations are still unknown [209]. The VLF band includes frequency bands indicating endothelial activity (clusters VI–VIII). Treasure et al. [210] demonstrated that endothelium-dependent dilation of the coronary microvasculature is impaired in patients suffering from DCM. Endothelial dysfunction in DCM patients could also be proven in animal studies, e.g. Kaiser et al. [211], who found impaired endothelium-dependent vasodilatation to acetylcholine in the hind limb of dogs with experimental heart failure.

6.4.3 LSPPA in Comparison to Traditional Time and Frequency Domain Analysis

We have proven that LSPPA has the potential to differ between high- and low-risk patients of DCM regarding several frequencies (0.012–1.153 Hz), corresponding to traditional HF, LF and VLF frequency bands. In this study, HRV is quantified with indices calculated from time- and frequency-domain analyses, comparing them with LSPPA by applying the BBI time series of DCM patients (see also Sect. 6.2.4 and Table 6.2) [55].
The following indices are calculated from time-domain analyses (HRV_TD):

- meanNN = mean value of BBI time series (ms)
- SDNN = standard deviation of BBI time series (ms)
- RMSSD = square root of the mean squared differences of successive BBIs (ms)
- pNN50 = percentage of successive BBI differences > 50 ms

In addition, traditional PPA provides detailed beat-to-beat information and calculates the following linear indices:

- *SD1* = the standard deviation (ms) of short-term BBI variability (Eq. 6.3)
- *SD2* = the standard deviation (ms) of long-term BBI variability (Eq. 6.4)
- $SD1/SD2$ = the axes ratio

The following gives an introduction to frequency-domain analysis methods that are applied to fast fourier transform (FFT) and short-time fourier transform (STFT). When performing frequency-domain analysis, the tachogram of each patient is resampled (2 Hz, linear interpolation) to obtain an equidistant time series.

The FFT is applied using the Blackman Harris window. The power spectra of the entire equidistant time series are estimated and relevant frequency-domain indices are extracted in accordance with the Task Force of the European Society of Cardiology [55]:

- HF = power in high-frequency band (0.15–0.4 Hz) (s^2)
- LF = power in low-frequency band (0.04–0.15 Hz) (s^2)
- VLF = power in very-low-frequency band (0.0033–0.04 Hz) (s^2)

- LF/HF = ratio of LF to HF power
- LFn = normalized LF
- HFn = normalized HF

The STFT (Eq. 6.20) provides a time-frequency decomposition of BBI time series. Considering the averaged time series for each group of patients $x(i)$ and applying Blackman Harris window $w(i)$ with $Ns = 512$ samples, the FT of the windowed signal $x(i)w(i-k)$ is the STFT [212, 213] and where n and $k(1 = n = N)$ represent the discrete time and frequency:

$$X_k(n) = \sum_{i=k-\frac{Ns}{2}}^{i=k+\frac{Ns}{2}} x(i)\, w(i-k) \mathrm{e}^{-j\frac{2\pi n}{Ns} * i}. \tag{6.20}$$

The window is shifted by one sample. This procedure is repeated up to the end of the BBI time series. To generate comparable frequency-domain values (VLF, LF and HF), the power density spectrum $X_k(n)$ is integrated within the specific frequency band.

The spectral resolution F_a (Eq. 6.21) depends upon the sampling frequency (2 Hz) of the (resampled) tachogram ($\Delta T = 0.5$ Hz) and upon the length of the selected window ($Ns = 512$ samples):

$$F_a = \frac{1}{Ns * \Delta \mathrm{T}}. \tag{6.21}$$

Table 6.14 represents the results of time-domain (HRV_TD and PPA) and frequency-domain (FFT and STFT) analyses including mean values and their standard deviations for all groups of DCM patients and healthy subjects (REF). Calculating the group test between DCM patients and REF, we could obtain highly significant indices within the time-domain (SDNN, RMSSD, pNN50, *SD1* and *SD2*) as well as the frequency-domain analyses in VLF, LF and HF bands when applying FFT and STFT. However, when investigating the group test between high- and low-risk DCM patients, neither time-domain nor frequency-domain analyses could confirm risk stratification in DCM patients.

The power spectra for each group of patients considering FFT and STFT (see Figs. 6.14 and 6.15, respectively) represent the power intensity within HF, LF and VLF bands. The figures show the averaged plots within the considered groups of high- and low-risk DCM patients and healthy subjects (REF).

Calculating the spectral resolution of STFT (Eq. 6.21), we reach a resolution of $F_a = 0.0039$ Hz for each window ($Ns = 512$ samples; $\Delta T = 0.5$ s) and a resolution of $F_a = 0.0006$ Hz for the whole signal ($Ns = 3{,}600$ samples; $\Delta T = 0.5$ s) applying FFT. In contrast, LSPPA achieves a spectral resolution up to 0.0002 Hz within VLF band ($m = 100$) depending on m, whereby higher lags present higher resolutions. Furthermore, STFT seems to have a different visual appearance within the investigated patient groups. However, there are no significant changes

Table 6.14 Significant STFT, PPA, time-domain (HRV_TD) and frequency-domain (FFT) indices of the group tests DCM_HR vs. DCM_LR and DCM vs. REF, including mean values and SDs; N.S. not significant; $*p < 0.05$; $**p < 0.01$

	Index	DCM_HR vs. DCM_LR	DCM vs. REF	DCM_HR Mean	SD	DCM_LR Mean	SD	REF Mean	SD
HRV_TD	meanNN (ms)	N.S.	N.S.	828.43	112.30	906.96	145.86	858.75	134.40
	SDNN (ms)	N.S.	**	33.45	17.70	36.98	21.66	60.38	21.54
	RMSSD (ms)	N.S.	**	17.43	11.46	20.53	12.14	47.99	26.98
	pNN50 (%)	N.S.	**	0.03	0.06	0.05	0.08	0.24	0.23
PPA	*SD1*(ms)	N.S.	**	30.00	17.55	34.14	18.87	56.27	21.97
	SD2(ms)	N.S.	**	36.13	18.39	39.18	24.62	63.47	22.51
	SD1/*SD2*	N.S.	N.S.	0.81	0.14	0.89	0.15	0.88	0.15
FFT	VLF (s^2)	N.S.	**	176.47	198.77	178.90	212.84	281.80	200.99
	LF (s^2)	N.S.	**	44.09	47.08	79.64	130.66	214.58	170.97
	HF (s^2)	N.S.	**	29.62	41.75	33.30	44.89	216.41	213.01
	LF/HF	N.S.	*	2.49	2.18	3.44	3.70	1.94	2.00
	LFn	N.S.	*	0.66	0.11	0.67	0.18	0.56	0.18
	HFn	N.S.	*	0.34	0.11	0.33	0.18	0.44	0.18
STFT	VLF	N.S.	**	23341	12800	20264	11235	37001	12950
	LF	N.S.	**	11547	7087	8869	5443	21589	8592
	HF	N.S.	**	11004	6211	10097	7387	29293	15932

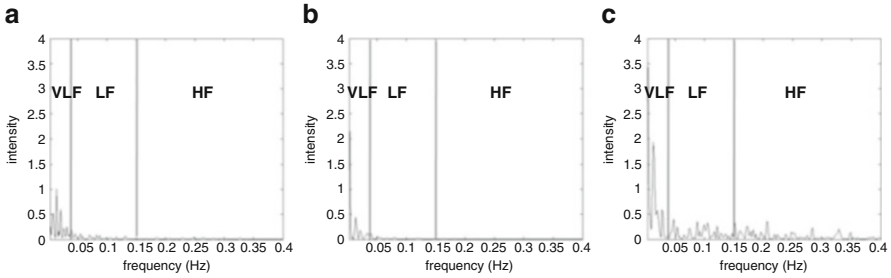

Fig. 6.14 FFT plots of high-risk DCM patients (**a**), low-risk DCM patients (**b**) and healthy subjects (**c**) averaged over all investigated subjects within each group. The frequency bands HF, LF and VLF are labelled

considering differences in the standardized frequency bands HF, LF and VLF when discriminating between high- and low-risk DCM patients (see Table 6.14).

Comparing the results of time- and frequency-domain analyses and LSPPA when applying high- and low-risk DCM patients, we can conclude that LSPPA represents highly significant indices (as seen in Table 6.13) within all defined clusters. LSPPA results are therefore better suited for time correlation analyses. It has been confirmed that LSPPA improves the results of traditional time- and frequency-domain analyses with regard to the corresponding frequency bands.

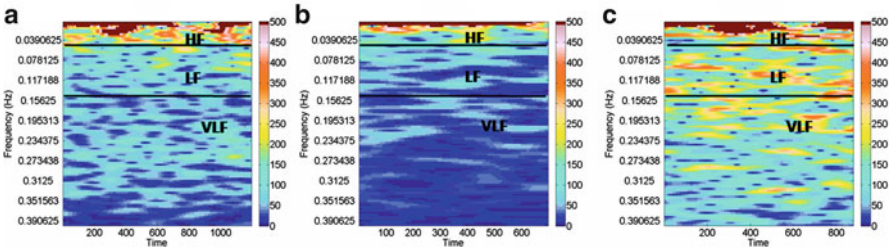

Fig. 6.15 STFT plots of high-risk DCM patients (**a**), low-risk DCM patients (**b**) and healthy subjects (**c**) averaged over all investigated subjects within each group. The frequency bands HF, LF and VLF are labelled

6.5 Perspective

We successfully performed several studies including SPPA for BBI time series (risk stratification of DCM patients and age dependencies in healthy subjects) as well as blood pressure signals (for application in the area of hypertensive pregnancy disorders). Furthermore, we could demonstrate that indices obtained from LSPPA improve risk stratification in DCM patients and that the calculated time correlations provide some additional insights into the underlying physiological mechanisms of these patients.

In this regard, several approaches have not yet been included and will be described in the following chapters. In these chapters, we will investigate the BBI time series of ECG signals, SBP as well as DBP and respiratory signals (RESP). Subsequent studies should focus on univariate (1D) as well as multivariate (2D and 3D) analyses of cardiovascular signals.

6.5.1 Application of SPPA and LSPPA to Respiratory Signals

Respiratory sinus arrhythmia (RSA), one of the physiological interactions between respiration and circulation, is HRV in synchrony with respiration where the BBI time series based on an ECG is shortened during inspiration and prolonged during expiration. RSA has been a focus of study since its first description by Ludwig [214]. The review article of Tripathi [215], inter alia, gives an overview of respiratory frequency and tidal volume associated with HRV.

The respiration signal significantly differs in patients suffering from cardiovascular diseases compared to healthy subjects. Therefore, we will investigate this influence by applying univariate and multivariate SPPA as well as LSPPA to investigate BBI time series, SBP- and DBP signals. The considerations about using multivariate SPPA methods are described in the following Sects. 6.5.2 (2D SPPA)

and 6.5.3 (3D SPPA) in more detailed way. Further considerations exist in the field of investigating different diseases like DCM, schizophrenia or pre-eclampsia using the entire respiration signal as well as inspiration and expiration periods.

6.5.2 *Application of SPPA to Two-Dimensional Analysis of Signal Couplings (2D SPPA)*

SPPA retains nonlinear features of the investigated system and until now has been applied to BBI time series and blood pressure signals, respectively. For multivariate analyses, we will consider the interaction between two different time series. The resulting method will be adapted by determining the phase space of two series instead of the pseudo-phase space of only one time series—the so-called 2D SPPA. This was recently published in a pilot study by Seeck et al. [216].

The 2D SPPA generally will include the following procedures (see Fig. 6.16) similar to the recently presented SPPA method [173] which was introduced in Sect. 6.2.1:

1. The linear indices *SD1* and *SD2* are calculated according to traditional PPA. A linear regression is fitted into the cloud of points and the angle α between the x-axis and the regression line is calculated (see Fig. 6.16a).
2. The cloud of points is rotated by the angle α around the main focus of the cloud (see Fig. 6.16b) to perform a simplified *SD1*/*SD2*-adapted probability-estimating procedure (with the consideration as to whether the cloud rotation will improve the results of 2D SPPA).
3. A grid of 12×12 rectangles is fitted into the plot starting from the main focus of the plot where the size of each rectangle is adapted to *SD1* (height) and *SD2* (width) (see Fig. 6.16c).
4. For estimating single probabilities (probability of occurrence: po_{ij}), the number of points within each rectangle is counted and normalized by the total number of points. Based upon these single probabilities, all row (i) and column (j) probabilities are calculated by summation of the related single probabilities (Eqs. 6.6 and 6.7).

To evaluate 2D SPPA patterns, it is perhaps necessary to observe specific regions of the cloud of points rather than the total row and column probabilities. Therefore, a novel segmentation algorithm is to be considered (as seen in Fig. 6.17) calculating the summation of the related single probabilities as (Eqs. 6.22–6.25):

$$po_{ri\_\text{left}} = \sum_{j=1}^{6} p_{ij} \tag{6.22}$$

$$po_{ri\_\text{right}} = \sum_{j=7}^{12} p_{ij} \tag{6.23}$$

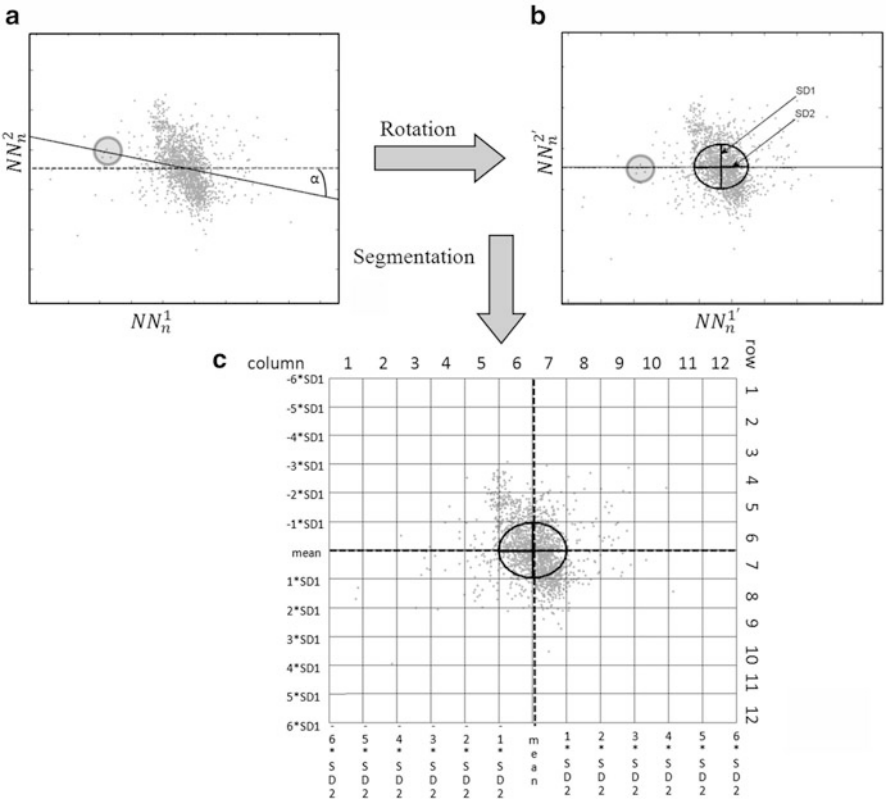

Fig. 6.16 A 2D SPPA procedure: (**a**) calculation of *SD1* and *SD2* and angle α between linear regression line and *x*-axis, (**b**) rotation of the cloud of points by α (an example for movement of points is highlighted by the *circle*); (**c**) segmentation of the plot into 12×12 rectangles based on *SD1* and *SD2* with declaration of SPPA indices

$$po_{cj\_\text{top}} = \sum_{i=1}^{6} p_{ij} \tag{6.24}$$

$$po_{cj\_\text{bottom}} = \sum_{i=7}^{12} p_{ij}. \tag{6.25}$$

In a first pilot study [216] with patients suffering from persistent atrial fibrillation (AF), we applied 2D SPPA of BBI time series and SBP including the segmented algorithm of 2D SPPA. All patients underwent successful electrical cardioversion (CV) which was defined as a stable sinus rhythm for the following 24 h. A follow-up examination after one year was obtained for all patients as well as their general practitioners. AF recurred in 12 patients within the first year (group: REZ) and 15 patients remained in sinus rhythm for at least one year (group: SR) (see Table 6.15).

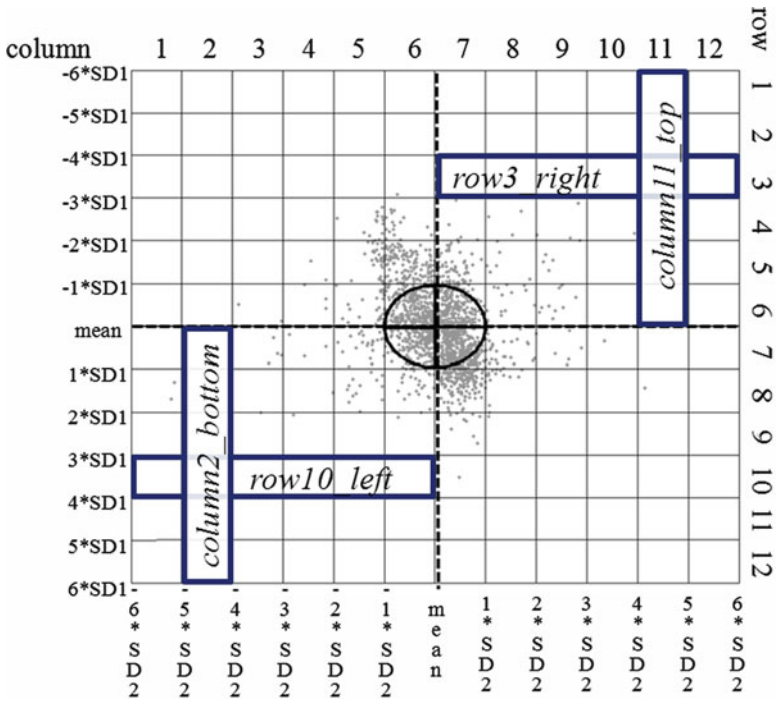

Fig. 6.17 Exemplary consideration of a novel segmentation algorithm of 2D SPPA

Table 6.15 Classification of SR (sinus rhythm) and REZ (AF recurrence) patients including the number of patients, gender, mean value, range and SD of age (in years)

Group	Number	Numbermale/female	Mean ± SD age	Range age
SR	15	10/6	62.5 ± 11.9	44–79
REZ	12	4/7	69.0 ± 6.8	59–83

When discriminating between the two groups of patients, we obtained one significant index (BBI/SBP-row10_left: KS-test for two samples: $p_{10\_left} = 0.016$; AUC = 78%) which was derived by applying 2D SPPA. This index reflects the probability of a low BBI following a very low SBP. This system's status is found more often in patients remaining in sinus rhythm than in patients with an AF relapse. This supports the assumption of reduced BRS and a lower variation of the system in patients with AF [217].

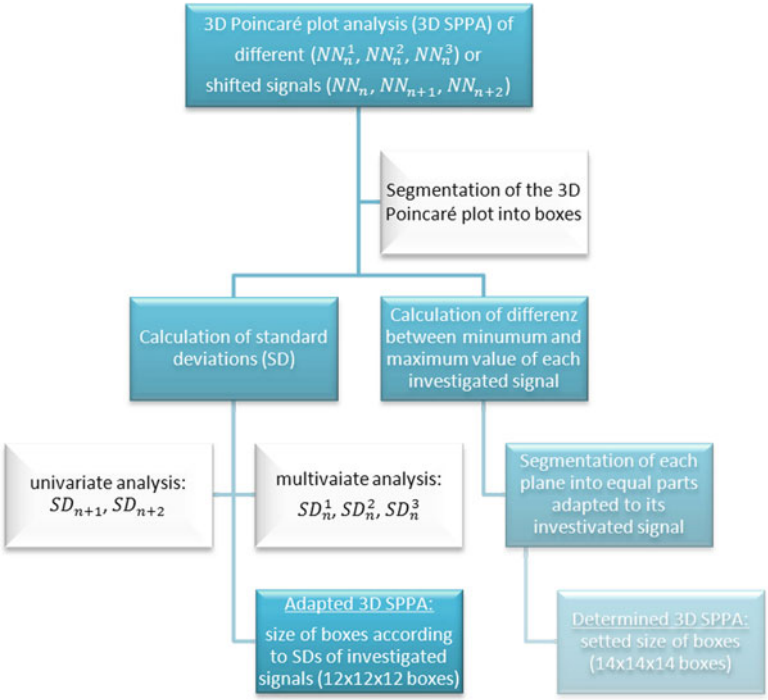

Fig. 6.18 Principle of 3D SPPA including univariate and multivariate analyses

6.5.3 Application of SPPA to Three-Dimensional Analysis of Signal Couplings (3D SPPA)

Three-dimensional SPPA (3D SPPA) methods will investigate three shifted signals from a time series (univariate) or three different signals (multivariate: e.g. BBI time series, SBP and DBP) plotted in several box models. The basis of our methodology rests on specific subdivisions of the box model which is similar to SPPA. Figure 6.18 represents the general principle of 3D SPPA considering univariate and multivariate analysis methods.

Furthermore, there is discussion to generate two different versions of 3D SPPA according to the size of the boxes within the 3D cubes plot (Fig. 6.18):

- First version: Adapted 3D SPPA (size of boxes depending on the calculated standard deviations (SD) of investigated signals)
- Second version: Determined 3D SPPA (size of boxes are previously defined to get equal dimensions for each patient)

The first version (adapted 3D SPPA) deals with the calculation of the standard deviation (SD). Therefore, each axis of the 3D cubes plot is divided into 12 equal

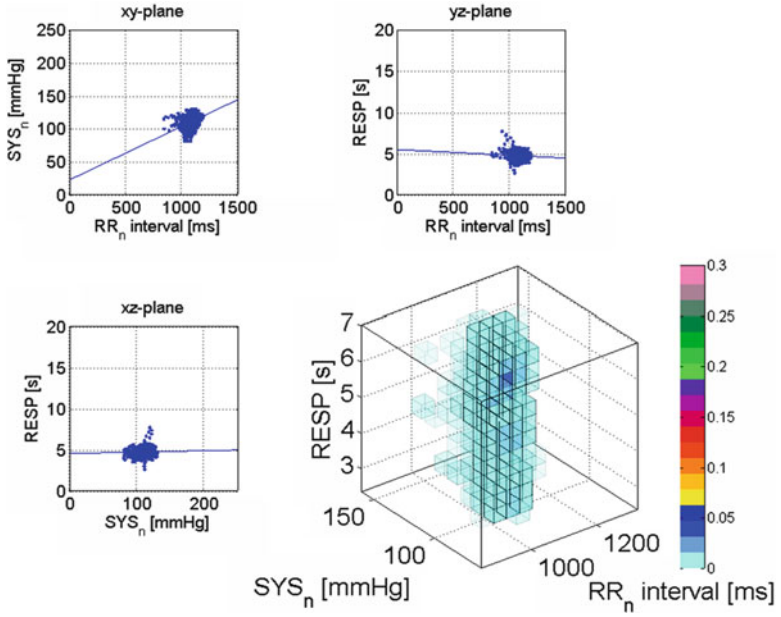

Fig. 6.19 Exemplary colourized 3D cubes plot of the first version of 3D SPPA (adapted 3D SPPA) including the planes and their regression lines

parts adapted to the calculated SD of investigated signals with regard to the axis. The resulting 3D cubes plot consists of $12 \times 12 \times 12$ equal boxes whereby the centre of all boxes represents the main focus of the cloud of points (as seen in Fig. 6.19). Depending on the percentage of measuring points within each box, we colour the boxes to allow for an improved graphical information processing.

To exemplarily demonstrate the first version (multivariate case) of 3D SPPA, we investigated BBI time series, SBP and RESP, as found in Fig. 6.19. In addition, the adapted 3D SPPA shows all three planes of a 3D cubes plot and the regression line of each plane.

The second version (determined 3D SPPA) deals with an equal grid for all patients depending on the investigated signals. Therefore, the distance between minimum and maximum of each investigated signal will be calculated and divided into 14 equal parts. This 3D cubes plot represents the basic 3D cubes plot with regard to all patients. The borders of the boxes will be calculated separately and specifically for each study according to the investigated patients.

Figure 6.20 demonstrates the 3D cubes plot of determined 3D SPPA and represents a healthy subject.

Consideration might also be given to normalizing the resulting 3D cubes plots by rotating the cloud of points in each plane. A first approach is provided by calculating the regression lines in each of the three planes of the 3D cubes plot (see Fig. 6.19). Then a rotation of the cloud of points is performed for both methods, Adapted and

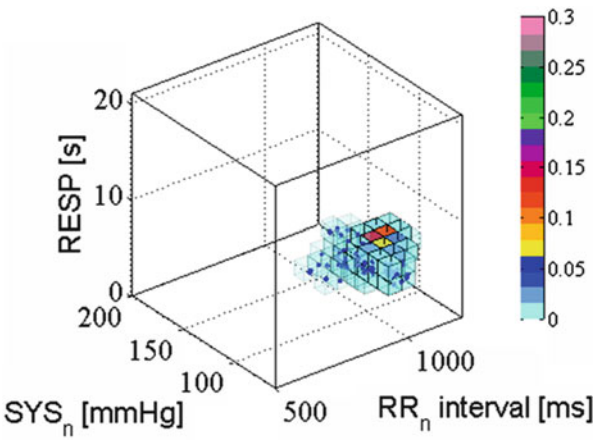

Fig. 6.20 Exemplary coloured 3D cubes plot of the second version of 3D SPPA (determined 3D SPPA)

Determined 3D SPPA. Therefore, regression lines through the centre of the cloud of points will be drawn in each plane of the cubes plot and the angles between the axis and the regression line are calculated. The clouds of points are then rotated by the angles around the main focus of each specific cloud (comparable to the 2D SPPA).

6.6 Conclusions

The methodology of SPPA was introduced and applied to patients suffering from DCM. The results indicated the ability of SPPA to differ between high- and low-risk patients of DCM as well as between DCM patients and healthy subjects. For the first time we could demonstrate that an index from SPPA showing heart rate variability was able to contribute to risk stratification in patients suffering from DCM. Furthermore, SPPA retains nonlinear features of the investigated system, therefore overcoming some limitations of traditional PPA [8].

Finally, we could show that SPPA is rather age-independent in short-time HRV analyses. In future, this study will be examined by comparing the short-term HRV indices between groups of patients and including a healthy control group.

By using a model, Brennan et al. [118] established that the length and width of Poincaré plots are not separately related to LF and HF powers of the HRV signal, respectively, but instead are a weighted combination of LF and HF powers. We could show by applying SPPA that these effects are also superimposed by nonlinear dynamics of HRV.

Additional insights into the underlying physiological mechanisms have been gained by extending the methodology of SPPA. Thus we developed the LSPPA that enhances the PPA method by investigating time correlations of the BBI. LSPPA

provides a prognostic preview for DCM patients regarding several associated symptoms such as endothelial dysfunctions. Therefore, the LSPPA method seems to be a potent risk stratifier in patients with idiopathic DCM.

In our studies we could demonstrate that with specific extension the PPA can lead to much more information about impaired autonomic regulation and has the potential to be applied in much more fields of medical diagnosis and risk stratification.

References

1. O. Rompelman, A.J.R.M. Coenen, R.I. Kitney, Measurement of heart-rate variability: part 1 - comparative study of heart-rate variability analysis methods. Med. Biol. Eng. Comput. **15**(3), 233–239 (1977)
2. J. Jalife, D.C. Michaels, Neural control of sinoatrial pacemaker activity. In *Vagal Control of the Heart: Experimental Basis and Clinical Implications*, ed. by M.N. Levy, P.J. Schwartz (Futura, New York, 1994), pp. 173–205
3. G.F. Chess, R.M.K. Tam, F.R. Calaresu, Influence of cardiac neural inputs on rhythmic variations of heart periods in the cat. Am. J. Physiol. **228**, 775–780 (1975)
4. S. Hales, in *Haemastaticks*, ed. by S. Hales. Statistical Essays, vol. II (Manby & Woodward, London, 1994)
5. E.H. Hon, S.T. Lee, Electronic evaluations of the fetal heart rate patterns preceding fetal death, further observations. Am. J. Obstet. Gynec. **87**, 814–826 (1965)
6. D.J. Ewing, C.N. Martin, R.J. Young, B.F. Clarke, The value of cardiovascular autonomic function tests: 10 years experience in diabetes. Diabetic Care **8**, 491–498 (1985)
7. J. Penaz, J. Roukenz, H.J. Vander Waal, Spectral analysis of some spontaneous rhythms in the circulation. In *Biokybernetik*, ed. by N. Drischel, H. Tiedt (Karl Marx University, Germany, 1968), pp. 233–241
8. B.M. Sayers, Analysis of heart rate variability. Ergonomics **16**(1), 17–32 (1973)
9. H. Luczak, W. Laurig, An analysis of heart rate variability. Ergonomics **16**, 85–97 (1968)
10. J.A. Hirsh, B. Bishop, Respiratory sinus arrhythmia in humans; how breathing pattern modulates heart rate. Am. J. Physiol. Heart Circ. Physiol. **241**, H620–H629 (1981)
11. M.M. Wolf, G.A. Varigos, D. Hunt, J.G. Sloman, Sinus arrhythmia in acute myocardial infarction. Med. J. Australia. **2**, 52–53 (1978)
12. S. Akselrod, D. Gordon, J.B. Madved, N.C. Snidman, D.C. Shannon, R.J. Cohen, Hemodynamic regulation: investigation by spectral analysis. Am. J. Physiol. **249**, H867–H875 (1985)
13. M. Pagani, F. Lombardi, S. Guzzetti, O. Rimoldi, R. Furlan, P. Pizzinelli, G. Sandrone, G. Malfatto, S. Dell'Orto, E. Piccaluga, Power spectral analysis of heart rate and arterial pressure variabilities as a marker of sympatho-vagal interaction in man and conscious dog. Circ. Res. **59**(2), 178–193 (1986)
14. B. Pomeranz, R.J. Macaulay, M.A. Caudill, I. Kutz, D. Adam, D. Gordon, K.M. Kilborn, A.C. Barger, D.C. Shannon, R.J. Cohen, H. Benson, Assessment of autonomic function in humans by heart rate spectral analysis. Am. J. Physiol. **248**(1), H151–H153 (1985)
15. J.L. Bigger, J.T. Fleiss, L.M. Rolnitzky, R.E. Kleiger, J.N. Rottman, Frequency domain measures of heart period variability and mortality after myocardial infarction. Circulation **85**, 164–171 (1992)

DOI 10.1007/978-1-4614-7375-6

16. R.E. Klieger, J.P. Miller, J.T. Bigger, A.J. Moss, the Multicenter Post-Infarction Research Group, Decreased heart rate variability and its association with increased mortality after acute myocardial infarction. Am. J. Cardiol. **59**, 256–262 (1987)
17. M. Malik, T. Farrell, T. Cripps, A.J. Camm, Heart rate variability in relation to prognosis after myocardial infarction: selection of optimal processing techniques. Eur. Heart J. **10**, 1060–1074 (1989)
18. M.G. Signorini, R. Sassi, F. Lombardi, S. Cerutti, Regularity patterns in heart rate variability signal: the approximate entropy approach. In *Proceedings of the 20th Annual International Conference of the IEEE Engineering in Medicine and Biology Society: Biomedical Engineering Towards the Year 2000 and Beyond*, vol. 20, pts 1–6, ed. by H.K. Chang, Y.T. Zhang. *Proceedings of Annual International Conference of the IEEE Engineering in Medicine and Biology Society*, vol. 20, pp. 306–309, 1998
19. M.X. Qin, Y.M. Zang, X.T. Shi, F. Fu, Short-time nonlinear dynamical analysis of heart rate variability in dogs after acute myocardial infarction. In *Proceedings of the 20th Annual International Conference of the IEEE Engineering in Medicine and Biology Society: Biomedical Engineering Towards the Year 2000 and Beyond*, vol. 20, pts 1–6, ed. by H.K. Chang, Y.T. Zhang. *Proceedings of Annual International Conference of the IEEE Engineering in Medicine and Biology Society*, vol. 20, pp. 330–333, 1998
20. M.G. Signorini, S. Guzzetti, R. Parola, S. Cerutti, Complex dynamics assessment in 24-hour heart-rate-variability signals in normal and pathological subjects. In *Proceedings of Computers in Cardiology*, pp. 401–404, 1993, ed. by A. Murray
21. A. Malliani, P.J. Schwartz, A. Zanchetti, A sympathetic reflex elicited by experimental coronary occlusion. Am. J. Physiol. **217**, 703–709 (1969)
22. B. Lown, R. Verrier, Neural activity and ventricular fibrillation. N. Emgl. J. Med. **294**, 1165–1170 (1976)
23. P.J. Schwartz, M.T. La Rovere, E. Vanoli, Autonomic nervous system and sudden cardiac death: experimental basis and clinical observations for post-myocardial infarction risk stratification. Circulation **85**, 177–191 (1992)
24. F. Lombardi, A. Malliani, Power spectral analysis of rr variability. Giornale Italiano di Cardiologia **22**, 501–509 (1992)
25. J. Ip, D. Tepper, J.A. Gomes, S.L. Winters, O. Kjellgren, Identification of patients with high risk of arrhythmic mortality. Role of ambulatory monitoring, signal-averaged ecg, and heart rate variability. Cardiology Clin. **11**, 55–63 (1993)
26. N. Singh, D. Mironov, P.W. Armstrong, A.M. Ross, A. Langer, Heart rate variability assessment early after acute myocardial infarction. Pathophysiological and prognostic correlates. GUSTO ECG substudy investigators. Global utilization of streptokinase and tpa for occluded arteries. Circulation **93**, 1388–1395 (1996)
27. L. Reinhardt, M. Makijarvi, T. Fetsch, G. Schulte, G. Sierra, A. Martinez-Rubio, J. Montonen, T. Katila, M. Borggrefe, G. Breithardt, Noninvasive risk modeling after myocardial infarction. Am. J. Cardiol. **78**, 627–632 (1996)
28. T.R. Rodrigues, R.C. Miranda, A.P. Lichter, N.C. Lobo, C.S. Figueroa, M. da Consolacao Moreira, Heart rate variability in myocardial infarction with and without malignant arrhythmias: comparison with heart transplant recipients and normal subjects. Pacing Clin. Electrophysiol. **19**(11), 1857–1862 (1996)
29. J. Kautzner, J. Camm. Clinical relevance of heart rate variability. Clin. Cardiol. **20**, 162–168 (1997)
30. B. Swynghedauw, S. Jasson, B. Chevalier, J. Clairambault, S. Hardouin, C. Heymes, L. Mangin, P. Mansier, C. Medigue, J.M. Moalic, N. Thibault, F. Carre, Heart rate and heart rate variability, a pharmacological target. Cardiovasc. Drug. Ther. **10**, 677–685 (1997)
31. S.H. Hohnloser, T. Klingenheben, M. Zabel, Y.G. Li, Heart rate variability used as an arrhythmia risk stratifier after myocardial infarction. Pacing Clin. Electrophysiol. **20**, 2594–2601 (1997)
32. F. Naccarella, G. Lepera, A. Rolli, Arrhythmic risk stratification of post-myocardial infarction patients. Curr. Opin. Cardiol. **15**, 1–6 (2000)

33. F. Palacios, R. Ruiz, J. Vila, J.R. Presedo, S. Barro, J. Merino, Applications of heart rate variability analysis in the stratification of arrhythmia risks in acute myocardial infarction. In *Computers in Cardiology* (IEEE Press, 1993), pp. 265–268
34. D.H. Singer, G.J. Martin, N. Magid, J.S. Weiss, J.W. Schaad, R. Kehoe, T. Zheutlin, D.J. Fintel, A.M. Hsieh, M. Lesch, Low heart rate variability and sudden cardiac death. J. Electrocardiol. **21**, S46–S55 (1988)
35. R.E. Bigger, J.T. Kleiger, J.L. Fleiss, L.M. Rolnitzky, J.P. Miller, Components of heart rate variability measured during healing of acute myocardial infarction. Am. J. Cardiol. **61**, 208–215 (1988)
36. F. Lombardi, G. Sandrone, S. Pernpruner, R. Sala, M. Garimoldi, S. Cerutti, G. Baselli, M. Pagani, A. Malliani, Heart rate variability as an index of sympathovagal interaction after acute myocardial infarction. Am. J. Cardiol. **60**, 1239–1245 (1987)
37. A.M. Pellizzer, P.W. Kamen, G. Jackman, D. Brazzale, H. Krum, Non-invasive assessment of baroreflex sensitivity and relation to measures of heart rate variability in man. Clin. Exp. Pharma. Physiol. **23**, 621–624 (1996)
38. G. Mancia, A. Ferrari, L. Gregorini, G. Parati, G. Pomidossi, G. Bertinieri, G. Grassi, A. Zanchetti. Blood pressure variability in man: its relation to high blood pressure, age and baroreflex sensitivity. Clin. Sci. **59**, 401s–404s (1980)
39. J.P. Toyry, J.V. Partanen, L.K. Niskanen, E.A. Lansimies, M.I. Uusitupa, Divergent development of autonomic and peripheral somatic neuropathies in niddm. Diabetologia **40**, 953–958 (1997)
40. H.H. Osterhues, G. Grossmann, M. Kochs, V. Hombach, Heart-rate variability for discrimination of different types of neuropathy in patients with insulin-dependent diabetes mellitus. J. Endocrinol. Invest. **21**, 24–30 (1998)
41. H.L. Kennedy, Beta blockade, ventricular arrhythmias, and sudden cardiac death. Am. J. Cardiol. **80**, 29J–34J (1997)
42. T.G. Farrell, Y. Bashir, T. Cripps, M. Malik, J. Poloniecki, D.E. Bennett, D.E. Ward, A.J. Camm, Risk stratification for arrhythmic events in postinfarction patients based on heart rate variability, ambulatory electrocardiographic variables and the signal-averaged electrocardiogram. J. Am. Coll. Cardiol. **18**(3), 687–697 (1991)
43. M. Kupari, J. Virolainen, P. Koskinen, M.J. Tikkanen, Short-term heart rate variability and factors modifying the risk of coronary artery disease in a population sample. Am. J. Cardiol. **72**(12), 897–903 (1993)
44. M.W. Rich, J.S. Saini, R.E. Kleiger, R.M. Carney, A. teVelde, K.E. Freedland, Correlation of heart rate variability with clinical and angiographic variables and late mortality after coronary angiography. Am. J. Cardiol. **62**(10, Part 1), 714–717, (1988)
45. M.G. Kienzle, D.W. Ferguson, C.L. Birkett, G.A. Myers, W.J. Berg, D.J. Mariano, Clinical, hemodynamic and sympathetic neural correlates of heart rate variability in congestive heart failure. Am. J. Cardiol. **69**(8), 761–767 (1992)
46. J. Nolan, A.D. Flapan, S. Capewell, T.M. MacDonald, J.M. Neilson, D.J. Ewing, Decreased cardiac parasympathetic activity in chronic heart failure and its relation to left ventricular function. Brit. Heart J. **67**(6), 482–485 (1992)
47. D. Gallagher, T. Terenzi, R. de Meersman, Heart rate variability in smokers, sedentary and aerobically fit individuals. Clin. Auton. Res. **2**, 383–387 (1992)
48. P. Koskinen, J. Virolainen, M. Kupari, Acute alcohol intake decreases short-term heart rate variability in healthy subjects. Clin. Sci. **87**(2), 225–230 (1994)
49. S.C. Malpas, E.A. Whiteside, T.J. Maling, Heart rate variability and cardiac autonomic function in men with chronic alcohol dependence. Brit. Heart J. **65**, 84–88 (1991)
50. F.M. Fouad, R.C. Tarazi, C.M. Ferrario, S. Fighaly, C. Alicandri, Assessment of parasympathetic control of heart rate by non-invasive method. Am. J. Phsiol. **246**, H838–H842 (1983)
51. D.L. Eckberg, Human sinus arrhythmia as an index of vagal cardiac outflow. J. Appl. Physiol. **54**, 961–966 (1983)
52. M. Malik, A.J. Camm, Components of heart rate variability – what they really mean and what we really measure. Am. J. Cardiol. **72**, 821–822 (1993)

53. A. Malliani, Cardiovascular sympathetic afferent fibres. Rev. Physiol. Biochem. Pharmacol. **94**, 11–74 (1982)
54. M.V. Kamath, E.L. Fallen, Power spectral analysis of heart rate variability: a noninvasive signature of cardiac autonomic function. Crit. Rev. Biomed. Eng. **21**(3), 245–311 (1993)
55. Task Force of the European Society of Cardiology the North American Society of Pacing Electrophysiology, Heart rate variability: standards of measurement, physiological interpretation, and clinical use. Circulation **93**(5), 1043–1065 (1996)
56. M.N. Levy, H. Zieske, Autonomic control of cardiac pacemaker activity and atriventricular transmission. J. Appl. Physiol. **27**, 465–470 (1969)
57. G. Casolo, E. Bali, T. Taddei, J. Amuhasi, C. Gori, Decreased spontaneous heart rate variability in congestive heart failure. Am. J. Cardiol. **64**(18), 1162–1167 (1989)
58. J.N. Townend, J.N. West, M.K. Davies, W.A. Littler, Effect of quinapril on blood pressure and heart rate in congestive heart failure. Am. J. Cardiol. **69**, 1587–1590 (1992)
59. M.A. Woo, W.G. Stevenson, D.K. Moser, H.R. Middlekauff, Complex heart rate variability and serum norepinephrine levels in patients with advanced heart failure. J. Am. Coll. Cardiol. **23**(3), 565–569 (1994)
60. K.M. Stein, J.S. Borer, C. Hochreiter, P.M. Okin, E.M. Herrold, R.B. Devereux, P. Kligfield, Prognostic value and physiological correlates of heart rate variability in chronic severe mitral regurgitation. Circulation **88**, 127–135 (1993)
61. P.J. Counihan, L. Fei, Y. Bashir, T.G. Farrell, G.A. Haywood, W.J. McKenna, Assessment of heart rate variability in hypertrophic cardiomyopathy. association with clinical and prognostic features. Circulation **88**, 1682–1690 (1993)
62. C.M. Dougherty, R.L. Burr, Comparison of heart rate variability in survivors and nonsurvivors of sudden cardiac arrest. Am. J. Cardiol. **70**, 610–615 (1992)
63. A. Algra, J.G. Tijssen, J.R. Roelandt, J. Pool, J. Lubsen, Heart rate variability from 24-hour electrocardiography and the 2-year risk for sudden death. Circulation **88**, 180–185 (1993)
64. H.V. Huikuri, M.K. Linnaluoto, T. Seppanen, K.E. Airaksinen, K.M. Kessler, J.T. Takkunen, R.J. Myerburg, Circadian rhythm of heart rate variability in survivors of cardiac arrest. Am. J. Cardiol. **70**, 610–615 (1992)
65. G.A. Myers, G.J. Martin, N.M. Magid, P.S. Barnett, J.W. Schaad, J.S. Weiss, M. Lesch, D.H. Singer, Power spectral analysis of heart rate variability in sudden cardiac death: comparison to other methods. IEEE Trans. Biomed. Eng. **33**(12), 1149–1156 (1986)
66. G.J. Martin, N.M. Magid, G. Myers, P.S. Barnett, J.W. Schaad, J.S. Weiss, M. Lesch, D.H. Singer, Heart rate variability and sudden death secondary to coronary artery disease during ambulatory electrocardiographic monitoring. Am. J. Cardiol. **60**, 86–89 (1987)
67. S.H. Hohnloser, T. Klingenheben, Insights into the pathogenesis of sudden cardiac death from analysis of circadian fluctuations of potential triggering factors. Pacing Clin. Electrophysiol. **17**, 428–433 (1994)
68. D.Z. Kocovic, T. Harada, J.B. Shea, D. Soroff, P.L. Friedman, Alterations of heart rate and of heart rate variability after radiofrequency catheter ablation of supraventricular tachycardia. delineation of parasympathetic pathways in the human heart. Circulation **88**, 1671–1681 (1993)
69. A. Lagi, C. Tamburini, M. Cipriani, L. Fattorini, Vagal control of heart rate variability in vasovagal syncope: studies based on 24-h electrocardiogram recordings. Clin. Auton. Res. **7**, 127–130 (1997)
70. C. Lazzeri, G. La Villa, G. Barletta, F. Franchi, 24-hour heart rate variability in patients with vasovagal syncope. Pacing Clin. Electrophysiol. **23**, 463–468 (2000)
71. M. Malik, V. Padmanabhan, W.H. Olson, Automatic measurement of long-term heart rate variability by implanted single-chamber devices. Med. Biol. Eng. Comput. **37**, 585–594 (1999)
72. H.H. Osterhues, S.R. Hanzel, M. Kochs, V. Hombach, Influence of physical activity on 24-hour measurements of heart rate variability in patients with coronary artery disease. Am. J. Cardiol. **80**, 1434–1437 (1997)

73. B. Wennerblom, L. Lurje, H. Tygesen, R. Vahisalo, A. Hjalmarson, Patients with uncomplicated coronary artery disease have reduced heart rate variability mainly affecting vagal tone. Heart **83**, 290–294 (2000)
74. K. Umetani, D.H. Singer, R. McCraty, M. Atkinson, Twenty-four hour time domain heart rate variability and heart rate: relations to age and gender over nine decades. J. Am. Coll. Cardiol. **31**, 593–601 (1998)
75. E. Baykal A. Akinci, A. Celiker T. Tezic, Heart rate variability in diabetic children: sensitivity of the time- and frequency-domain methods. Pediatr. Cardiol. **14**, 140–146 (1993)
76. M.J. Cowan, Measurement of heart rate variability. Western J. Nurs. Res. **17**, 32–48 (1995)
77. C.E. Guzman, G.M. Sanchez, M.F. Marquez, A.G. Hermosillo, M. Cardenas. Differences in heart rate variability between cardioinhibitory and vasodepressor responses to head-up tilt table testing. ARCH MED R, **30**(3), 203–211 (1999)
78. M.J. Hilz, B. Stemper, P. Sauer, U. Haertl, W. Singer, F.B. Axelrod, Cold face test demonstrates parasympathetic cardiac dysfunction in familial dysautonomia. Am. J. Physiol. **276**, R1833–R1839 (1999)
79. A. Uehara, C. Kurata, Sugi, T. Mikami, S. Shouda, Diabetic cardiac autonomic dysfunction: parasympathetic versus sympathetic. Ann. Nucl. Med. **13**, 95–100 (1999)
80. M.P. van den Berg, J. Haaksma, J. Brouwer, R.G. Tieleman, G. Mulder, H.J. Crijns, Heart rate variability in patients with atrial fibrillation is related to vagal tone. Circulation **96**, 1209–1216 (1997)
81. M.M. Massin, K. Maeyns, N. Withofs, F. Ravet, P. Gerard, Circadian rhythm of heart rate and heart rate variability. Arch. Dis. Child. **83**, 179–182 (2000)
82. A. Lagi, C. Tamburini, L. Fattorini, S. Cencetti, Autonomic control of heart rate variability in vasovagal syncope: a study of the nighttime period in 24-hour recording. Clin. Auton. Res. **9**, 179–183 (1999)
83. L.A. Fleisher, J.F. Fleckenstein, S.M. Frank, P.J. Thuluvath, Heart rate variability as a predictor of autonomic dysfunction in patients awaiting liver transplantation. Digest. Dis. Sci. **45**, 340–344 (2000)
84. D. Ramaekers, H. Ector, A.E. Aubert, A. Rubens, F. Van de Werf, Heart rate variability and heart rate in healthy volunteers: is the female autonomic nervous system cardioprotective? Euro. Heart J. **19**, 1334–1341 (1998)
85. M.A. Woo, D.K. Moser, L.W. Stevenson, W.G. Stevenson, Six-minute walk test and heart rate variability: lack of association in advanced stages of heart failure. Am. J. Crit. Care **6**(1), 348–354 (1997)
86. M.A. Woo, W.G. Stevenson, D.K. Moser, Comparison of four methods of assessing heart rate variability in patients with heart failure. Am. J. Crit. Care **5**(1), 34–41 (1996)
87. P.W. Kamen, Heart rate variability. Aust. Fam. Physician **25**, 1087–1094 (1996)
88. P.W. Kamen, H. Krum, A.M. Tonkin, Low-dose but not high-dose captopril increases parasympathetic activity in patients with heart failure. J. Cardiovasc. Pharmacol. **30**, 7–11 (1997)
89. P.W. Kamen, A.M. Tonkin, Application of the poincar plot to heart rate variability: a new measure of functional status in heart failure. Aust. NZ. J. Med. **25**, 18–26 (1995)
90. M.A. Woo, W.G. Stevenson, D.K. Moser, Effects of ventricular ectopy on sinus r-r intervals in patients with advanced heart failure. Heart Lung **21**, 515–522 (1992)
91. M.A. Woo, W.G. Stevenson, D.K. Moser, R.B. Trelease, R.M. Harper, Patterns of beat-to-beat heart rate variability in advanced heart failure. Am. Heart J. **123**(3), 704–710 (1992)
92. M. Brennan, P. Kamen, M. Palaniswami, A neural system for heart rate variability analysis. In *IEEE Proceedings of the 2nd IEEE International Conference on Intelligent Processing Systems*, IEEE Press, 1998
93. M. Brennan, P. Kamen, M. Palaniswami, A new cardiac nervous system model for heart rate variability analysis. In *Proceedings of the 20th Annual International Conference of the IEEE Engineering in Medicine and Biology Society*, pp. 349–352, IEEE Press, 2000
94. P.W. Kamen, H. Krum, A.M. Tonkin. Poincaré plot of heart rate variability allows quantitative display of parasympathetic nervous activity in humans. Clin. Sci. **91**, 201–208 (1996)

95. M. Nakao, M. Norimatsu, Y. Mizutani, M. Yamamoto, Spectral distortion properties of the integral pulse frequency modulation model. IEEE Trans. Biomed. Eng. **44**(5), 419–426 (1997)
96. R.K. Mohn, Suggestions for the harmonic analysis of point process data. Comput. Biomed. Res. **9**, 521–530 (1976)
97. R.D. Hyndman, R.K. Mohn, A model of the cardiac pacemaker and its use in decoding the information content of cardiac intervals. Automedica **1**, 239–252 (1975)
98. R.W. De Boer, J.M. Karemaker, J. Strackee, Description of heart-rate variability data in accordance with a physiological model for the genesis of heartbeats. Psychophysiology **22**(2), 147–154 (1985)
99. R.W. De Boer, J.M. Karemaker, Spectrum of a series of point events generated by the integral pulse frequency modulation model. Med. Biol. Eng. Comput. **23**, 138–142 (1985)
100. R.W. De Boer, J.M. Karemaker, J. Strackee, Comparing spectra of a series of point events particularly for heart rate variability. IEEE Trans. Biomed. Eng. **31**(4), 384–387 (1984)
101. R.D. Berger, J.P. Saul, R.J. Cohen, Transfer function analysis of autonomic regulation. I. Canine atrial rate response. Am. J. Physiol. Heart Circ. Physiol. **256**(1), H142–H152 (1989)
102. R.D. Berger, S. Askelrod, D. Gordon, R.J. Cohen, An efficient algorithm for spectral analysis of heart rate variability. IEEE Trans. Biomed. Eng. **33**, 900–904 (1986)
103. S. Akselrod, D. Gordon, F.A. Ubel, D.C. Shannon, A.C. Berger, R.J. Cohen, Power spectrum analysis of heart rate fluctuation: a quantitative probe of beat-to-beat cardiovascular control. Science **213**(4504), 220–222 (1981)
104. N. Montano, T.G. Ruscone, A. Porta, F. Lombardi, M. Pagani, A. Malliani, Power spectrum analysis of heart rate variability to assess the changes in sympathovagal balance during graded orthostatic tilt. Circulation **90**(4), 1826–1831 (1994)
105. K.E. Sands, M.L. Appel, L.S. Lilly, F.J. Schoen, G.H. Mudge, R.J. Cohen, Power spectrum analysis of heart rate variability in human cardiac transplant recipients. Circulation **79**, 76–82 (1989)
106. A. Voss, S. Schulz, R. Schroeder, M. Baumert, P. Caminal, Methods derived from nonlinear dynamics for analysing heart rate variability. Philos. Trans. Roy. Soc. A **367**(1887), 277–296 (2009)
107. J.J. Goldberger, M.W. Ahmed, M.A. Parker, A.H. Kadish, Dissociation of heart rate variability from parasympathetic tone. Am. J. Physiol. **266**, H2152–H2157 (1994)
108. J.J. Goldberger, Y.H. Kim, M.W. Ahmed, M.A. Parker, A.H. Kadish, Effect of graded increases in parasympathetic tone on heart rate variability. J. Cardiovasc. Electrophysiol. **7**, 594–602 (1996)
109. A.L. Goldberger, J.E. Mietus, D.R. Rigney, M.L. Wood, S.M. Fortney, Effects of head-down bed rest on complex heart rate variability: response to lbnp testing. J. Appl. Physiol. **77**, 2863–2869 (1994)
110. L. Glass, Chaos and heart rate variability. J. Cardiovasc. Electrophysiol. **10**, 1358–1360 (1999)
111. M.P. Tulppo, T.H. Makikallio, T.E.S. Takala, T. Seppanen, H.V. Huikuri, Quantitative beat-to-beat analysis of heart rate dynamics during exercise. Am. J. Physiol. **271**, H244–H252 (1996)
112. M. Brennan, M. Palaniswami, P. Kamen, Do existing measures of poincare plot geometry reflect nonlinear features of heart rate variability. IEEE Trans. Biomed. Eng. **48**, 1342–1347 (2001)
113. L.S. Liebovitch, D. Scheurle, Two lessons from fractals and chaos. Complexity **5**, 34–43 (2000)
114. U.R. Acharya, K.P. Joseph, N. Kannathal, C.M. Lim, J.S. Suri, Heart rate variability: a review. Med. Biol. Eng. Comput. **44**(12), 1031–1051 (2006)
115. M.P. Tulppo, T.H. Makikallio, T. Seppanen, J.K.E. Airaksinen, H.V. Huikuri, Heart rate dynamics during accentuated sympathovagal interaction. Am. J. Physiol. **247**, H810–H816 (1998)
116. M. Toichi, T. Sugiura, T. Murai, A. Sengoku, A new method of assessing cardiac autonomic function and its comparison with spectral analysis and coefficient of variation of r-r interval. J. Auton. Nerv. Syst. **62**, 79–84 (1997)

117. J. Hayano, H. Takahashi, T. Toriyama, S. Mukai, A. Okada, S. Sakata, A. Yamada, N. Ohte, H. Kawahara, Prognostic value of heart rate variability during long-term follow-up in chronic haemodialysis patients with end-stage renal disease. Nephrol. Dial. Transplant. **14**, 1480–1488 (1999)
118. M. Brennan, M. Palaniswami, P. Kamen, Poincare plot interpretation using a physiological model of hrv based on a network of oscillators. Am. J. Physiol. Heart Circ. Physiol. **283**, 1873–1886 (2002)
119. R.E. De Meersman, S.S. Reisman, M. Daum, R. Zorowitz, M. Leifer, T. Findley, Influence of respiration on metabolic, hemodynamic, psychometric, and r-r interval power spectral parameters. Am. J. Physiol. Heart Circ. Physiol. **269**(4), H1437–H1440 (1995)
120. M.V. Hjgaard, N.-H. Holstein-Rathlou, E. Agner, J.K. Kanters, Dynamics of spectral components of heart rate variability during changes in autonomic balance. Am. J. Physiol. Heart Circ. Physiol. **275**(1), H213–H219 (1998)
121. J.H. Warren, R.S. Jaffe, C.E. Wraa, C.L. Stebbins, Effect of autonomic blockade on power spectrum of heart rate variability during exercise. Am. J. Physiol. Regul. Integr. Comp. Physiol. **273**(2), R495–R502 (1997)
122. P. Sleight, M.T. La Rovere, A. Mortara, G. Pinna, R. Maestri, S. Leuzzi, B. Bianchini, L. Tavazzi, L. Bernardi, Physiology and pathophysiology of heart rate and blood pressure variability in humans: is power spectral analysis largely an index of baroreflex gain? Clin. Sci. **88**(1), 103–109 (1995)
123. L.T. Mainardi, A.M. Bianchi, G. Baselli, S. Cerutti, Pole-tracking algorithms for the extraction of time-variant heart rate variability spectral parameters. IEEE Trans. Biomed. Eng. **42**(3), 250–259 (1995)
124. A. Rosenblueth, F.A. Simeone, The interrelations of vagal and accelerator effects on the cardiac rate. Am. J. Physiol. **110**, 42–55 (1934)
125. J.J. Goldberger, Sympathovagal balance: how should we measure it? Am. J. Physiol. Heart Circ. Physiol. **276**(4), H1273–H1280 (1999)
126. P.G. Katona, M. McLean, D.H. Dighton, A. Guz, Sympathetic and parasympathetic cardiac control in athletes and nonathletes at rest. J. Appl. Physiol. **52**(6), 1652–1657 (1982)
127. H. Otzenberger, C. Gronfier, C. Simon, A. Charloux, J. Ehrhart, F. Piquard, G. Brandenberger, Dynamic heart rate variability: a tool for exploring sympathovagal balance continuously during sleep in men. Am. J. Physiol. Heart Circ. Physiol. **275**(3), H946–H950 (1998)
128. C.A. Del Negro, C.G. Wilson, R.J. Butera, H. Rigatto, J.C. Smith, Periodicity, mixed-mode oscillations, and quasiperiodicity in a rhythm-generating neural network. Biophys. J. **82**, 206–214 (2002)
129. V.L. Schechtman, M.Y. Lee, A.J. Wilson, R.M. Harper, Dynamics of respiratory patterning in normal infants and infants who subsequently died of the sudden infant death syndrome. Pediatr. Res. **40**, 571–577 (1996)
130. R.A. Thuraisingham, Enhancing poincare plot information via sampling rates. Appl. Math. Comput. **186**, 1374–1378 (2007)
131. C. Lerma, O. Infante, H. Perez-Grovas, M.V. Jose, Poincaré plot indexes of heart rate variability capture dynamic adaptations after haemodialysis in chronic renal failure patients. Clin. Physiol. Funct. Imaging **23**(2), 72–80 (2003)
132. T.P. Thakre, M.L. Smith, Loss of lag-response curvilinearity of indices of heart rate variability in congestive heart failure. BMC Cardiovasc. Disorders **6**, 27 (2006)
133. A. Goshvarpour, A. Goshvarpour, S. Rahati, Analysis of lagged poincar plots in heart rate signals during meditation. Digit. Signal Process. **21**(2), 208–214 (2011)
134. The Physionet Website, Computers in cardiology challenge 2002 (cinc 2002): Rr interval time series modelling (2002). http://www.physionet.org/challenge/2002/
135. C. Karmakar, A. Khandoker, J. Gubbi, M. Palaniswami, Complex correlation measure: a novel descriptor for poincaré plot. Biomed. Eng. OnLine **8**(1), 17 (2009)
136. P. Contreras, R. Canetti, E. Migliaro, Correlations between frequency-domain hrv indices and lagged poincaré plot width in healthy and diabetic subjects. Physiol. Meas. **28**, 85–94 (2007)

137. T. Vybrial, R.J. Byrg, M.E. Maddens, W.E. Boden, Effect of passive tilt on sympathetic and parasympathetic components of heart rate variability in normal subjects. Am. J. Cariol. **63**, 1117–1120 (1989)
138. J. Hayano, Y. Sakakibara, A. Yamada, Accuracy of assessment of cardiac vagal tone by heart rate variability in normal subjects. Am. J. Cardiol. **67**, 199–204 (1991)
139. M.. La Rovere, A. Mortara, P. Pantaleo, R. Maestri, F. Cobelli, L. Tavazzi, Scopolamine improves autonomic balance in advanced congestive heart failure. Circulation **90**(2), 838–843 (1994)
140. R.S. Jaffe, D.L. Fung, K.H. Behrman, Optimal frequency ranges for extracting information on autonomic activity from the heart rate spectrogram. J. Auton. Nerv. Syst. **46**(1–2), 37–46 (1994)
141. Y. Nakamura, Y. Yamamoto, I. Muraoka, Autonomic control of heart rate during physical exercise and fractal dimension of heart rate variability. J. Appl. Physiol. **74**(2), 875–881 (1993)
142. Y. Yamamoto, R.L. Hughson, Coarse-graining spectral analysis: new method for studying heart rate variability. J. Appl. Physiol. **71**(3), 1143–1150 (1991)
143. M.E. Dibner-Dunlap, D.L. Eckberg, N.M. Magid, N.M. Cintron-Trevino, The long-term increase of baseline and reflexly augmented levels of human vagal-cardiac nervous activity induced by scopolamine. Circulation **71**(4), 797–804 (1985)
144. T. Vybrial, R.J. Byrg, M.E. Maddens, S.S. Bhasin, W.E Chronin, W.E. Boden, M.H. Lehmann, Effects of transdermal scopolamine on heart rate variability in normal subjects. Am. J. Cariol. **65**, 604–608 (1990)
145. A.L. Goldberger, L.A.N. Amaral, L. Glass, J.M. Hausdorff, P.C. Ivanov, R.G. Mark, J.E. Mietus, G.B. Moody, C.-K. Peng, H.E. Stanley, PhysioBank, PhysioToolkit, and PhysioNet: components of a new research resource for complex physiologic signals. Circulation **101**(23), e215–e220 (2000). Circulation Electronic Pages: http://circ.ahajournals.org/cgi/content/full/101/23/e215
146. M.J. Eisenberg, Risk stratification for arrhythmic events: are the bangs worth the bucks? J. Am. Coll. Cardiol. **38**(7), 1912–1915 (2001)
147. J.E. Hartikainen, M. Malik, A. Staunton, J. Poloniecki, A.J. Camm, Distinction between arrhythmic and nonarrhythmic death after acute myocardial infarction based on hear rate variability, signal-averaged electrocardiogram, ventricular arrhythmias and left ventricular ejection fraction. J. Am. Coll. Cariol. **28**(2), 296–304 (1996)
148. A. Rydberg, M. Karlsson, R. Hornsten, U. Wiklund, Can analysis of heart rate variability predict arrhythmia in children with fontan circulation? Pediatr. Cardiol. **29**, 50–55 (2008)
149. M. Costa, A.L. Goldberger, C.K. Peng, Broken asymmetry of the human heartbeat: loss of time irreversibility in aging and disease. Phys. Rev. Lett. **95**(198102), 1–4 (2005)
150. D.R. Chialvo, M.M. Millonas, Asymmetric unbiased fluctuations are sufficient for the operation of a correlation ratchet. Phys. Lett. A **209**(1–2), 26–30 (1995)
151. I. Prigogine, I. Antoniou, Laws of nature and time symmetry breaking. Ann. N. U. Acad. Sci. **879**, 8–28 (2007)
152. M. Costa, A.L. Goldberger, C.K. Peng, Multiscale entropy analysis of physiological time series. Phys. Rev. Lett. **89**, 062102 (2002)
153. J. Piskorski, P. Guzik, Geometry of the poincaré plot of rr intervals and its asymmetry in healthy hearts. Physiol. Meas. **28**, 287–300 (2007)
154. A. Porta, K.R. Casali, A.G. Casali, T. Gnecchi-Ruscone, E. Tovaldini, N. Montano, S. Lange, D. Geue, D. Cysarz, P. Van Leeuwen, Temporal asymmetries of short-term heart period variability are linked to autonomic regulation. Am. J. Physiol. Regul. Integr. Comp. Physiol. **295**, R550–R557 (2008)
155. A. Porta, S. Guzzetti, N. Montano, T. Gnecchi-Ruscone, A. Malliani, Time reversibility in short-term heart period variability. Comp. Cardiol. **33**, 77–80 (2006)
156. P. Guzik, J. Piskorski, T. Krauze, A. Wykretowicz, H. Wysocki, Heart rate asymmetry by poincaré plots of rr intervals. Biomed. Tech. **51**, 530–537 (2006)

157. C.L. Ehlers, J. Havstad, D. Prichard, J. Theiler, Low doses of ethanol reduce evidence for nonlinear structure in brain activity. J. Neurosci. **18**, 7474–7486 (1998)
158. J.T. Bigger Jr., J.L. Fleiss, R.C. Steinman, L.M. Rolnitzky, W.J. Schneider, P.K. Stein, Rr variability in healthy, middle-aged persons compared with patients with chronic coronary heart disease or recent acute myocardial infarction. Circulation **91**(7), 1936–1943 (1995)
159. D.L. Eckberg, Nonlinearities of the human carotid baroreceptor-cardiac reflex. Circ. Res. **47**, 208–216 (1980)
160. J. Theiler, S. Eubank, A. Longtin, B. Galdrikian, J.D. Farmer, Testing for nonlinearity in time series: the method of surrogate data. Physica **58**, 77–94 (1992)
161. T. Nkamura,M Small, Applying the method of small-shuffle surrogate data: testing for dynamics in fluctuating data with trends. Int. J. Bifurcat. Chaos **16**(12), 3581–3603 (2006)
162. M. Nurujjaman, R. Narayanan, A.N. Sekar Iyengar, Comparative study of nonlinear properties of eeg signals of normal persons and epileptic patients. Nonlinear Biomed. Phys. **3**, 6 (2009). doi: 10.1186/1753–4631–3–6
163. P.D. Welch, The use of fast fourier transform for the estimation of power spectra: A method based on time averaging over short, modified periodograms. IEEE Trans. Audio Electroacous. **15**(2), 70–73 (1967)
164. C. Spearman, The proof and measurement of association between two things. Am. J. Psychol. **15**, 72–101 (1904)
165. C.K. Karmakar, A.H. Khandoker, J. Gubbi, M. Palaniswami, Defining asymmetry in heart rate variability signals using a poincaré plot. Physiol. Meas. **30**(11), 1227 (2009)
166. A. Porta, S. Guzzetti, M. Pagani, A. Malliani, S. Cerutti, Prediction of short cardiovascular variability signals based on conditional distribution. IEEE Trans. Biomed. Eng. **47**, 1555–1564 (2000)
167. A. Porta, S. Guzzetti, R. Furlan, T. Gnecchi-Ruscone, N. Montano, Complexity and nonlinearity in short-term heart period variability: comparison of methods based on local nonlinear prediction. IEEE Trans. Biomed. Eng. **54**, 94–106 (2007)
168. S. Carrasco, M.J. Gaitan, R. Gonzalez, O. Yanez, Correlation among poincaré plot indexes and time and frequency domain measures of heart rate variability. J. Med. Eng. Technol. **25**, 240–248 (2001)
169. D.L. Eckberg, Sympathovagal balance: a critical appraisal. Circulation **96**, 3224–3232 (1997)
170. A. Babloyantz, A. Destexhe, Is the normal heart a periodic oscillator? Biol. Cybern. **58**(3), 203–211 (1988)
171. W. Grimm, P. Alter, B. Maisch, Arrhythmia risk stratification with regard to prophylactic implantable defibrillator therapy in patients with dilated cardiomyopathy. results of macas, definite, and scd-heft. Herz **29**(3), 348–352 (2004)
172. A. Voss, R. Schroeder, S. Truebner, M. Goernig, H.R. Figulla, A. Schirdewan, Comparison of nonlinear methods symbolic dynamics, detrended fluctuation, and poincare plot analysis in risk stratification in patients with dilated cardiomyopathy. Chaos **17**(1), 0151201 (2007)
173. A. Voss, C. Fischer, R. Schroeder, H.R. Figulla, M. Goernig, Segmented poincaré plot analysis for risk stratification in patients with dilated cardiomyopathy. Methods Inf. Med. **49**(5), 511–515 (2010)
174. A. Voss, C. Fischer, R. Schroeder, H.R. Figulla, M. Goernig, Lagged segmented poincaré plot analysis for risk stratification in patients with dilated cardiomyopathy. Med. Biol. Eng. Comput. **50**, 727–736 (2012)
175. W. Grimm, M. Christ, J. Bach, H.H. Muller, B. Maisch, Noninvasive arrhythmia risk stratification in idiopathic dilated cardiomyopathy: results of the marburg cardiomyopathy study. Circulation **108**(23), 2883–2891 (2003)
176. J. Piskorski, P. Guzik, Filtering poincaré plots. Comput. Method. Sci. Technol. **11**(1), 39–48 (2005)
177. R. Moe-Nilssen, J.L. Helbostad, Estimation of gait cycle characteristics by trunk accelerometry. J. Biomech. **37**(1), 121–126 (2004)

178. D. Hoyer, B. Pompe, K.H. Chon, H. Hardraht, C. Wicher, U. Zwiener, Mutual information function assesses autonomic information flow of heart rate dynamics at different time scales. IEEE Trans. Biomed. Eng. **52**(4), 584–592 (2005)
179. D. Hoyer, U. Leder, H. Hoyer, B. Pompe, M. Sommer, U. Zwiener, Mutual information and phase dependencies: measures of reduced nonlinear cardiorespiratory interactions after myocardial infarction. Med. Eng. Phys. **24**(1), 33–43 (2002)
180. S.G. Priori, E. Aliot, C. Blomstrom-Lundqvist, L. Bossaert, G. Breithardt, P. Brugada, A.J. Camm, R. Cappato, S.M. Cobbe, C. Di Mario, B.J. Maron, W.J. McKenna, A.K. Pedersen, U. Ravens, P.J. Schwartz, M. Trusz-Gluza, P. Vardas, H.J. Wellens, D.P. Zipes, Task force on sudden cardiac death of the european society of cardiology. Eur. Heart J. **22**(16), 1374–1450 (2001)
181. P. Schirdewahn, A. Dorszewski, G. Hindricks, R. Kobza, H. Kottkamp, H. Tanner, Plötzlicher herztod und icd-therapie. J. Kardiol. **11**, 3–10 (2004)
182. S.B. Mohan, M. Parker, M. Wehbi, P. Douglass, Idiopathic dilated cardiomyopathy: a common but mystifying cause of heart failure. Cleve. Clin. J. Med. **69**(6), 481–487 (2002)
183. N. Wessel, A. Voss, H. Malberg, C. Ziehmann, H.U. Voss, A. Schirdewan, U. Meyerfeldt, J. Kurths, Nonlinear analysis of complex phenomena in cardiological data. Herzschr. Elektrophys. **11**, 159–173 (2000)
184. O. Przibille, A. Liebrich, B. Nowak, S. Rosocha, C.H. Zellerhoff, S. Geil, E. Himmrich, N. Treese, J. Meyer, Prognostic significance of analysis of heart rate variability in patients with dilated cardiomyopathy. Z Kardiol. **87**(6), 453–458 (1998)
185. F. Lombardi, Chaos theory, heart rate variability, and arrhythmic mortality. Circulation **101**(1), 8–10 (2000)
186. R.E. Klieger, P.K. Stein, J.T. Bigger Jr., Heart rate variability: measurement and clinical utility. Ann. Noninvasive Electrocardiol. **10**(1), 88–101 (2005)
187. H.V. Huikuri, J.S. Perkiomaki, R. Maestri, G.D. Pinna, Clinical impact of evaluation of cardiovascular control by novel methods of heart rate dynamics. Philos. Trans. A Math. Phys. Eng. Sci. **367**(1892), 1223–1238 (2009)
188. A.E. Aubert, B. Seps, F. Beckers, Heart rate variability in athletes. Sports Med. **33**(12), 889–919 (2003)
189. R.P. Nolan, M.V. Kamath, J.S. Floras, J. Stanley, C. Pang, P. Picton, Q.R. Young, Heart rate variability biofeedback as a behavioral neurocardiac intervention to enhance vagal heart rate control. Am. Heart J. **149**(6), 1137 (2005)
190. M. Risk, V. Bril, C. Broadbridge, A. Cohen, Heart rate variability measurement in diabetic neuropathy: review of methods. Diabetes Technol. Ther. **3**(1), 63–76 (2001)
191. M. Javorka, J. Javorkova, I. Tonhajzerova, A. Calkovska, K. Javorka, Heart rate variability in young patients with diabetes mellitus and healthy subjects explored by poincare and sequence plots. Clin. Physiol. Funct. Imaging **25**(2), 119–127 (2005)
192. P.K. Stein, P.P. Domitrovich, H.V. Huikuri, R.E. (Cast Investigators) Kleiger, Traditional and nonlinear heart rate variability are each independently associated with mortality after myocardial infarction. J. Cardiovasc. Electrophysiol. **16**, 13–20 (2005)
193. A.H. Glassman, J.T. Bigger, M. Gaffney, L.T. Van Zyl, Heart rate variability in acute coronary syndrome patients with major depression: influence of sertraline and mood improvement. Arch. Gen. Psychiatry **64**(9), 1025–1031 (2007)
194. H. Malberg, R. Bauernschmitt, A. Voss, T. Walther, R. Faber, H. Stepan, N. Wessel, Analysis of cardiovascular oscillations: a new approach to the early prediction of pre-eclampsia. Chaos **17**(1), 015113 (2007)
195. K.M. Stein, Noninvasive risk stratification for sudden death: signal-averaged electrocardiography, nonsustained ventricular tachycardia, heart rate variability, baroreflex sensitivity, and qrs duration. Prog. Cardiovasc. Dis. **51**(2), 106–117 (2008)
196. J.E. Skinner, J.M. Anchin, D.N. Weiss, Nonlinear analysis of the heartbeats in public patient ecgs using an automated pd2i algorithm for risk stratification of arrhythmic death. Ther. Clin. Risk Manag. **4**(2), 549–557 (2008)

197. V.A. Cornelissen, B. Verheyden, A.E. Aubert, R.H. Fagard, Effects of aerobic training intensity on resting, exercise and post-exercise blood pressure, heart rate and heart-rate variability. J. Hum. Hypertens **24**(3), 175–182 (2010)
198. A. Voss, A. Heitmann, R. Schroeder, A. Peters, S. Perz, Short-term heart rate variability-age dependence in healthy subjects. Physiol. Meas. **33**(8), 1289–1311 (2012)
199. R. Holle, M. Happich, H. Lowel, H.E. Wichmann, Monica Kora Study Group. Kora—a research platform for population based health research. Gesundheitswesen **67**(1), S19–S25 (2005)
200. Report of the national high blood pressure education program working group on high blood pressure in pregnancy. Am. J. Obstet. Gynecol. **183**(1), S1–S22 (2000)
201. R. Faber, M. Baumert, H. Stepan, N. Wessel, A. Voss, T. Walther, Baroreflex sensitivity, heart rate, and blood pressure variability in hypertensive pregnancy disorders. J. Hum. Hypertens **18**(10), 707–712 (2004)
202. A. Voss, H. Malberg, A. Schumann, N. Wessel, T. Walther, H. Stepan, R. Faber, Baroreflex sensitivity, heart rate, and blood pressure variability in normal pregnancy. Am. J. Hypertens **13**(11), 1218–1225 (2000)
203. J.P. Greenwood, J.B. Stoker, J.J. Walker, D.A. Mary, Sympathetic nerve discharge in normal pregnancy and pregnancy-induced hypertension. J. Hypertens **16**(5), 617–624 (1998)
204. H.P. Schobel, T. Fischer, K. Heuszer, H. Geiger, R.E. Schmieder, Preeclampsia – a state of sympathetic overactivity. N. Engl. J. Med. **335**(20), 1480–1485 (1996)
205. A. Seeck, M. Baumert, C. Fischer, A. Khandoker, R. Faber, A. Voss, Advanced poincare plot analysis differentiates between hypertensive pregnancy disorders. Physiol. Meas. **32**(10), 1611–1622 (2011)
206. A. Bernjak, P.B. Clarkson, P.V. McClintock, A. Stefanovska, Low-frequency blood flow oscillations in congestive heart failure and after beta1-blockade treatment. Microvasc. Res. **76**, 224–232 (2008)
207. M. Rossi, A. Carpi, C. Di Maria, F. Franzoni, F. Galetta, G. Santoro, Post-ischaemic peak flow and myogenic flowmotion component are independent variables for skin post-ischaemic reactive hyperaemia in healthy subjects. Microvasc. Res. **74**, 9–14 (2007)
208. I.V. Tikhonova, A.V. Tankanag, N.K. Chemeris, Time-amplitude analysis of skin blood flow oscillations during the post-occlusive reactive hyperemia in human. Microvasc. Res. **80**, 58–64 (2010)
209. T.A. Kuusela, T.J. Kaila, M. Kahonen, Fine structure of the low-frequency spectra of heart rate and blood pressure. BMC Physiol. **3**, 11 (2003)
210. C.B. Treasure, J.A. Vita, D.A. Cox, R.D. Fish, J.B. Gordon, G.H. Mudge, W.S. Colucci, M.G. Sutton, A.P. Selwyn, R.W. Alexander et al., Endothelium-dependent dilation of the coronary microvasculature is impaired in dilated cardiomyopathy. Circulation **81**(3), 772–779 (1990)
211. L. Kaiser, R.C. Spickard, N.B. Olivier, Heart failure depresses endothelium-dependent responses in canine femoral artery. Am. J. Physiol. **256**(4 Pt 2), H962–H967 (1989)
212. F.J. Harris, On the use of windows for harmonic analysis with the discrete fourier transform. Proc. IEEE **66**(1), 172–204 (1978)
213. Y. Zhang, Z. Guo, W. Wang, S. He, T. Lee, M. Loew, A comparison of the wavelet and short-time fourier transforms for doppler spectral analysis. Med. Eng. Phys. **25**(7), 547–557 (2003)
214. C. Ludwig, Beiträge zur kenntniss des einflusses der respirationsbewegung auf den blutlauf im aortensystem. Arch. Anat. Physiol. **13**, 242–302 (1847)
215. Lt. Col. KK. Tripathi, Respiration and heart rate variability: a review with special reference to its application in aerospace medicine. Indian J. Aero. Med. **48**(1), 64–75 (2004)
216. A. Seeck, W. Rademacher, C. Fischer, J. Haueisen, R. Surber, A. Voss, Prediction of atrial fibrillation recurrence after cardioversion – interaction analysis of cardiac autonomic regulation. Med. Eng. Phys. **35**(4), 471–479 (2012)
217. P.A. Gould, M.D. Esler, D.M. Kaye, Atrial fibrillation is associated with decreased cardiac sympathetic response to isometric exercise in chf in comparison to sinus rhythm. Pacing Clin. Electrophysiol. **31**(9), 1125–1129 (2008)

Index

A.H. Khandoker et al., *Poincaré Plot Methods for Heart Rate Variability Analysis*,
DOI 10.1007/978-1-4614-7375-6, © Springer Science+Business Media New York 2013